Design and test of beamforming networks for a Galileo antenna array

Master thesis

by

Arturo Arango Selga

Supervisor:

Eduardo Schittler-Neves, German Aerospace Center

Examiner:

Per-Simon Kildal, Chalmers University of Technology

Chalmers University of Technology, June 2006

This work is dedicated to my parents,

Diana Selga Austrums

and

Arturo Armando Arango Herrera

Acknowledgments

To my colleagues in the antenna group of the Communications and Navigation Institute of DLR, Eduardo Schittler-Neves, Marcos Heckler, Lukasz Greda, and Wahid Elmarissi not only for their advice and help during this stage but also for their friendship.

To my parents, Diana Selga Austrums and Arturo Armando Arango Herrera, to my sister and my brother, Valerie Diana Arango Selga and Guillermo Pérez-Nájera Selga, that even from the distance have always supported me and been there when I needed them.

To Anna Kalinowska, for being there during this time and for all her support and love.

To my professors in Chalmers, Piotr Starski, Lennart Lundgren, Harald Merkel and Per-Simon Kildal; very special thanks to Joakim Johansson whose lectures, advice, and humor were always an inspiration.

To the STINT Foundation whose financial support allowed me to pursue my education in Sweden.

To my friends and family in Mexico and around the world.

Abstract

The beamforming analysis and the design of a series of microstrip power dividers to passively test beamforming on a broadband planar array thought for the European navigation system Galileo are presented. Analyses in terms of mutual coupling and beamsteering limits show that it is possible to steer the main beam 360° in azimuth and in elevations larger than 45° while keeping the maximum directivity in the desired direction for all the operational frequencies of the antenna array, in the range from 1.19 GHz to 1.57 GHz. Based on these analyses, power dividers providing the amplitudes and phases required for a series of beamforming scenarios were designed to passively test the performance of the antenna array. The design and optimization were done using planar electromagnetic simulation tools such as Ansoft Designer® and HFSS®. Simulation results for the different beamforming power dividers show that is possible to achieve a good precision in terms of output phases and amplitudes which in turn results in radiation patterns with precise beam pointing and good side lobe level suppression when fed into the antenna array.

Index Terms—Active antennas, Antenna array feeds, Array signal processing, Microstrip antennas

Preface

This thesis project is presented in June 2006 in the context of the international master program ‘Hardware for Wireless Communications’ of the Chalmers University of Technology. The project was developed from October 2005 to May 2006 at the antenna group of the Institute of Communications and Navigation of the German Aerospace Center – Deutsches Zentrum für Luft und Raumfahrt (DLR) as part of a long-term collaboration between the German Aerospace Center and the Chalmers University of Technology

The supervisor of this project at the DLR was Eduardo Schittler-Neves and the examiner at the Chalmers University of Technology was Professor Per-Simon Kildal.

Table of contents

Chapter 1 – Introduction

High accuracy levels for future combined Galileo/GPS applications pushes for the development of improvements in the domain of signal processing as well as of modern antenna technologies. The employment of smart antenna arrays with digital beamforming (DBF) can improve the navigation accuracy by tracking the visible satellites with multiple beams including multipath and jammer reduction. In modern beamforming antenna systems this is achieved by implementing complex beamforming algorithms such as MUSIC, ESPIRIT or Least Mean Squares on a Digital Signal Processor (DSP) controlling the amplitudes and phases that are fed into each of the elements.

One of the objectives of the GALANT (Galileo Antenna) project under development at the Deutsches Zentrum für Luft und Raumfahrt (DLR) is the analysis of antenna array performance for beamforming. Its performance can be tested when precise excitation in amplitude and phase is provided to each antenna input terminal by means of passive beamforming feed networks. Such excitations can be computed by means of beamforming algorithms together with knowledge of the antenna array characteristics. The importance of performing the beamforming tests is that a clear picture of the beamforming capabilities and limitations of the antenna could be obtained as well as information necessary to successfully implement the digital beamforming circuitry that will be used in the final design.

The goal of this master thesis project is the design of a series of passive beamforming feeding networks to steer the main beam of the Galileo antenna array in a set of different fixed directions to evaluate its performance under such conditions. This set of directions has been chosen based on a study of the antenna characteristics in order to obtain a representative range of beamforming conditions.

In brief, the main objectives of this work are:

- To review the microstrip antenna, passive microwave circuit, transmission line, antenna array and phased array theory.
- To review the different beamforming algorithms for side-lobe level and interferer reduction as well as precise beam pointing.
- To perform an analysis of the mutual coupling and beamsteering limits of the antenna array, necessary to decide which beamforming cases are to be designed and tested.
- To calculate the optimal excitation coefficients for the different beamforming cases selected.
- To design, construct, and test a series of passive beamforming feed networks to provide the antenna array elements the amplitudes and phases for the test cases.
- To test the passive beamforming feed networks with the complete Galileo antenna array to assess its performance and obtain the information necessary for the design of the digital beamforming circuitry.

This report is divided into 3 chapters. In chapter 2, an introduction to beamforming is given. The basic characteristics of microstrip antennas and the terminology used throughout the report are presented. Then, a series of tests performed with a linear and a planar array using a square patch element optimal at 1.37 GHz, the center frequency of the Galileo band, are used to introduce fundamental concepts needed to understand beamforming antennas and the effects of tapering distributions in the radiation pattern of the arrays.

Chapter 3 presents the most important characteristics of the Galileo antenna array and the analysis of its performance in terms of mutual coupling and beamsteering limits. The chapter starts with an

introduction to the antenna element used in the Galileo antenna array and its simulated and measured performance. Then, the modular concept of the array is introduced and its advantages discussed. Right after, the software tools and the models used for the simulations done to evaluate the performance of the antenna array in terms of mutual coupling and beamsteering limits are presented. The results of these analyses are used in order to select the beamforming cases to be tested with the beamforming power dividers. The chapter concludes with an analysis of the 'ideal' cases that are later used as reference for the design of the divider networks.

In chapter 4 the design of the beamforming power divider networks is presented. The design constraints and the way these were tackled are presented in the first place. Then, the reasons that led to the selected substrate material and the geometry adopted in the final designs are explained. A computational tool to accelerate the design of the power divider networks was implemented using MATLAB® and the algorithm used explained in detail. An example of the outputs of this program is presented afterwards. The implementation and simulation results of the power dividers models in Ansoft Designer® and HFSS is presented. The resulting output powers for each of the cases is used to feed a simplified model of the antenna array and the resulting radiation patterns are compared with the reference cases obtained in chapter 3. The chapter concludes with a brief description of the physical implementation of the power divider networks, the current stage of this project.

Finally in chapter 5 the conclusions of this work are presented, stressing on the experience gained through it, the work that is needed to fully complete it, and finally some suggestions for future work.

Chapter 2 – Fundamentals and preliminary tests

This chapter gives an introduction to the fundamentals of microstrip antennas, antenna arrays, and beamforming. Firstly, the basic terminology on these subjects is introduced. Then, more specific concepts are presented through a series of test simulations that were performed with a simple square patch antenna model. Beamforming tests were done with a 7-element linear array by steering the beam in elevation and tests in elevation and azimuth were done with a 16-element 4x4 square array. The results are presented and discussed while introducing the fundamental concepts related to beamforming.

2.1 Basic characteristics of microstrip patch antennas

Microstrip antennas are in general low-profile, conformable to planar and non-planar surfaces, mechanically robust, compatible with MMIC as well as simple and low-cost. They are also very versatile in terms of resonant frequency, polarization, radiation pattern and input impedance. Possible disadvantages are low efficiency, low power, high Q, poor polarization purity, and poor scan performance spurious feed radiation and very narrow frequency bandwidth [1]. In recent years numerous developments have been done to overcome these disadvantages as the use of microstrip antennas is very convenient for many applications.

Typically a patch consists of a very thin metallic strip placed a small fraction of a wavelength above a ground plane. The space in between can be filled with air or a dielectric substrate. The radiating elements and the feeding are usually photoetched on the dielectric substrate. The patch can have almost any kind of shape; it can be square, rectangular, circular, elliptical, triangular, etc [1]. Radiation from a rectangular patch is similar to the radiation from two slots, at the left and right edges of the patch as most of the surface current accumulates there. A picture of a typical rectangular microstrip antenna element can be seen on Fig. 2.1 below.

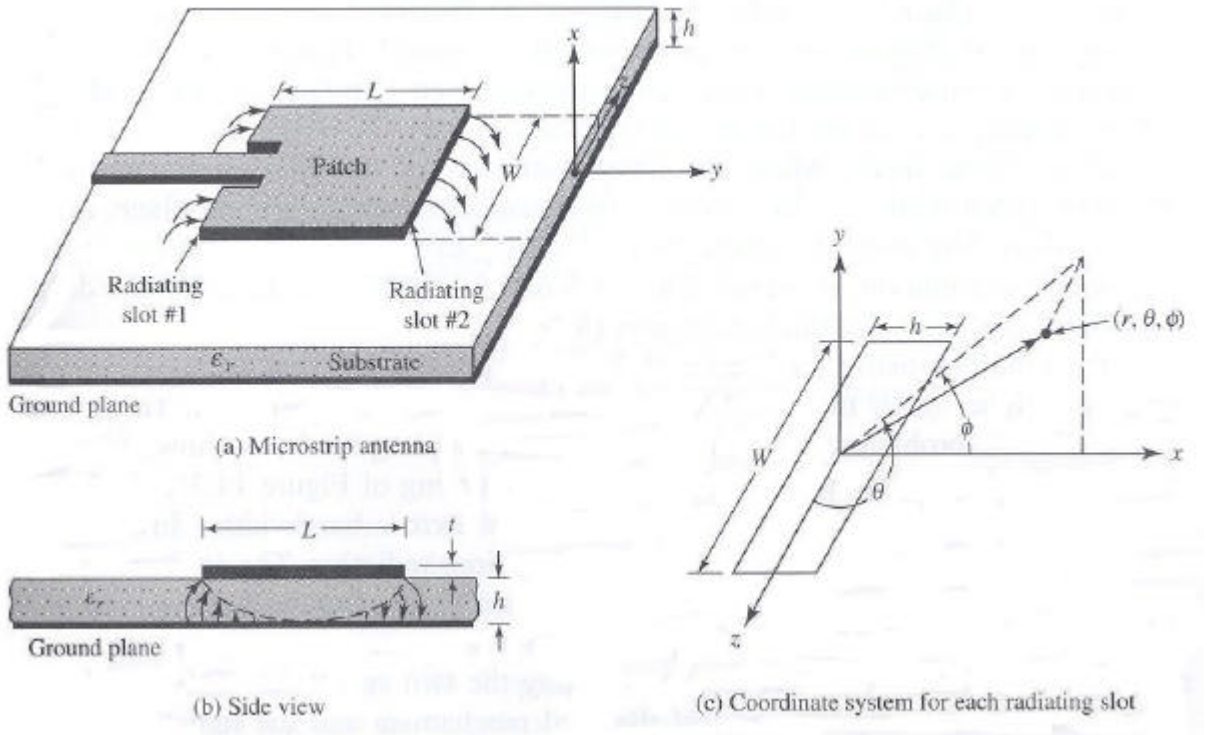

Fig. 2.1 Rectangular microstrip antenna element.

2.1.1 Feeding Methods

The feeding methods typically used for microstrip antennas are microstrip line, coaxial probe, aperture coupling and proximity coupling. These are shown in Fig. 2.2 below.

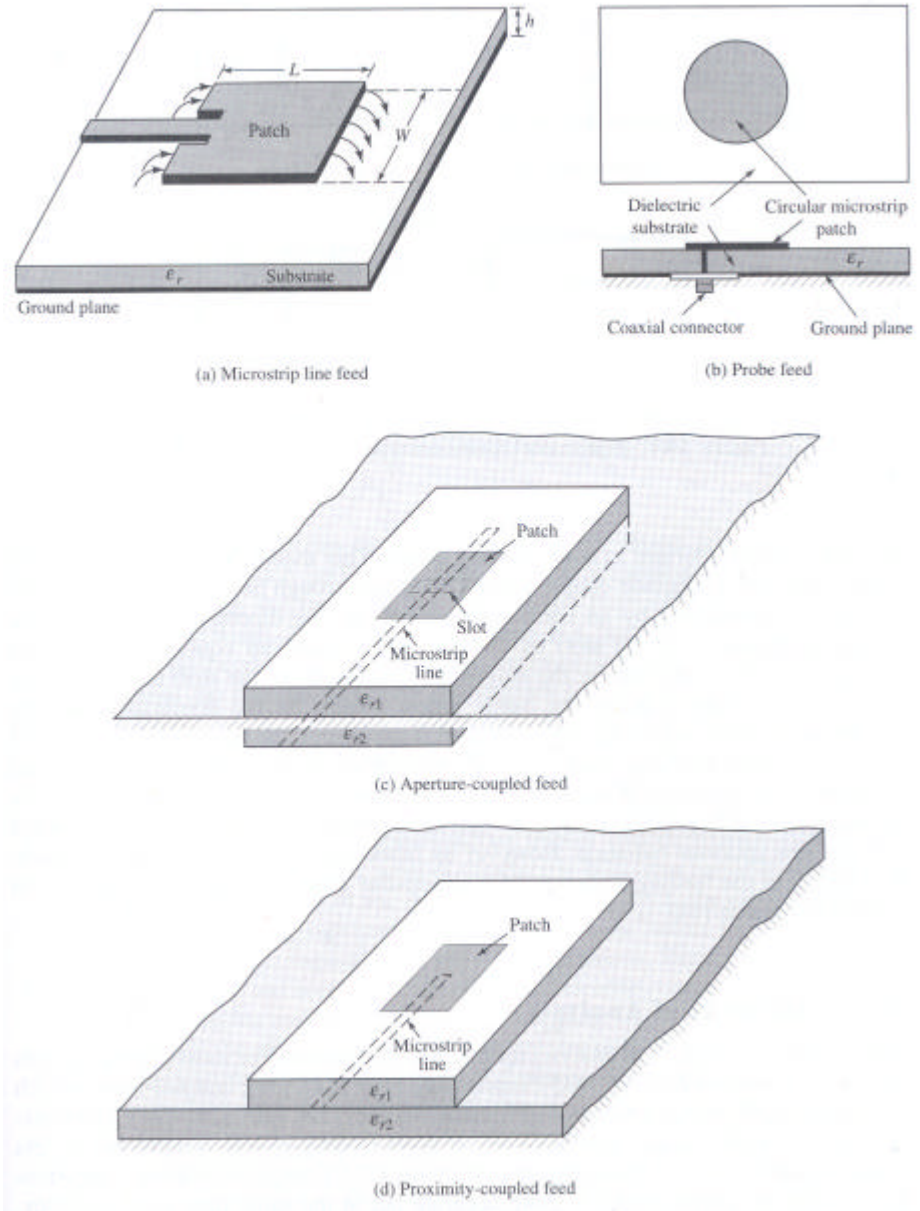

Fig. 2.2. Four different feeding methods for microstrip antennas.

Microstrip feed line is a conducting strip of smaller width compared to the patch. The patch is directly excited from the microstrip line. The feed network and patch radiators are on the same layer, therefore there is no need for soldering or making holes in the substrate. It is easy to fabricate and match by controlling the inset position. However as the substrate thickness increase, surface waves and spurious feed radiation increase, which limits the bandwidth to 2 – 5 %.

Probe-fed is a coaxial probe coming up through the ground plane. It is easy to fabricate and match while having low spurious radiation. The major disadvantage of this method is that it generally has a small bandwidth, in particular when using substrates thicker than 0.02 λ_0.

Aperture coupling overcomes the disadvantages of the above methods. It uses two substrates separated by a ground plane. On the bottom substrate there is a microstrip feed line whose energy is coupled to the upper patch through a slot on the ground plane. This arrangement allows reducing ohmic losses and increases bandwidth considerably. Typically a high dielectric material is used on the bottom substrate, and a thick low dielectric constant material for the top substrate. The ground plane also isolates the feed from the radiating element and minimizes interference of spurious radiation for pattern and polarization purity. Controlling the width of the feed line and the length of the slot allows matching. The disadvantage of this feeding method is that it causes undesired resonances in the feed line layers [1].

2.2 Beamforming antenna array basics

This section presents the basic terminology to understand beamforming antenna arrays. Some of the presented terms are used throughout this work so it is important to familiarize with them. All the concepts are marked in *italic*.

2.2.1 Basic terminology on beamforming antenna arrays

The radiation pattern of a single-element antenna is usually wide and with low directivity. For applications like satellite communications it is desirable to have very high gains as the distance among transmitter and received is considerably large. The directivity (D) for a given frequency can be controlled by increasing the antenna's aperture area as:

$$D = \frac{4pA_{Eq}}{l^2} \tag{2.1}$$

Where λ is the wavelength at the operating frequency and A_{Eq} is the equivalent aperture area, equal to the product of the physical aperture area and the antenna efficiency.

One way to increase the aperture area is by placing several individual antenna elements in an electrical and geometrical configuration which can be referred to as an array [1]. Such configuration provides flexibility to shape the resulting radiation pattern to have maxima and minima in different 'custom' directions. The signals fed on different elements of an antenna array are combined to form a single radiation pattern. The process of combining these signals to produce a desired radiation pattern is known as *beamforming*. If the antenna elements are fed with identical amplitudes and phases the beam pointing position will be orthogonal to the array plane, such configuration is called a *broadside array* [2].

The direction where the radiation pattern of the array has its maximum gain is called the *beam pointing position*. The place where the array radiation pattern goes down to a low value on both sides of the beam pointing position is called a *null*. The pattern between the two nulls on either side of the beam pointing direction is known as the *main lobe*. The width of the main lobe between the two halfpower points is called *the half-power beamwidth*. A smaller beamwidth can be achieved with a larger array. The distance between the two farthest elements in the array is known as the *aperture of the array* [2].

The beam pointing position might be changed by mechanically moving the array. This is called *mechanical steering*. Beamsteering can also be accomplished by delaying the signals fed into the antenna elements before combining them. This procedure is known as *electronic steering* [2]. The required delay can be accomplished passively by using phase shifters, by inserting varying lengths of coaxial cables between the antenna elements and the combiner, or by using beamforming power divider networks such as the ones presented in this project. Modern active systems use digital signal processors to emulate these effects.

Adjusting only the phase of signals from different elements to point the beam is the conventional method of beamforming. If the amplitude of each signal is the same, the shape of the radiation pattern

is fixed even when the main beam is steered from broadside. This means that the relative positions of the side lobes with respect to the main lobe do not change. The radiation pattern can be changed by adjusting the amplitude and phase of the signal fed into each antenna element. The number of elements in the array is a very important parameter as the amount of change possible depends on it.

The amplitude and phase applied to each array element is a complex quantity and throughout this work is referred to as *excitation coefficient*. If there is only one element, there is no way to change the pattern of an antenna even if the excitation changes. With two elements, however, changing the excitation coefficient of one element relative to the other might change the pattern. One null in the direction of an interferer, or one maximum in the direction of the desired signal can be produced anywhere in the pattern. Likewise, with three elements, two positions may be specified, and so on. Therefore, with an *n*-element array, one is able to specify *n*-1 positions. This characteristic of an *n*-element array is known as the *degree of freedom of the array* [2].

This is a property of great importance of beamforming arrays as it may be used to cancel unwanted signals operating at the same frequency as that of the desired signal, if these are not in the direction of the desired source. In the case where the directions of the interferences are known, it is possible to cancel them by placing nulls in these directions and at the same time to steer the main beam in the direction of the desired signal. This operation is usually known as *null beamforming* [2].

2.3 Beamforming tests

This section presents more specific concepts through a series of test simulations that were performed with a simple square patch antenna model. Beamforming tests were done by steering the main beam in elevation with a 7-element linear array and in elevation and azimuth with a 16-element 4x4 square array. These tests served a double purpose as they allowed studying the basic principles of beamforming and allowed to get familiar with the main simulation tools used throughout this project: Ansoft Designer® and HFSS®.

2.3.1 Optimized Test Patch

A simple narrowband probe-fed square patch optimal at 13775 GHz (the center frequency of the Galileo band) with linear polarization was designed in Designer in order to get familiar with the beamforming techniques by using it in linear and planar arrays. The physical layout is shown in Fig. 2.3.

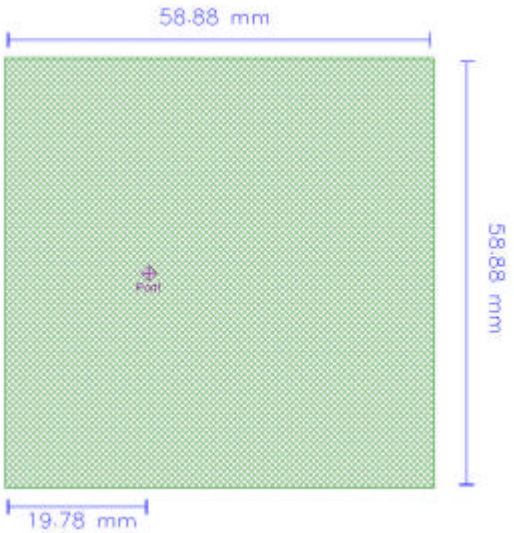

Fig. 2.3. Optimized test patch.

The feeding is done by a coaxial probe with a 1 mm diameter on the 100 Ω input impedance point as it was found to be optimal. The dielectric used was Rogers 4003 with a 1.6 mm thickness. The return loss and gain at the center frequency can be seen in Fig. 2.4. It can be observed that there is a good impedance matching at the design frequency and that gain is about 5 dB at broadside.

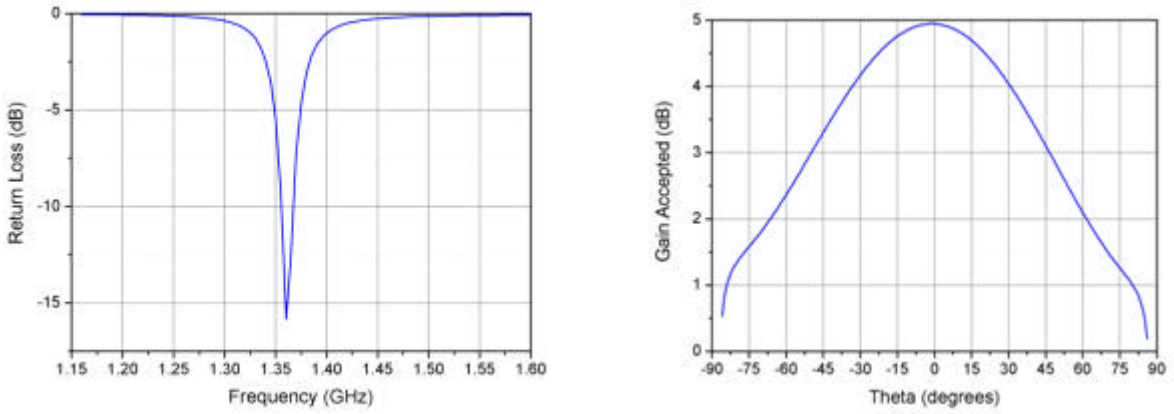

(a) (b)

Fig. 2.4. Return loss for optimized patch (a) and its gain at 1.375 GHz (b).

2.3.2 Test Linear Array

A seven element linear array with λ/2 distance among elements was simulated and is shown in Fig. 2.5. Seven elements were chosen in order to provide with sufficient flexibility while keeping the structure as simple as possible. The purpose of this test was to study the beamsteering properties of the array in one dimension.

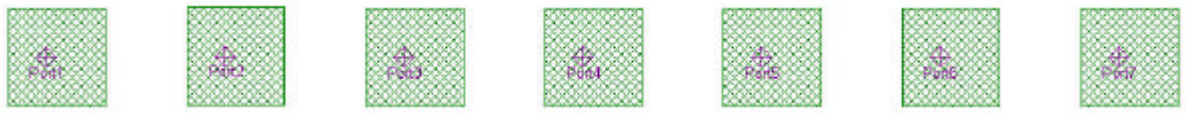

Fig. 2.5. The test linear array.

2.3.2.1 Array factor, pattern multiplication property, and relative phases

For a uniform array the total field is the product of the array factor of the isotropic sources by the field of a single element at a reference point [1].

$$E_{total} = E_{SE} \cdot AF \tag{2.2}$$

The array factor is given by:

$$AF = \sum_{n=1}^{N} e^{j(n-1)y} \tag{2.3}$$

Where N is the number of elements in the array and:

$$y = kd\cos\theta + \beta \tag{2.4}$$

Where d is the distance between elements, θ is the elevation angle and β is the difference in phase excitation between elements. It is evident from the above formulas that the array factor is a function of the distance between elements and the phases of the excitations. Equation 2.2 is known as the pattern multiplication property of uniform arrays and is exemplified graphically in Fig. 2.6 by the resulting far-field radiation patterns of a simple case.

If the reference point is placed on the physical center of the array, the normalized array factor for a linear N-Element array can be expressed as:

$$(AF)_n = \frac{1}{N}\left[\frac{\sin\left(\frac{N}{2}y\right)}{\sin\left(\frac{1}{2}y\right)}\right] \tag{2.5}$$

The direction of maximum gain in the array is controlled by the relative phases between different antennas. It can be shown that if the maximum radiation is required to be pointed at an angle θ_0 between 0° and 180°, the phase excitation between elements β should be:

$$y = kd\cos\theta_0 + \beta = 0 \Rightarrow \beta = -kd\cos\theta_0 \tag{2.6}$$

The phase on each of the elements is then set in such a way that the output fields are added in phase in the direction where the maximum radiation is needed.

A uniform change in the relative phases using the property in Equation 2.6 is used on the test linear array presented earlier to observe the beamsteering effects in one dimension. Four different tapering distributions (uniform, binomial, Taylor one-parameter, and Chebyshev) and four different elevation angles (broadside, close to broadside, middle elevation, and close to end-fire) were chosen to introduce and observe the concepts of side-lobe level suppression, beam broadening, and grating lobes.

Tables 2.1 to 2.4 show the excitation coefficients for each case.

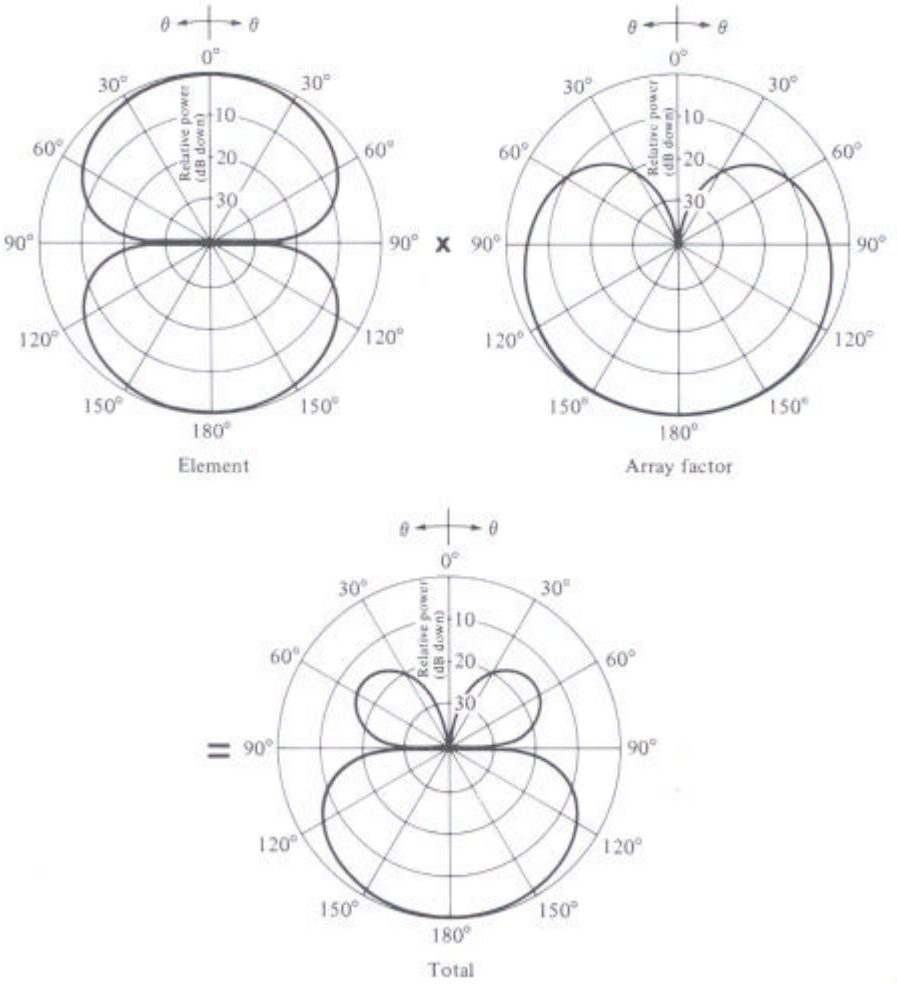

Fig. 2.6. Example of the pattern multiplication property. The total field is the product of the element pattern and the array factor.

Case A: Broadside array

2.3.2.2 Effects of tapering distributions

The broadside array results in Fig. 2.7 (a) show the effects that different tapering distributions have on the resulting radiation pattern. The best directivity is achieved when using a uniform distribution. Nevertheless the side lobe level is around -13 dB which might be too high for some applications. The binomial distribution shows an exceptional performance in terms of side lobe level suppression but leads to the broadest main lobe among the studied distributions. The Taylor one-parameter distribution shows monotonically decreasing side lobes below -20 dB. Finally, Chebyshev distribution keeps the side lobe level below -20 dB while causing only a small broadening of the main beam.

Table 2.1. Excitation coefficients for broadside array.

Patch	1	2	3	4	5	6	7
Amplitude Uniform	1	1	1	1	1	1	1
Amplitude Binomial	0.05	0.3	0.75	1	0.75	0.3	0.05
Amplitude Taylor 1P	0.35	0.66	0.9	1	0.9	0.66	0.35
Amplitude Chebyshev	0.54	0.69	0.91	1	0.91	0.69	0.54
Phase(°)	0	0	0	0	0	0	0

Case B: Beam pointed at q = 20°

In Fig. 2.7 (b) it can be observed that the beam pointing position is precisely at θ = 20°. Tests for angles between 0 and 35 degrees were done and showed a similar behavior in terms of precision. Once more the best side lobe level reduction was achieved with a Taylor distribution and the smallest broadening of the main beam with a Chebyshev distribution.

Table 2.2. Excitation coefficients for array pointing at θ = 20°.

Patch	1	2	3	4	5	6	7
Amplitude Uniform	1	1	1	1	1	1	1
Amplitude Binomial	0.05	0.3	0.75	1	0.75	0.3	0.05
Amplitude Taylor 1P	0.35	0.66	0.9	1	0.9	0.66	0.35
Amplitude Chebyshev	0.54	0.69	0.91	1	0.91	0.69	0.54
Phase(°)	-175.31	123.17	61.56	0	-61.56	-123.17	175.31

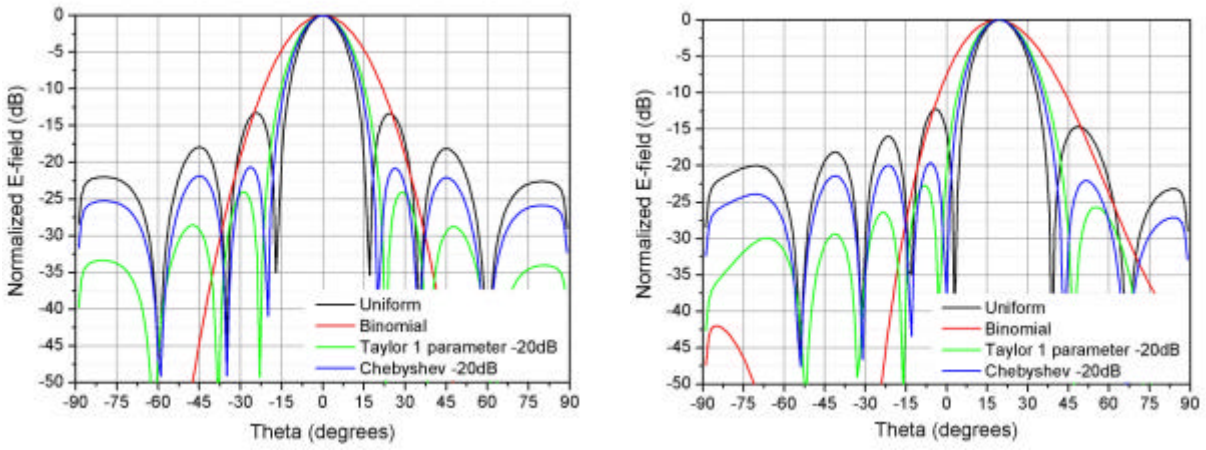

Fig. 2.7. Normalized radiation patterns: linear array pointing at broadside (a), linear array pointing at θ = 20° (b).

Case C: Beam pointed at q = 50°

Many effects related with beamforming can be observed in Fig. 2.8 (a). Firstly, the maxima are pointing at a smaller angle than expected, being more evident in the Binomial distribution. This effect is mainly due to the radiation pattern of the single element whose gain decreases rapidly at low elevation angles (at θ = 50° is about 2.6 dB below that of broadside) as it can be seen in Fig. 2.4 (b). In addition, phase and amplitude errors induced by mutual coupling between elements can also lead to errors in beam pointing.

Table 2.3. Excitation coefficients for array pointing at θ = 50°

Patch	1	2	3	4	5	6	7
Amplitude Uniform	1	1	1	1	1	1	1
Amplitude Binomial	0.05	0.3	0.75	1	0.75	0.3	0.05
Amplitude Taylor 1P	0.35	0.66	0.9	1	0.9	0.66	0.35
Amplitude Chebyshev	0.54	0.69	0.91	1	0.91	0.69	0.54
Phase(°)	53.66	-84.22	137.88	0	-137.88	84.22	53.66

2.3.2.3 Beam broadening factor

Besides the effects mentioned earlier, an evident broadening of the main beam can be observed in the radiation patterns of Fig. 2.8. The beam broadening factor (BB) is a dimensionless quantity proportional to the scan angle θ_{scan} [3],

$$BB \propto \frac{1}{\cos q_{scan}} \tag{2.7}$$

so the bigger the scan angle the larger the beam broadening.

An increase of the side lobe level above the -20 dB specified for the Chebyshev tapering can also be observed. This could be explained by the fact that the position of the coefficients of the tapering distributions remains unchanged regardless of the angle pointed at. Thus surplus energy is fed on patches that are not on the direction of the main beam and too little energy on those of the desired beam pointing position.

Case D: Beam pointed at q = -75°

It can be observed in Fig. 2.8 (b) that a grating lobe about 2 dB below the main lobe appears on the right hand side of the graph, thus creating an undesirable condition.

2.3.2.4 Grating lobes

The appearance of grating lobes depends on the choice of the spacing between elements, since the array factor function is proportional to it. The function has maxima at multiples of 2π, therefore if the element spacing exceeds a certain distance, grating lobes will arise. When pointing at broadside as in Fig. 2.9, the grating lobe in the array factor function (solid line) is suppressed by the null of the element pattern (dashed line). Nevertheless, if the array is pointed at a different angle then the grating lobe as in Fig. 2.10 moves away from the null and can cause important levels of radiation in undesired directions. The condition to avoid grating lobes for a given angle and frequency is:

$$\frac{d_x}{l_0} \leq \frac{1}{1+\sin q_{scan}} \tag{2.8}$$

Where d_x is the distance between elements, λ_0 is the wavelength at the given frequency and θ_{scan} is the scan angle. This will assure that the nearest grating lobe is at the horizon. This condition requires inter-element spacing equal or smaller than $\lambda/2$. In most practical cases the spacing should be smaller to avoid effects such as array blindness [4]. This properties show that scanning angles close to end-fire are difficult to realize in practice as they require a very small distance between elements. The inter-element distance in the simulations made was kept constant so the appearance of the grating lobe is expected. The requirements set by Equation 2.8 might be hard to achieve especially in broadband arrays such as the Galileo Antenna Array where the inter-element distance varies considerably for the different frequencies [5].

Table 2.4. Excitation coefficients for array pointing at θ = -75°.

Patch	1	2	3	4	5	6	7
Amplitude Uniform	1	1	1	1	1	1	1
Amplitude Binomial	0.05	0.3	0.75	1	0.75	0.3	0.05
Amplitude Taylor 1P	0.35	0.66	0.9	1	0.9	0.66	0.35
Amplitude Chebyshev	0.54	0.69	0.91	1	0.91	0.69	0.54
Phase(°)	-161.6	12.27	-173.87	0	173.87	-12.27	161.6

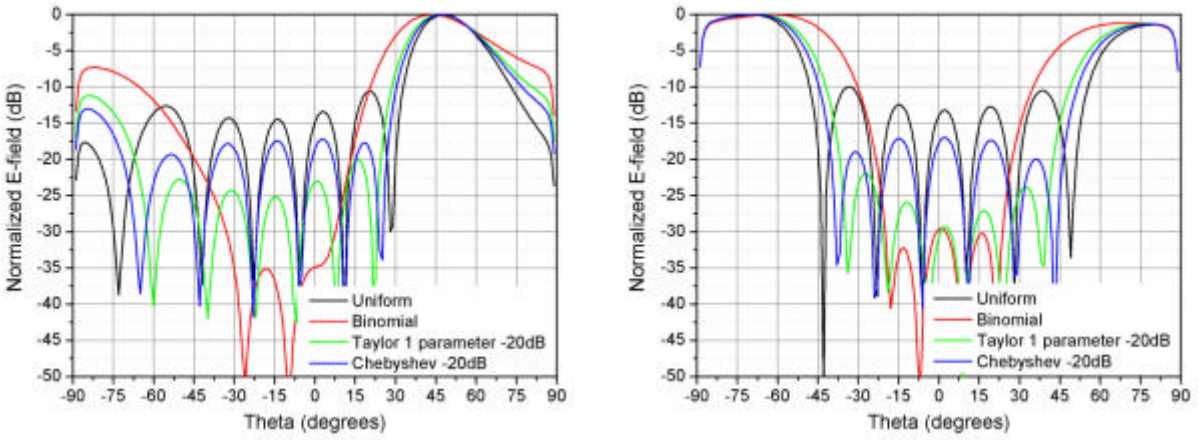

(a) (b)

Fig. 2.8. Normalized radiation patterns: linear array pointing at θ = 50° (a), linear array pointing at θ = -75° (b).

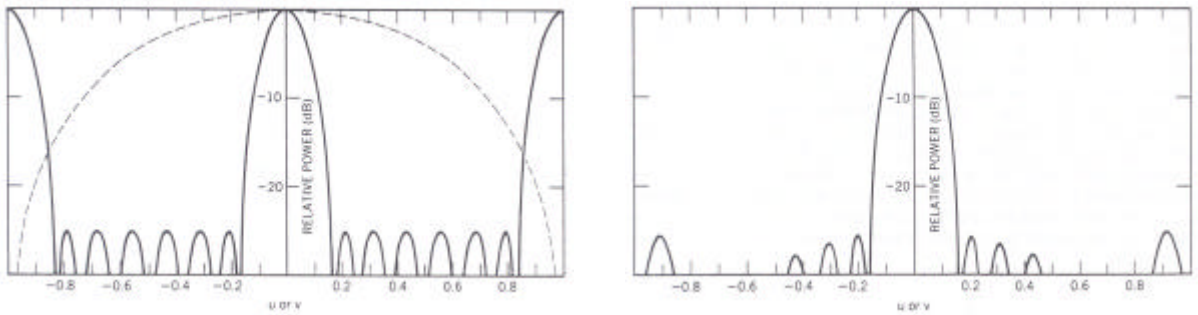

(a) (b)

Fig. 2.9. Grating lobes in a broadside array (a), element radiation pattern (dashed line) and array factor (solid line). Result (b).

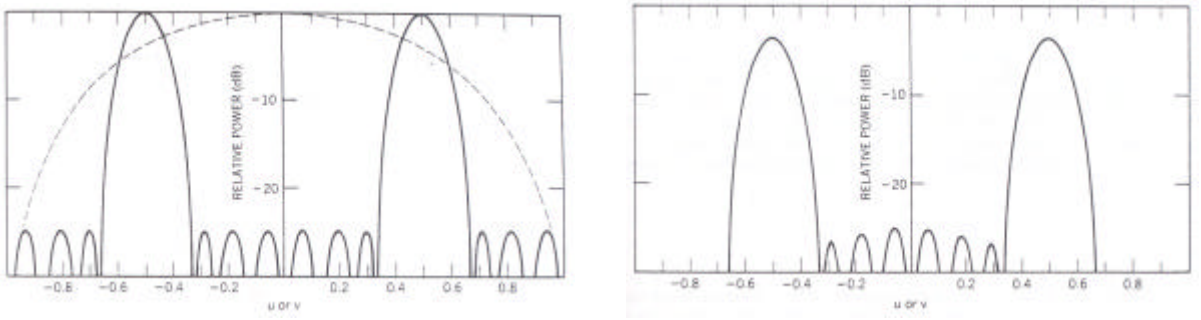

(a) (b)

Fig. 2.10. Grating lobes in an array scanned to θ = 30° (a), element radiation pattern(dashed line) and array factor (solid line). Result (b).

2.3.2.5 Limited field-of-view arrays

Using 2.8, the minimum number of elements to avoid grating lobes in a linear array of length L is [4]

$$N = \frac{L}{D_{\max}} = \frac{L}{l_0}(1+\sin q_{scan}) \tag{2.9}$$

where D_{max} is the inter-element spacing. Even though this expression might lead to the use of a small amount of elements for limited scan or broadside arrays; in practice the minimum number of elements are one per square wavelength for broadside and four for endfire arrays.

2.3.3 Test Planar Array

The planar square array of 4x4 elements shown in Fig. 2.11 using the optimized patch was designed and simulated for various scanning angles. The spacing among elements is λ/2, in both x and y directions. A planar array offers the possibility to steer the beam pointing position in both elevation and azimuth. Multiple beams and interferer nulling can also be synthesized.

2.3.3.1 Array factor and relative phases

The array factor for an N x M element rectangular array is given by [1]:

$$AF = \sum_{n=1}^{N} I_{1n} \left[\sum_{m=1}^{M} I_{m1} e^{j(m-1)(kd_x \sin\theta \cos\phi + \beta_x)} \right] e^{j(n-1)(kd_y \sin\theta \sin\phi + \beta_y)} \tag{2.10}$$

where β_x, β_y, d_x and d_y are the phase excitation and the distance between elements in x and y directions respectively, I_{m1} and I_{1n} are the excitation coefficients for each of the elements in rows and columns respectively.

The equation above shows that the pattern of the rectangular array is simply the product of the array factors in the x and y directions. In a simpler notation, it could be expressed as:

$$AF = AF_x AF_y \tag{2.11}$$

The normalized form of Equation 2.10 could be expressed as:

$$AF_n(\theta,\phi) = \left[\frac{1}{M} \frac{\sin\left(\frac{M}{2}\psi_x\right)}{\sin\left(\frac{\psi_x}{2}\right)} \right] \left[\frac{1}{N} \frac{\sin\left(\frac{N}{2}\psi_y\right)}{\sin\left(\frac{\psi_y}{2}\right)} \right] \tag{2.12}$$

where

$$\psi_x = kd_x \sin\theta \cos\phi + \beta_x \tag{2.13}$$

$$\psi_y = kd_y \sin\theta \sin\phi + \beta_y \tag{2.14}$$

From the above formulas it can be shown that if the maximum radiation is required to be pointed at an angle $\theta = \theta_0$ and $\phi = \phi_0$ the relative phase shift among elements in the x and y directions should be:

$$\beta_x = -kd_x \sin\theta_0 \cos\phi_0 \tag{2.15}$$

$$\beta_y = -kd_y \sin\theta_0 \sin\phi_0 \tag{2.16}$$

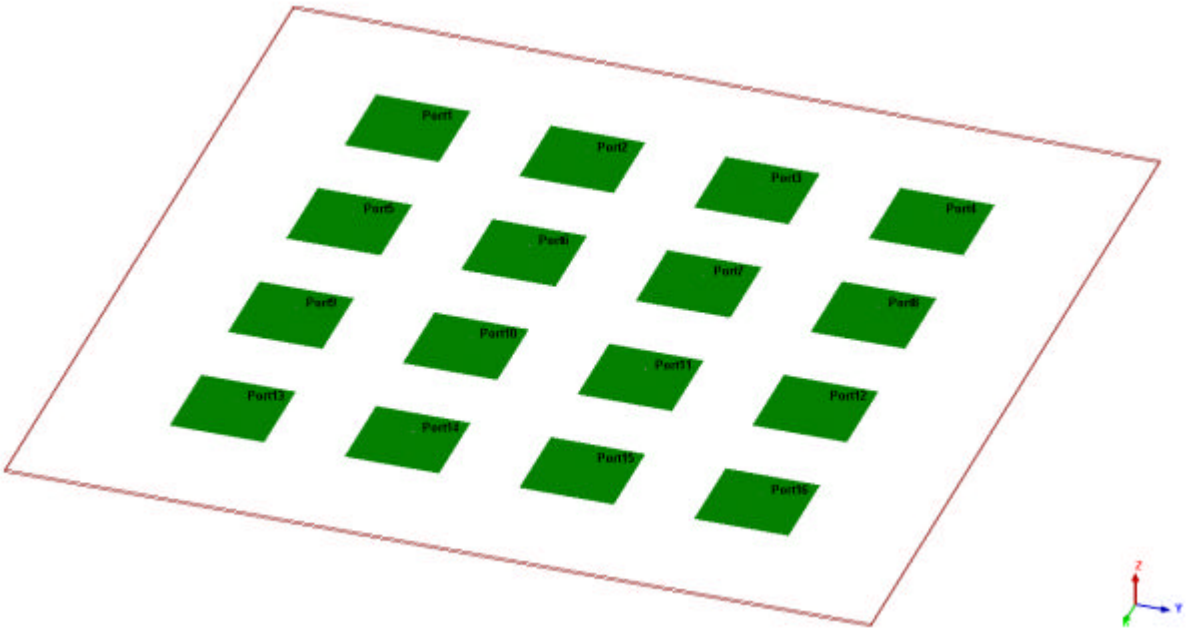

Fig. 2.11. Planar array model and orientation.

The above properties are used for testing beamsteering in azimuth and elevation. Two different pointing angles are presented using a uniform distribution and a simple Chebyshev pattern multiplication (i.e. the amplitudes for a 4-element linear Chebyshev tapering are simply cross-multiplied) for the feeding amplitudes. No optimization algorithms were used and mutual coupling between elements was not considered while calculating the excitation coefficients.

Tables 2.5 to 2.8 show the excitation coefficients for each case.

Case A: Beam pointing to $q = 50°$ and $f = 155°$

The results of this simulation can be observed in Fig. 2.12 and 2.13. It can be seen that the main beam maxima are not pointing to the expected $\theta = 50°$ but to $\theta = 43°$. This could be explained by the limitations explained earlier for the linear array cases. Besides, it can be observed that the use of the Chebyshev pattern in the feeding of the array reduces the side lobe levels considerably in comparison to the uniform distribution case. The cost of it is a reduction on the main lobe power level and a slight broadening of it. The normalization in Fig. 2.12 and 2.13 is done in relation to the maxima in the uniform distribution case.

Table 2.5. Excitation coefficients for array pointing at $\theta = 50°$ and $\phi = 155°$ using uniform distribution.

Patch	1	2	3	4
Amplitude (1-4)	1	1	1	1
Phase (°)	-129.11	172.62	114.35	56.08
Amplitude (5-8)	1	1	1	1
Phase (°)	-4.21	-62.48	-120.75	-179.02
Amplitude (9-12)	1	1	1	1
Phase (°)	120.75	62.48	4.21	-54.06
Amplitude (13-16)	1	1	1	1
Phase (°)	-114.35	-172.62	129.11	70.84

Table 2.6. Excitation coefficients for array pointing at θ = 50° and ϕ =155° using Chebyshev pattern multiplication.

Patch	1	2	3	4
Amplitude (1-4)	0.3319	0.5761	0.5761	0.3319
Phase (°)	-129.11	172.62	114.35	56.08
Amplitude (5-8)	0.5761	1	1	0.5761
Phase (°)	-4.21	-62.48	-120.75	-179.02
Amplitude (9-12)	0.5761	1	1	0.5761
Phase (°)	120.75	62.48	4.21	-54.06
Amplitude (13-16)	0.3319	0.5761	0.5761	0.3319
Phase (°)	-114.35	-172.62	129.11	70.84

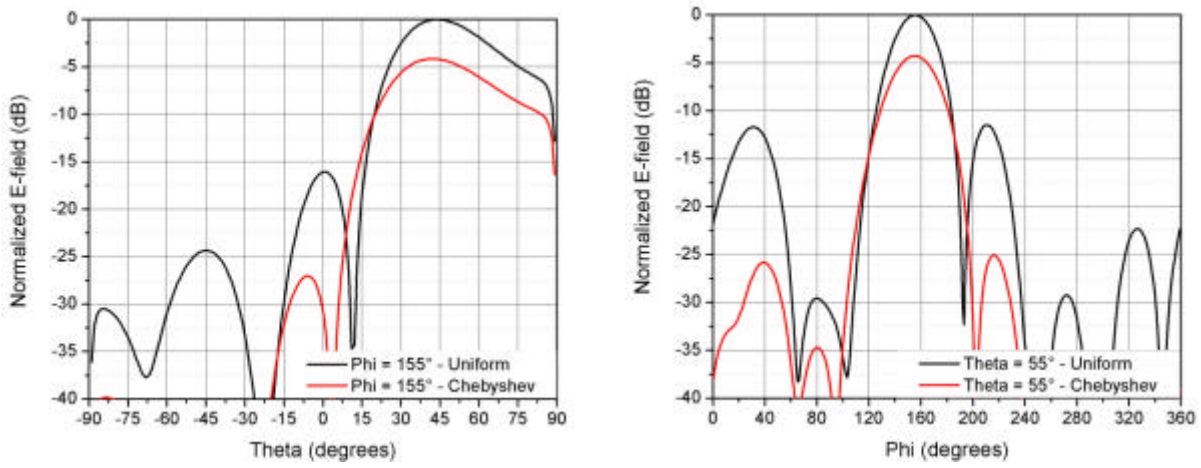

(a) (b)

Fig. 2.12. Normalized radiation patterns of planar array pointing at θ = 50° and ϕ =155° in a Phi = 155° (a) and Theta = 55° cut (b).

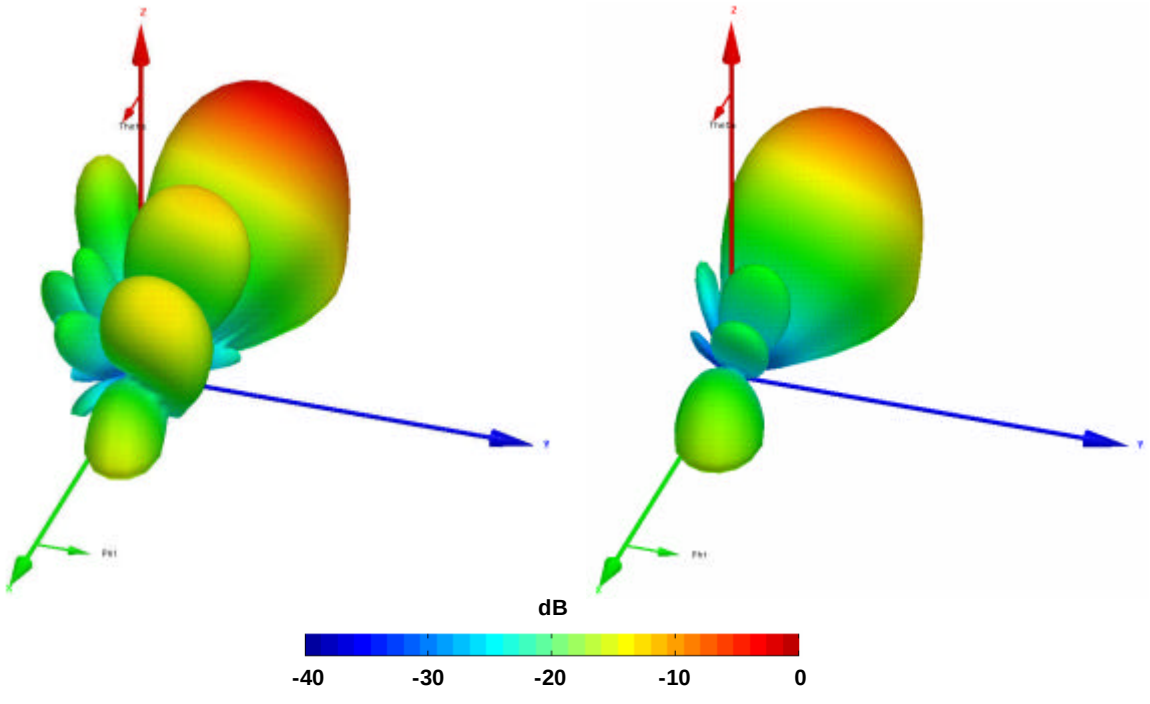

(a) (b)

Fig. 2.13. Normalized 3D radiation patterns of planar array pointing at θ = 50° and ϕ =155° for a uniform distribution (a) and Chebyshev distribution (b).

Case B: beam pointing to q = 15° and f = 315°

The results of these simulations can be observed in Fig. 2.14 and 2.15. They are good in terms of side lobe level reduction as the scan angle in elevation is close to broadside where, as discussed earlier, the Chebyshev tapering used is optimal. Nevertheless, there is an evident beam broadening that can be observed in the radiation pattern of Fig. 2.15 (b). Beam broadening is a consequence of applying any kind of tapering.

Table 2.7. Excitation coefficients for array pointing at θ = 15° and ϕ =315° using uniform distribution.

Patch	1	2	3	4
Amplitude (1-4)	1	1	1	1
Phase (°)	-16.47	16.47	49.41	82.35
Amplitude (5-8)	1	1	1	1
Phase (°)	-49.41	-16.47	16.47	49.41
Amplitude (9-12)	1	1	1	1
Phase (°)	-82.35	-49.41	-16.47	16.47
Amplitude (13-16)	1	1	1	1
Phase (°)	-115.29	-82.35	-49.41	-16.47

Table 2.8. Excitation coefficients for array pointing at θ = 15° and ϕ =315° using Chebyshev pattern multiplication.

Patch	1	2	3	4
Amplitude (1-4)	0.3319	0.5761	0.5761	0.3319
Phase (°)	-16.47	16.47	49.41	82.35
Amplitude (5-8)	0.5761	1	1	0.5761
Phase (°)	-49.41	-16.47	16.47	49.41
Amplitude (9-12)	0.5761	1	1	0.5761
Phase (°)	-82.35	-49.41	-16.47	16.47
Amplitude (13-16)	0.3319	0.5761	0.5761	0.3319
Phase (°)	-115.29	-82.35	-49.41	-16.47

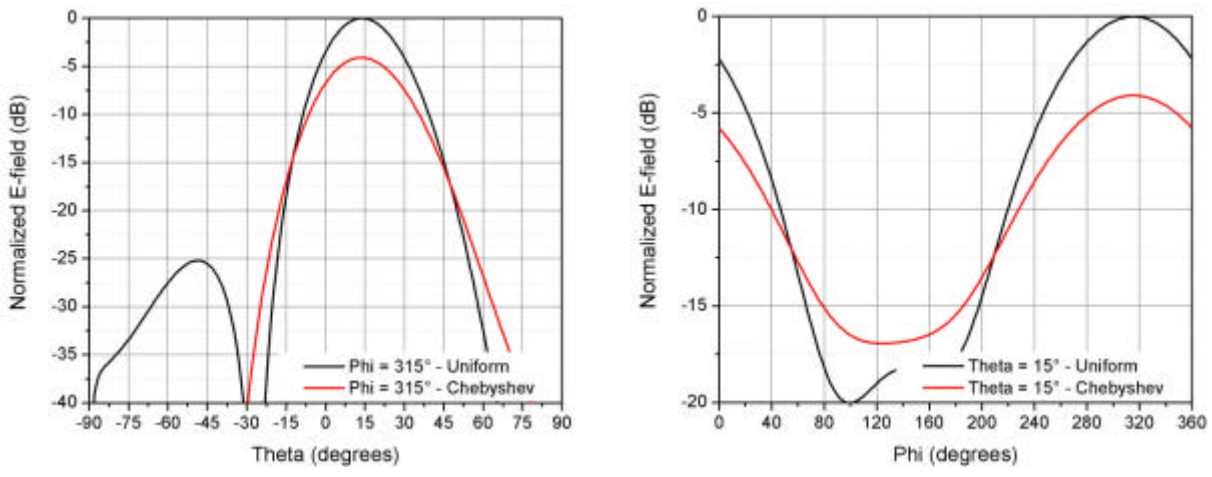

(a) (b)

Fig. 2.14. Normalized radiation patterns of planar array pointing at θ = 15° and ϕ =315° in a Phi = 315° (a) and Theta = 15° cut (b).

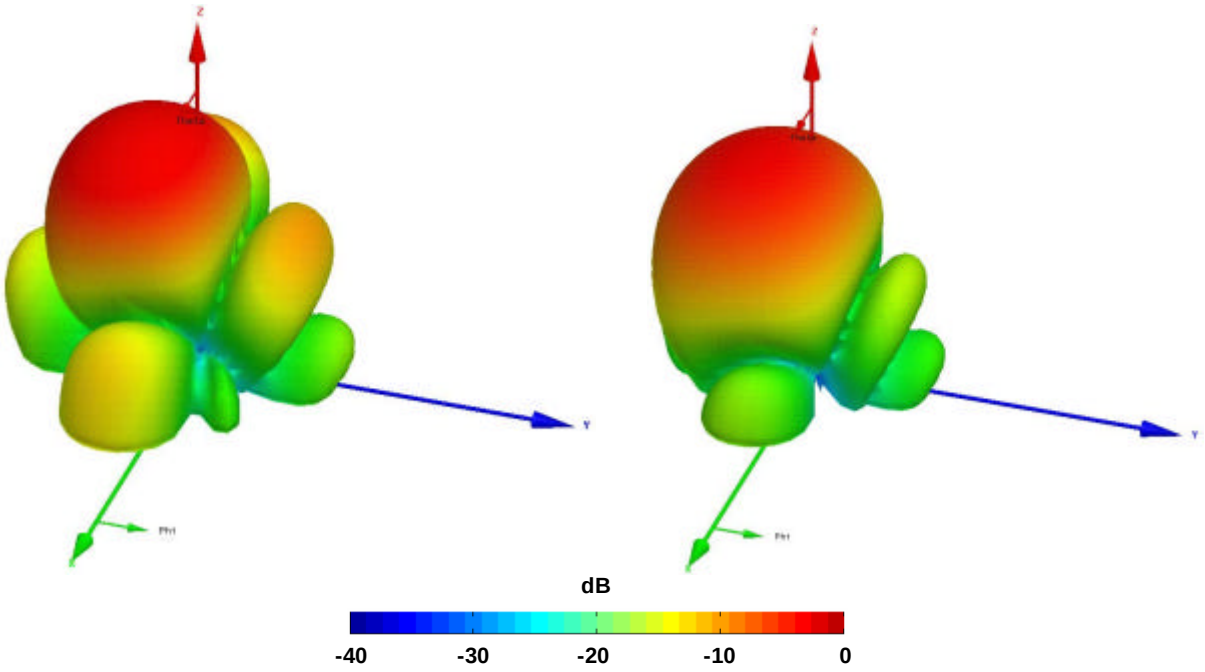

(a) (b)

Fig. 2.15. Normalized 3D radiation patterns of planar array pointing at $\theta = 15°$ and $\phi = 315°$ for a uniform distribution (a) and Chebyshev distribution (b).

2.3.4 Remarks on the results of the test arrays

Several conclusions can be drawn out of the results of the test linear and planar arrays. First of all, they were useful for introducing and proving basic concepts of beamforming. It was seen that changing the relative phases fed into the elements the beam pointing direction can be directed to anywhere in azimuth while in elevation it is limited by the physical characteristics of the array, particularly the radiation pattern of the single element. The effects of tapering distributions were shown and the advantages and disadvantages discussed. It was also seen that there is a need for an optimization algorithm to calculate the excitation coefficients fed into each of the elements; since applying simple tapering is only optimal in broadside direction. Such algorithm should take into account the angle pointed at and the mutual coupling among elements. The optimization and mutual coupling analysis of the Galileo Antenna Array is treated in chapter 3.

Chapter 3 – Beamforming analysis of the Galileo antenna array

In this chapter the most important characteristics of the Galileo Antenna Array are presented and analyzed. Before moving into the design of the beamforming power dividers it is essential to understand the structure and characteristics of the single element and the array. These characteristics are presented and the performance of the array in terms of mutual coupling and beamsteering limits is analyzed in order to decide which beamforming cases are to be implemented with the power dividers. Finally, the selected cases are analyzed using two different tools and the results are presented and discussed.

3.1 The Galileo antenna array

The Galileo smart antenna array terminal has a flexible concept that allows its use for GPS/Galileo applications. The characteristics of the single antenna element and the array are presented in this section followed by mutual coupling and beamsteering limit analyses. The in-house developed software SEQAR, used in the analyses and the calculation of the optimal excitation coefficients for the beamforming cases to be implemented is also presented in this section.

3.1.1 Single element characteristics

The single element of the Galileo antenna array is a circular microstrip patch antenna fed by means of four capacitive coupled circular plates [6], [7]. These are connected by vias to a feeding system composed by a 180° hybrid (rat-race) and two 90° hybrids that generate a progressive phase shift of 90° at the four feeding points. Such structure has proven to be broadband and provides good polarization purity over a large range of elevation angles. A schematic of the antenna element as well as a first prototype are shown in Fig. 3.1.

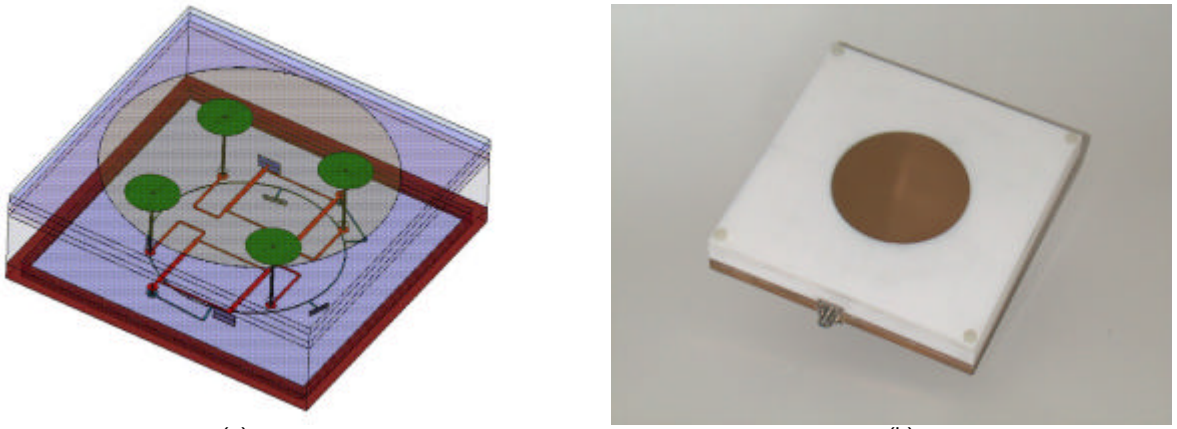

(a) (b)

Fig. 3.1. Single element (a) schematic and (b) prototype.

Two versions of this antenna element were developed; the first one with Teflon as the main substrate and the second with Rohacell foam. The complete layer structure for both versions is shown in Fig. 3.2. The diameter of the patch and feeding plates is 74.00 mm and 12.76 mm respectively for the Teflon case and 82.2 mm and 15.2 mm respectively for the foam case. The positions of the four feeding points form a perfect square around the center of the structure, as shown in Fig. 3.1(a). Its diagonal measures 52 mm for the Teflon case and 54 mm for the foam case.

A first prototype of the Teflon substrate antenna was built and measured. However, the final version uses the foam substrate because it is much lighter and offers very similar performance to that of the Teflon version. Fig. 3.3 and 3.4 show the simulated and measured parameters of the Teflon antenna.

The half power beam width of this antenna element is about 80°, which is relatively large and suitable for beamforming. Its broadside gain varies between 3 and 5 dBi along the operation bandwidth,

decreasing to not less than -3 dBi at an elevation of 30°. The simulated axial ratio is better than 3 dB for elevations higher than 30° on the whole frequency range, and about to 4.8 dB for a 15° elevation.

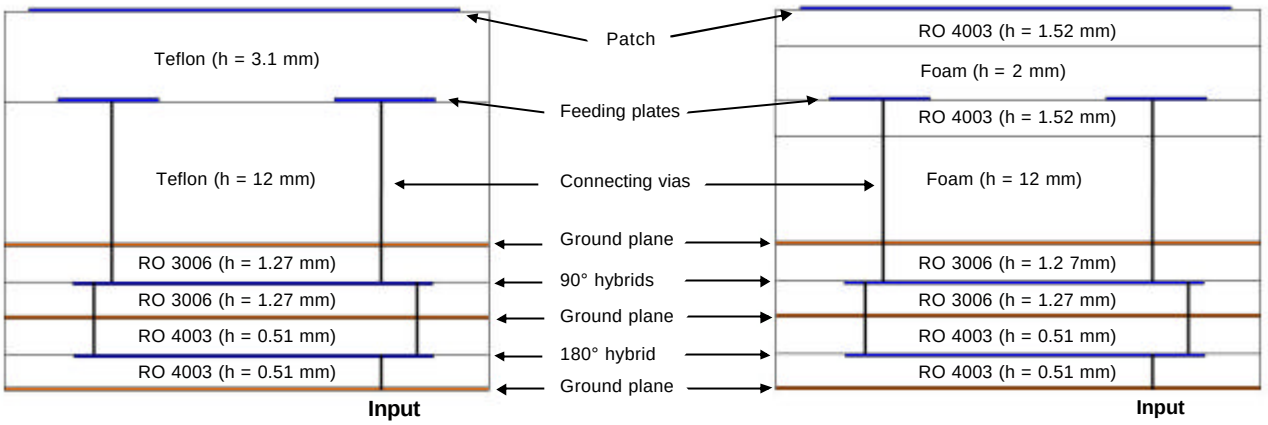

(a) (b)

Fig. 3.2. Layer structure of the single element antenna for the (a) Teflon case and (b) foam case.

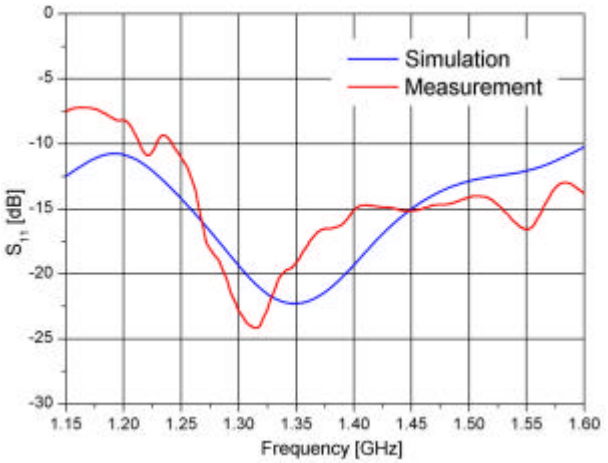

Fig. 3.3. Return loss of the Teflon prototype.

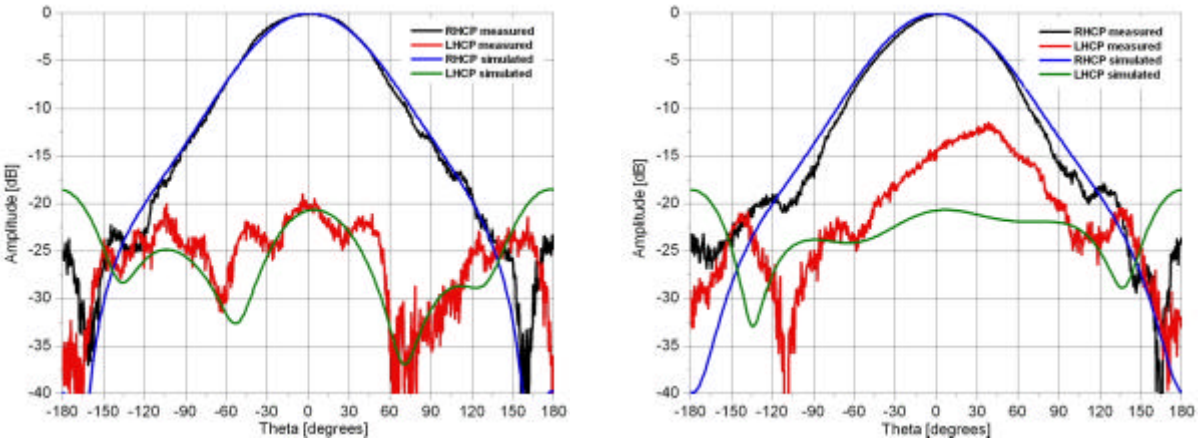

(a) (b)

Fig. 3.4. Radiation patterns at 1.37 GHz. $\phi = 0°$ (a) and $\phi = 90°$ (b) for the Teflon prototype.

3.1.2 Array Characteristics

3.1.2.1 Specifications and dimensions

The antenna array must be able to receive Galileo and GPS signals, track the visible satellites with multiple beams, and suppress interferers such as jammers and multipath signals by means of digital beamforming (DBF). A set of specifications to attain the desired performance is shown in Table 3.1.

Table 3.1. Galileo Antenna Array specifications.

Parameter	Specification
Bandwidth	1164 MHz to 1591 MHz (31%)
Return loss	-10 dB min
Polarization	RHCP
Azimuth scanning	360°
Elevation scanning	from 30° to 90° (from 0° to 30° desired)
Gain	10 dBi minimum over all scan angles (30° to 90° elevation)
Axial ratio	3 dB minimum over all scan angles (30° to 90° elevation)
Cross-polarization	15 dB minimum, 25 dB or better is desirable

The smart antenna terminal under development has a number of potential navigation applications that might set limitations in terms of size, therefore it was decided that the dimensions should not exceed 50 cm x 50 cm. This limit set, the maximum size would have been a 5x5 array using the L-band element presented. A 4x4 array was preferred as it was found that the performance is not substantially improved by the 5x5 array and the design of feeding networks and digital signal processing modules is simplified. The overall antenna array surface is 38 cm x 38 cm, as the dimensions of the element module are 95mm x 95mm.

The antenna array was designed following a modular concept, in which every part of it is a module itself. Fig. 3.5 shows the antenna array schematic in a perspective and a side view. This modular approach provides great flexibility to the array prototype and offers advantages such as the possibility of using the antenna array for passive beamforming tests by using passive beamforming networks replacing the LO networks. In addition, any part of the antenna array may be easily tested isolated from the others. The antenna modules are mounted on a frame and the RF front-end modules are connected to the bottom side of the antennas. The DC and LO modules are built separately and are fixed at the bottom of the frame. Each of these parts of the array will be treated as individual modules being the connection between them made by means of high precision coaxial cables with high phase and amplitude stability. In order to accommodate all these cable connections, there is a need for a suitable room and this is provided by a separation of approximately 10 cm between the front-end modules and the power divider network modules.

3.1.2.2 Simulation results at center frequency

In order to analyze the behavior of the whole array, a series of simulations were done at the center frequency of 1.37 GHz. The gain and axial ratio for three different cases of beamsteering at the center frequency of the operating band are shown in Fig. 3.6. A linear phase shift on the without any side lobe level suppression was applied.

The results show that due to the pattern multiplication property the main beam cannot be steered down to very low elevation angles. According to the simulations at center frequency, the maximum of the beam can only be pointed up to about 50° without causing the appearance of grating lobes. Therefore, for incoming satellite signals arriving at low elevation angles (large θ), the array antenna will steer its beam towards the maximum reachable angle and receive them in a portion of the beam with a

gain lower than that of the maximum. Simulations show that the antenna array gain can be about 8 to 10 dBi at θ = 60°, 5 dBi at θ = 75° and -5 dBi at θ = 85°. In addition, the axial ratio keeps under 3 dB up to θ = 67°.

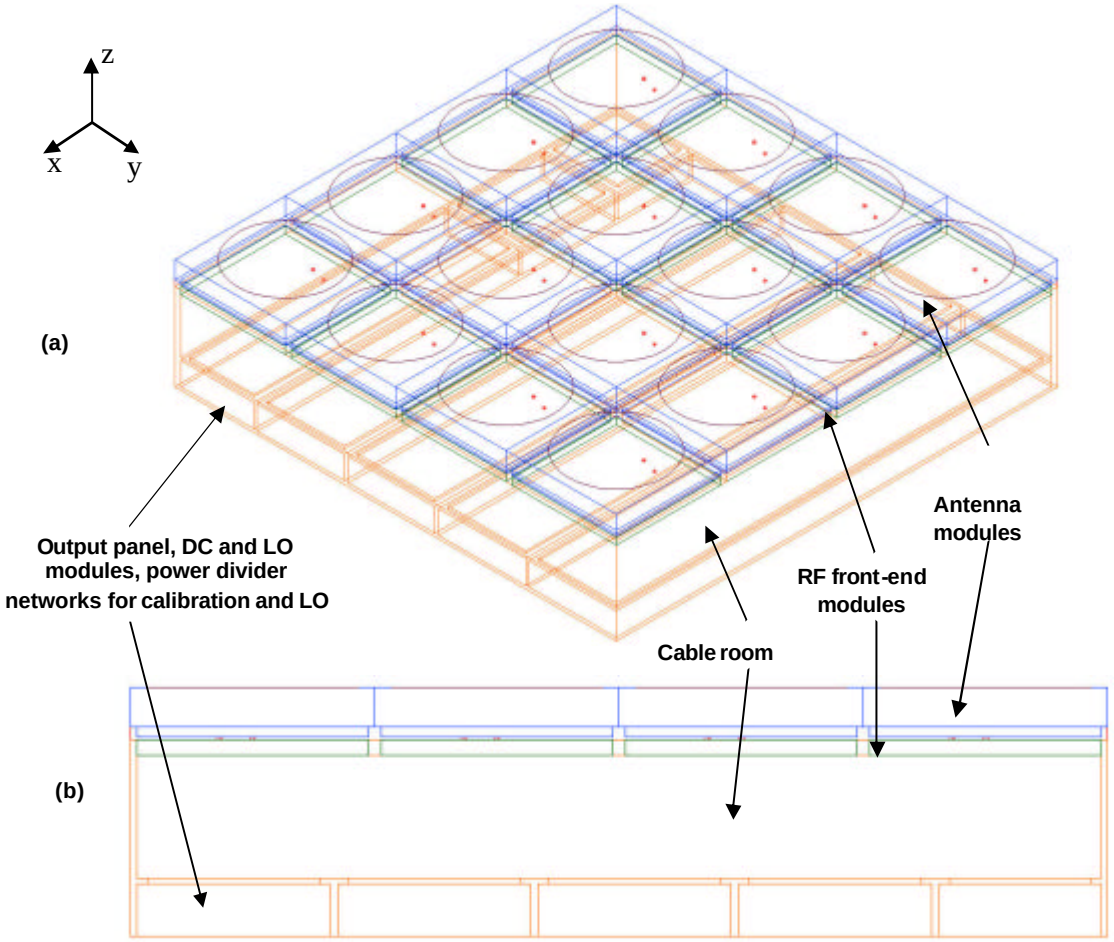

Fig. 3.5. Antenna array frame structure (a) perspective view and (b) side view.

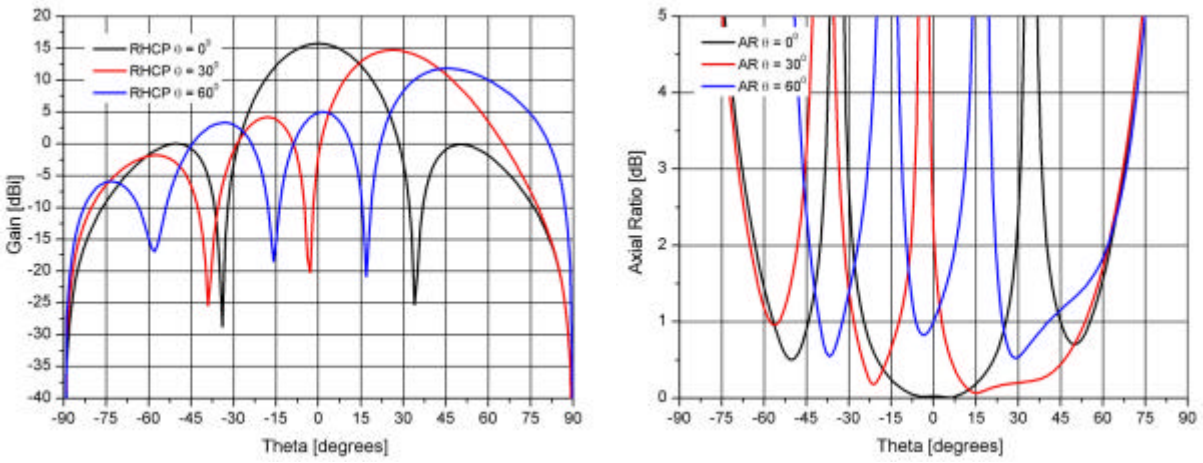

Fig. 3.6. Simulated RHCP gain (a) and axial ratio (b) with beam steering of the 4x4 antenna array at 1.37 GHz.

3.1.3 Mutual coupling analysis

Mutual coupling between elements is an important issue when dealing with antenna arrays. It influences the current configuration on each element differently, particularly if beamsteering is done. In order to account for these effects, a way to find how each element is affected and the influence it has on the whole radiation pattern is needed. This section presents how this analysis was performed for the Galileo Antenna Array.

3.1.3.1 Mutual coupling in antenna arrays

The effects of mutual coupling in antenna arrays can be better understood by means of a general example. Consider an array of small apertures located in the plane z = 0 as shown in Fig. 3.7.

If the aperture field of the individual element is assumed to have the same distribution. For the *n*th element, the tangential aperture field is

$$\mathbf{E}_{\mathbf{T}}(x_n, y_n, z_n) = \hat{\mathbf{y}} A_n e_{10}(x', y') \tag{3.1}$$

where e_{10} is the spatial distribution of the electric field in the aperture with coordinates (x', y', 0). The constant A_n is the complex amplitude of the tangential aperture field; it contains not only the applied field at the antenna aperture, but also the field due to the reflected signal at the aperture and the field induced by other array elements. The entire radiation and interelement coupling behavior for the N-element array can be described in terms of an N-by-N element scattering matrix that relates the different transmitted incident and reflected fields at each element [4].

If the array elements are excited by incident signals a_n, the reflected signals b_n at each port are given in terms of a scattering matrix as

$$[b] = \{S\}[a] \tag{3.2}$$

Where the matrix [a] is the incident signal and the matrix [b] is the reflected signals.

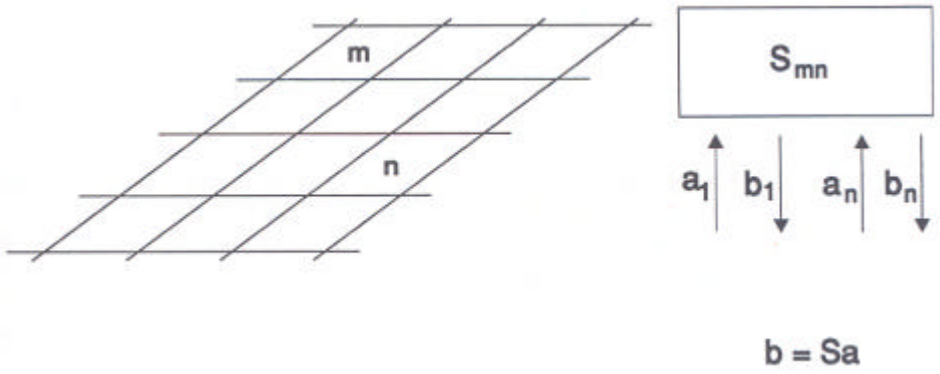

Fig. 3.7. Scattering matrix representation for mutual coupling in a generalized aperture array.

The tangential field is thus given by the sum of incident and reflected fields at the aperture. The constant A_n is hence the sum of incident and reflected signal amplitudes

$$A_n = \left(a_n + \sum S_{mn} a_n\right) \tag{3.3}$$

and the radiated field of the array is

$$\mathbf{E}(\mathbf{r}) = \frac{jk_0}{2p}\frac{e^{-jk_0R_0}}{R_0}\mathbf{f}_{\mathbf{x}}(q,f)\sum e^{-jk_0(\mathbf{r'_m}-\hat{r})}\left(a_n + \sum S_{mn}a_n\right) \tag{3.4}$$

where $f_x(\theta, \phi)$ is the pattern of an isolated element polarized transverse to the radial direction.

The array radiation equation can be analyzed in two ways. The fist one sees each element from a circuit point of view. In the mutual impedance perspective, each element is considered to radiate separately based on its aperture field E_T. To obtain a desired radiation pattern aperture fields must be controlled as a function of scan because reflection coefficients for apertures are scan-dependant. Therefore the array control is done by specifying the correct incident fields to produce the desired aperture fields in a mutually coupled environment.

In the active element pattern perspective, each element is excited with all other elements terminated in matched loads. The resulting radiation pattern $f_m(\theta, \phi)$ is the active element pattern of that element. This pattern does not change with scan, but includes all interelement coupling for all scan angles. The radiated field is thus given by

$$\mathbf{E}(\mathbf{r}) = \frac{jk_0}{2p}\frac{e^{-jk_0R_0}}{R_0}\sum a_n g_m \mathbf{f}_m(q,f) \tag{3.5}$$

where

$$\mathbf{f}_m(q,f) = \mathbf{f}_i(q,f)\left[1 + \sum S_{mn}\frac{g_n}{g_m}\right] \tag{3.6}$$

The far field expression is the sum of element excitation coefficients a_m multiplied by a time-delay factor g_m and an element pattern $f_m(\theta, \phi)$ which is now different for each element. The basic array element radiation pattern is the product of the isolated active element pattern and a space factor, which accounts for all the other coupled elements. Some of the mutual coupling terms can produce very angle-sensitive changes to the element patterns which result in distorted patterns with strong frequency dependence. The elements in the center of large arrays are usually very similar, but the ones near the edges are distorted and asymmetrical. These effects usually limit the side lobe level that can be achieved when the elements are excited with a determined tapering distribution.

3.1.3.2 Mutual Coupling in the Galileo Antenna Array

In order to evaluate the performance of the Galileo Antenna Array in terms of mutual coupling, an in-house developed Matlab program called SEQAR was used [8]. This program has a user-friendly interface as it can be seen in Fig. 3.8 that allows selecting the array size, DOA for signals, DOA for interferers, mutual coupling and decoupling matrix calculation, side lobe level suppression, and polarization. The only parameter that can not be specified is the inter-element spacing as it is fixed at 0.5λ.

The output of this program is the radiation pattern of the array, the direction of the main lobe and its directivity for a user-defined beamforming case. If the program is required to take mutual coupling into account, it requires the active element pattern (i.e. one array element excited and the rest matched) for each antenna of the array as input. The active element computations were performed using a simplified model of the antenna on the Planar EM Simulator from Ansoft Designer®. This model did not

consider the feeding system (i.e. the 180° and 90° hybrids) in order to suit the available computational resources. Hence, the feeding of the four plates shown in Fig. 3.1 (a) was done using coaxial vias with unitary amplitudes and the desired phases. The simulation model of the array is shown in Fig. 3.9.

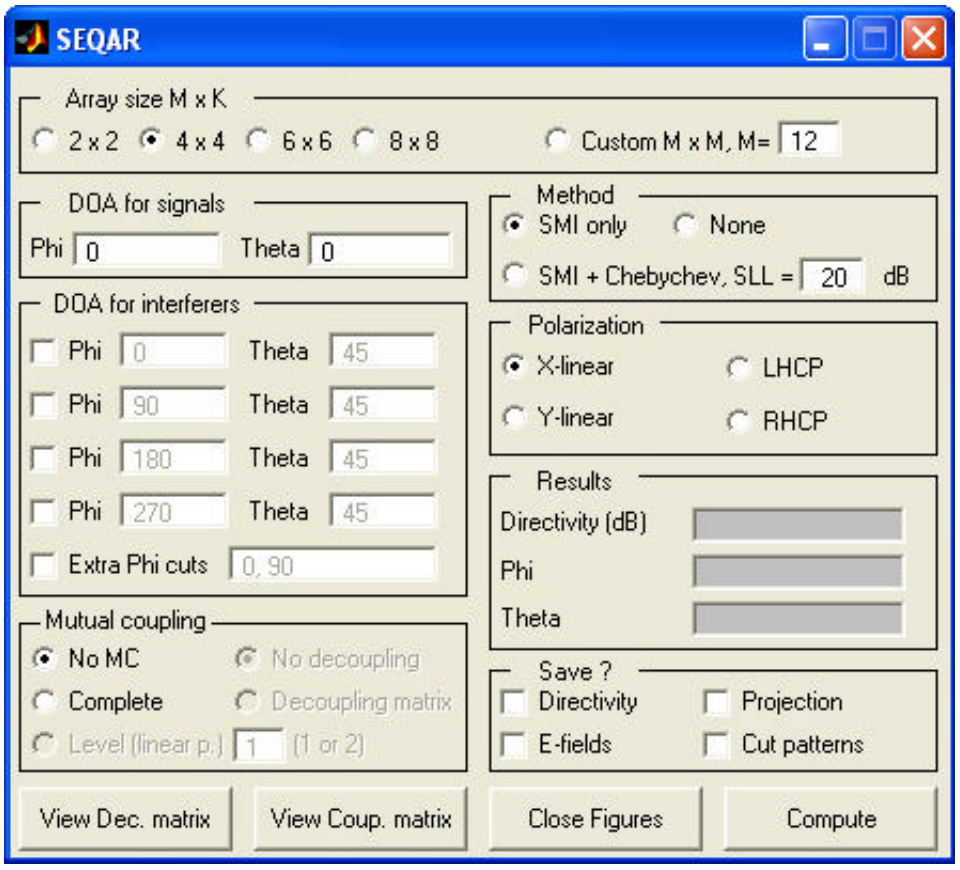

Fig. 3.8. SEQAR interface.

In order to verify the mutual coupling response of the Galileo Antenna Array, a number of simulations were done for different beamforming cases.

The simulation results without considering mutual coupling at $\phi = 45°$ and $\theta = 45°$ at 1.57 GHz are shown in Fig. 3.10. When using a side lobe level (SLL) suppression of 20 dB, the directivity was estimated to be 16.39 dBi. The axial ratio levels remain identical to that of the single element for all beamforming conditions simulated. The polarization purity is very good in the broadside direction, and a degradation for lower elevation angles is observed.

If mutual coupling is taken into account, the resulting plots at 1.57 GHz when pointing the main beam to the same point are shown in Fig. 3.11. In contrast with the uncoupled case, an overall degradation of the axial ratio is observed. The axial ratio level obtained is 3.99 dB in the direction of maximum radiation. In the case without considering mutual coupling, the corresponding value is 2.76 dB. The effects on directivity are almost negligible as the obtained value is 16.27 dBi.

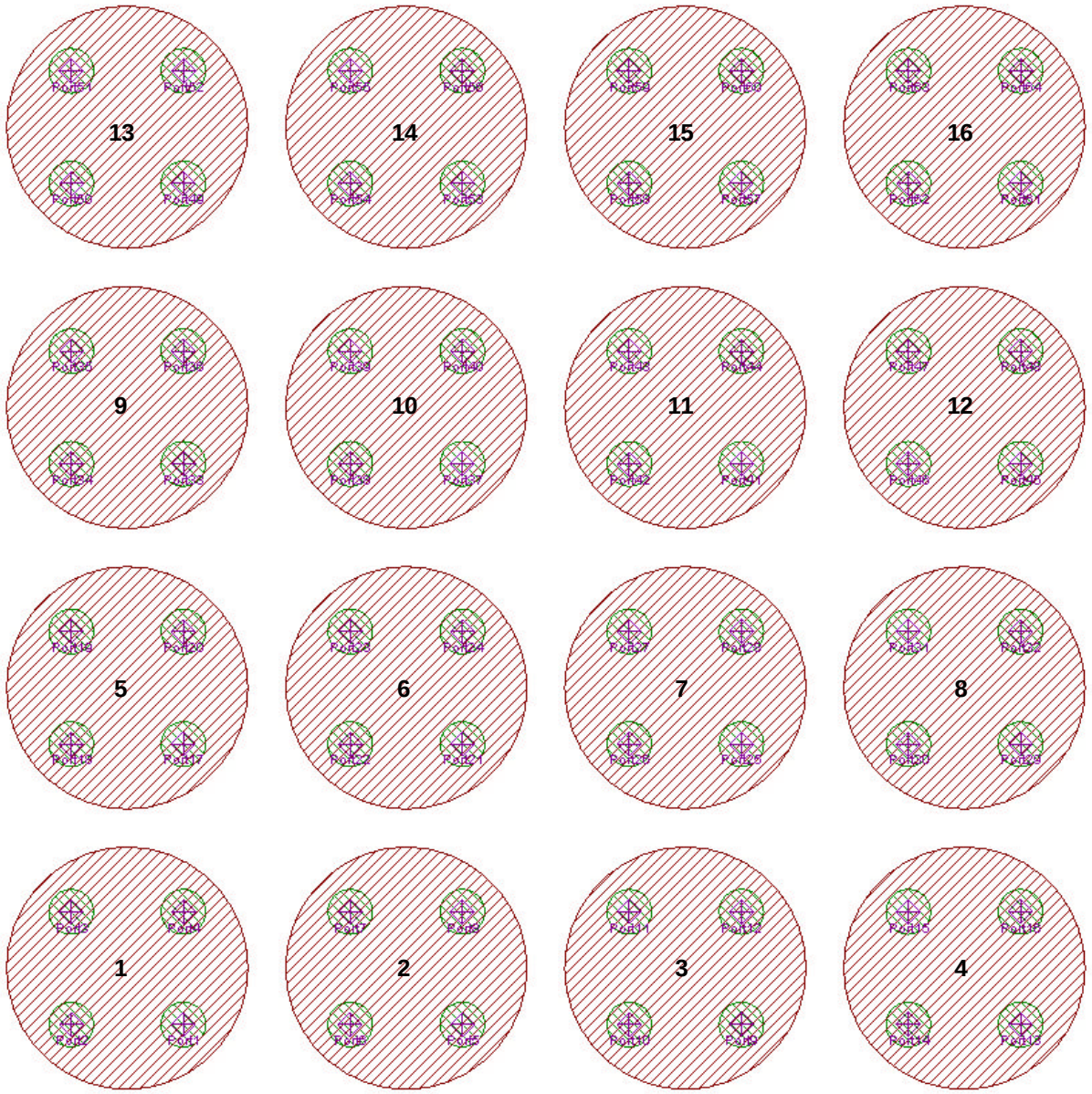

Fig. 3.9. Top view of the simplified Galileo antenna array model with element numbering.

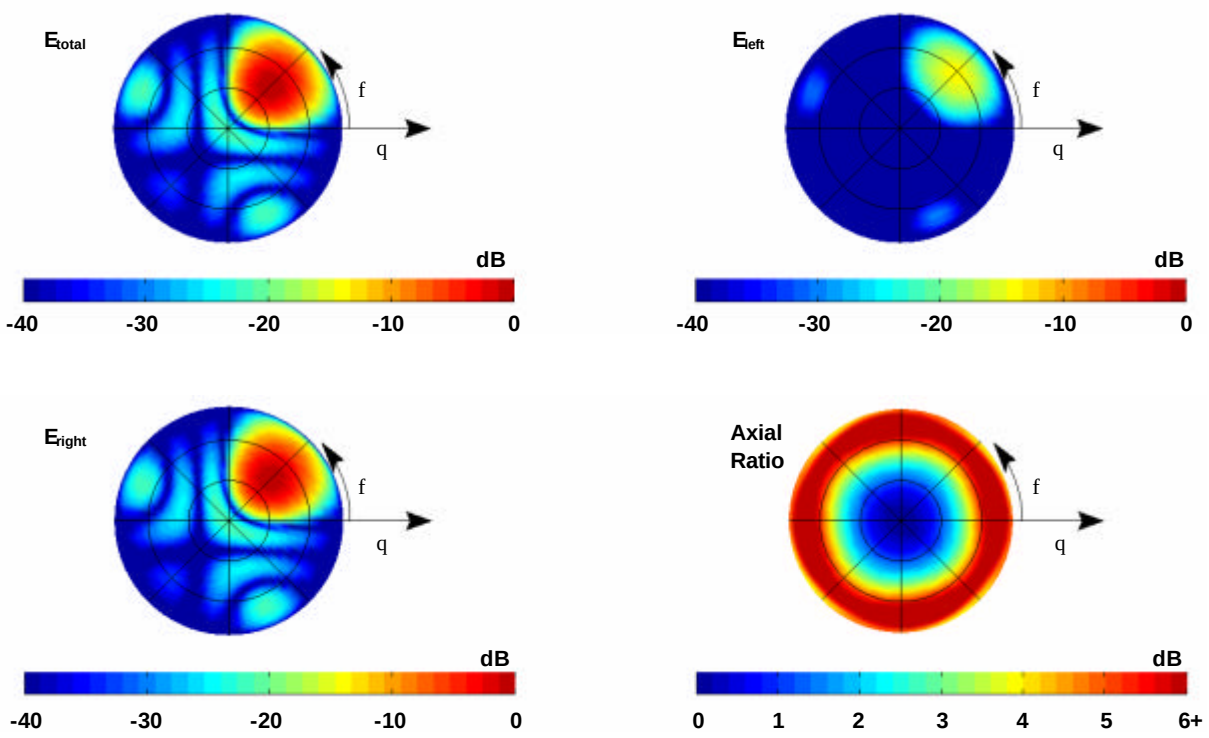

Fig. 3.10. Radiation characteristics obtained with SEQAR not considering mutual coupling with beam steered to $\phi = 45°$ and $\theta = 45°$ at 1.57 GHz and SLL suppression of 20 dB. θ varies from 0° to 90° from the center out.

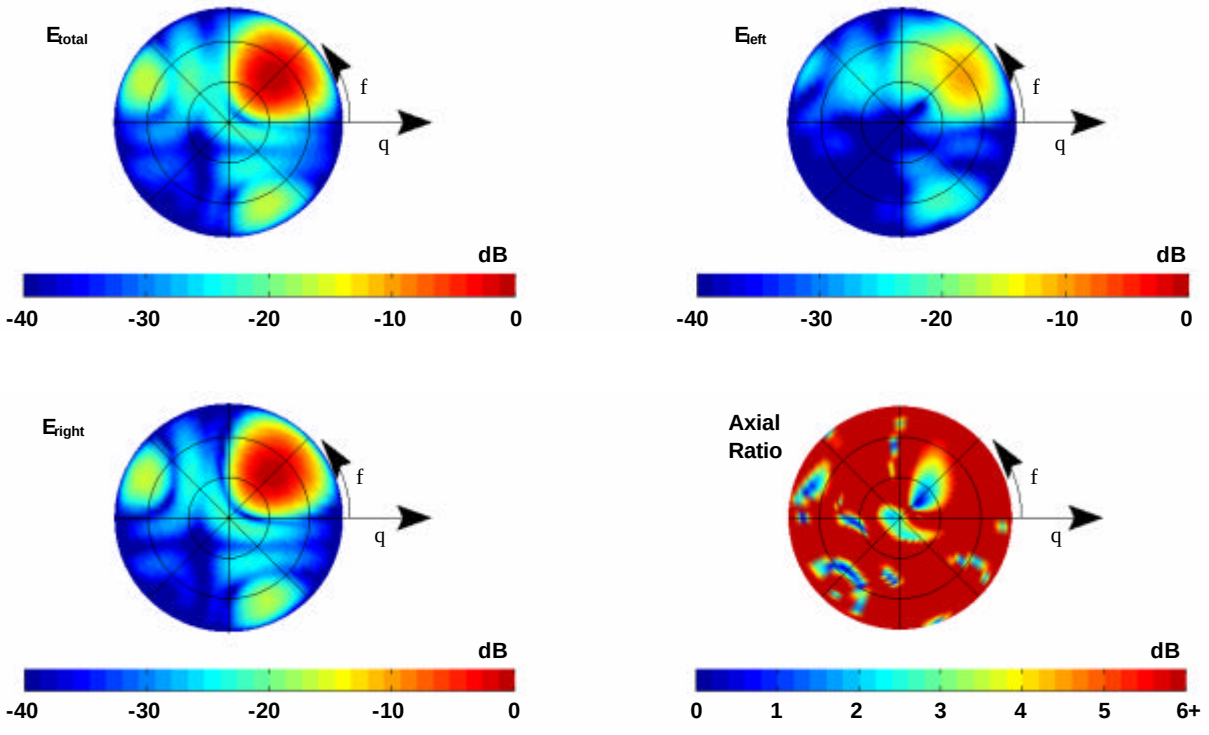

Fig. 3.11. Radiation characteristics obtained with SEQAR considering mutual coupling with beam steered to $\phi = 45°$ and $\theta = 45°$ at 1.57 GHz and SLL suppression of 20 dB. θ varies from 0° to 90° from the center out.

From this analysis it was observed as a major effect that the polarization purity degrades when including mutual coupling effects. In addition, the side lobe levels increase in the case considering mutual coupling. The directivity, however, has not been strongly affected.

It has been shown that mutual coupling is an important factor that should be taken into account when analyzing and designing circularly polarized arrays. One possible way to compensate its effects is suggested in [9], where the array elements have been re-optimized when placed in the array configuration. Another solution would be the use of an additional sequential rotation, as proposed in [10]. In this project however, only the techniques described in [8] are used

3.1.4 Beamsteering limit analysis

According to the array specifications given in Table 3.1, it is desirable to steer the main beam down to elevation angles of 30° or lower. However, as mentioned before, there are some physical limitations that need to be taken into account. In chapter 2 it was shown that the total field of an array is the product of the single element pattern and the array factor:

$$E_{total} = E_{SE} \cdot AF \tag{3.7}$$

It was also shown that the array factor changes for different beamsteering cases; however the single element pattern remains unchanged. Therefore, the aim of the beamsteering limit analysis was to find out how far from broadside the main beam can be steered while keeping the maximum directivity in the desired direction.

A number of simulations with SEQAR for different beamforming situations including mutual coupling effects have been performed. The decoupling algorithm included in SEQAR was applied to try to palliate these effects.

3.1.4.1 Beamsteering limits of the Galileo Antenna Array

Simulations of the Galileo Antenna Array for frequencies located at the lower and upper parts of the band have been performed to find the beamsteering limits. The purpose is to observe the different radiation pattern effects on the extreme frequency cases. The first observable effects when working with a broad band is that the directivity, as well as the side lobe level vary noticeably from the lower to the upper frequencies. For instance, when pointing the main beam to broadside and without applying any SLL suppression, a directivity of 15.65 dBi is observed at 1.19 GHz in contrast with 17.98 dBi at 1.57 GHz. The main reason for this is the electrical inter-element spacing, which is 0.38 λ_0 for the first and 0.5 λ_0 for the second frequency respectively. Moreover, the simulated gain at broadside for an isolated element decreases from the upper to the lower part of the frequency band.

Simulations pointing the main beam to an azimuth angle of 45° and different elevation angles with SLL suppression of 20 dB were performed. With this setup, the main beam could only be steered down to an elevation angle of 47.5° at 1.19 GHz. Further than this limit, the maximum directivity is not on the desired direction and side lobes with high levels appear. The calculated directivity in this case was 14.09 dBi. All side lobe levels are 20 dB under the main beam, as shown in Fig. 3.12. Under these conditions, the directivity at an elevation of 30° is estimated to be 12.12 dBi. At 1.57 GHz, the main beam could be steered down to an elevation angle of 40° considering the same SLL suppression and azimuth angle as in the former case. A directivity of 15.99 dBi is observed; however, two side lobes appear with levels greater than -20 dB, as it can be seen in Fig. 3.13. These lobes are caused by a larger inter-element spacing at this frequency.

The axial ratio for the 1.19 GHz case is reasonably good, below 5 dB, for elevation angles down to 20°. For the 1.57 GHz case this limit is around 35°. This effect could also be explained by the larger inter-element spacing.

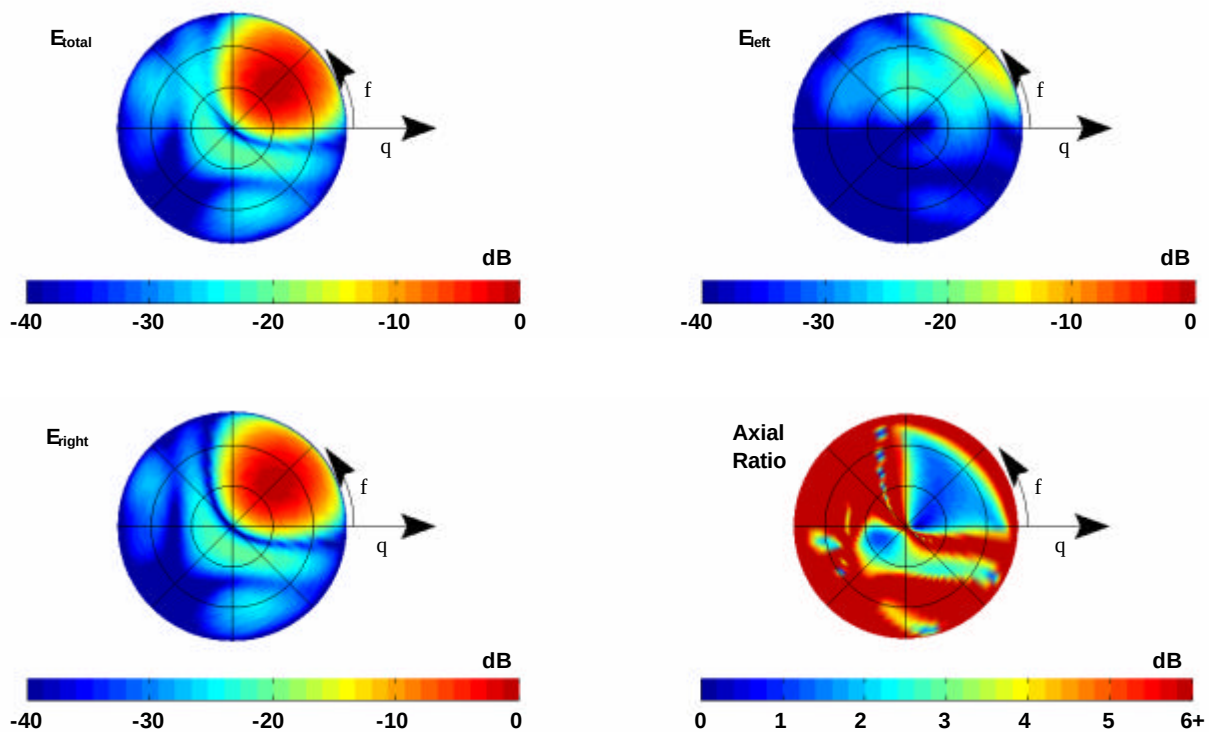

Fig. 3.12. Radiation characteristics obtained with SEQAR considering mutual coupling with beam steered to $\phi = 45°$ and $\theta = 45°$ at 1.19 GHz and SLL suppression of 20 dB. θ varies from 0° to 90° from the center out.

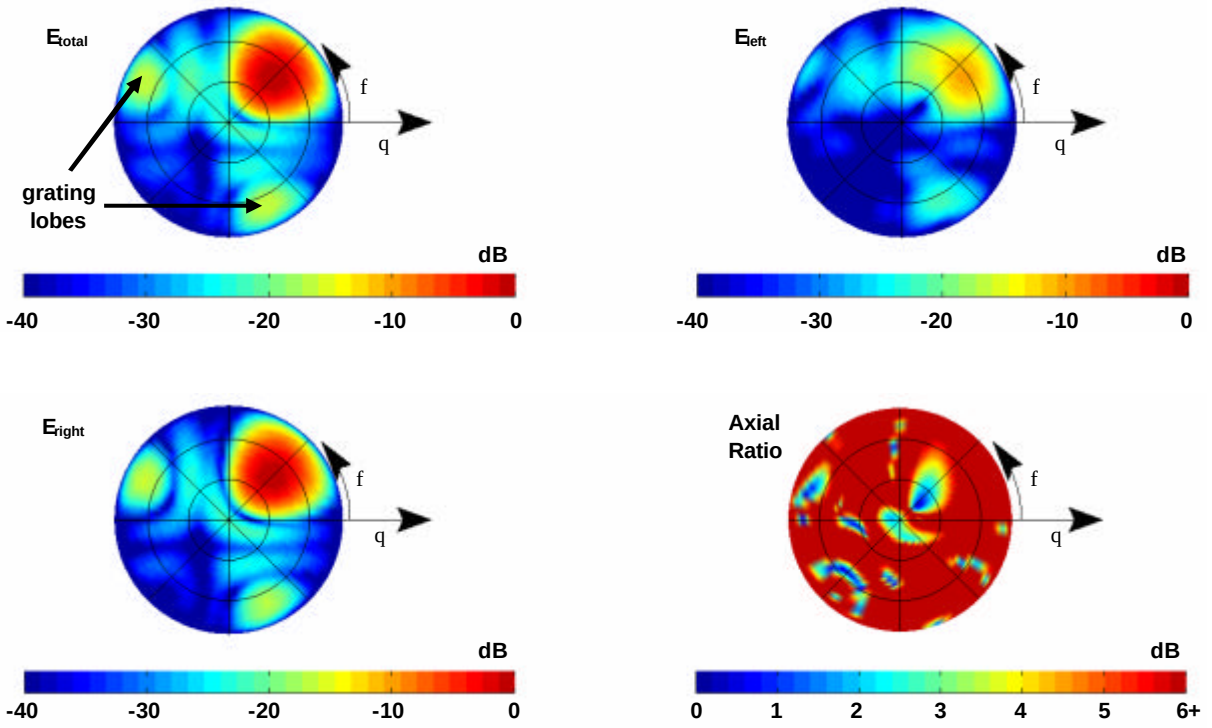

Fig. 3.13. Radiation characteristics obtained with SEQAR considering mutual coupling with beam steered to $\phi = 45°$ and $\theta = 45°$ at 1.57 GHz and SLL suppression of 20 dB. θ varies from 0° to 90° from the center out.

The results for the beamforming simulations presented show that the radiation characteristics, especially in terms of directivity and grating lobes excitation, may present significant variations within a broad frequency band demanding a careful design of the passive beamforming networks.

The knowledge gained from the mutual coupling and beamsteering limit analyses is used to select the beamforming cases to be implemented and tested.

3.2 Beamforming Analysis

It was shown in the previous sections that there are several effects have an important influence on the antenna array performance. In modern beamforming systems these effects are normally compensated by implementing complex beamforming algorithms such as MUSIC, ESPIRIT or Least Mean Squares on a Digital Signal Processor (DSP) [2]. Implementing such algorithms requires a good knowledge of the antenna array characteristics such as the one gained by the analyses presented. With this information in hand it is possible to decide which beamforming cases are to be implemented with the power dividers. In this section, the selected directions of arrival to be tested are presented and the radiation characteristics for each case are analyzed using two different tools.

3.2.1 Directions of Arrival to be tested

Several directions of arrival (DOA) were defined in order to test the beamsteering capabilities of the Galileo Antenna Array. A total of 6 DOAs, 2 for each frequency, are tested and were chosen in order to cover a wide range of possibilities. In the case of elevation, one of the cases is near to broadside and one close to the beamsteering limit previously calculated. The latter was achieved by giving a θ=70° input to SEQAR. Azimuth angles were chosen so they would cover different regions of space. The obtained DOAs can be seen in Table 3.2. The decoupling functions along with the SMI and Chebyshev side lobe level set to -20 dB were used.

Table 3.2. Directions of arrival to be tested.

Frequency	1.19 GHz	1.27 GHz	1.57 GHz
Close to broadside	θ=20° ϕ=120°	θ=20° ϕ=45°	θ=20° ϕ=290°
Beamsteering limit	θ=44° ϕ=120°	θ=44° ϕ=45°	θ=48° ϕ=290°

3.2.2 Optimal coefficient tables and radiation patterns using SEQAR and Designer

The in-house developed software SEQAR has been used to obtain optimal excitation coefficients for each of the beamforming cases to be tested. This software employs a Chebyshev tapering for side lobe level reduction [11]. The beamsteering and nulling uses the Sample Matrix Inversion (SMI) algorithm, which employs the signal vector and the interfering signal covariance matrix to calculate the optimal amplitudes and phases to be applied to the array elements [12].

The results for the ideal excitation amplitudes and phases obtained from SEQAR for the cases in Table 3.2 are presented in this section in form of tables and radiation patterns. The array element numbering in tables is the same as given in Fig. 3.9. Simulations using the optimal coefficients on the simplified Galileo Antenna Array model were performed and the results are compared with those of SEQAR.

Tables 3.3 to 3.8 show the optimal amplitudes and angles for each case in a matrix fashion, where the rows and columns increase from left-to-right and top-to-bottom respectively.

Case A: q=20° f=120° @ 1.19 GHz, SLL = -20 dB

In this case a very good performance in terms of side lobe level suppression for all azimuth angles was observed. The LHCP component remains at least 25 dB under the RHCP component. The maximum of the main beam is pointed at θ = 20° as expected. An excellent agreement between the results from SEQAR and those from Ansoft Designer using the simplified array model are observed in Fig. 3.14 to 3.16.

Table 3.3. Optimal excitation coefficients for the θ=20° ϕ=120° @ 1.19 GHz case.

Patch	1	2	3	4
Amplitude (1-4) **Phase (°)**	0.26 5.88	0.66 33.89	0.65 58.87	0.3 83.29
Amplitude (5-8) **Phase (°)**	0.64 -40.40	0.95 -4.47	0.76 28.59	0.71 37.24
Amplitude (9-12) **Phase (°)**	0.62 -86.22	1 -68.62	0.99 -24.5	0.65 -7.05
Amplitude (13-16) **Phase (°)**	0.23 -130.01	0.59 -110.21	0.67 -84.44	0.26 -53.23

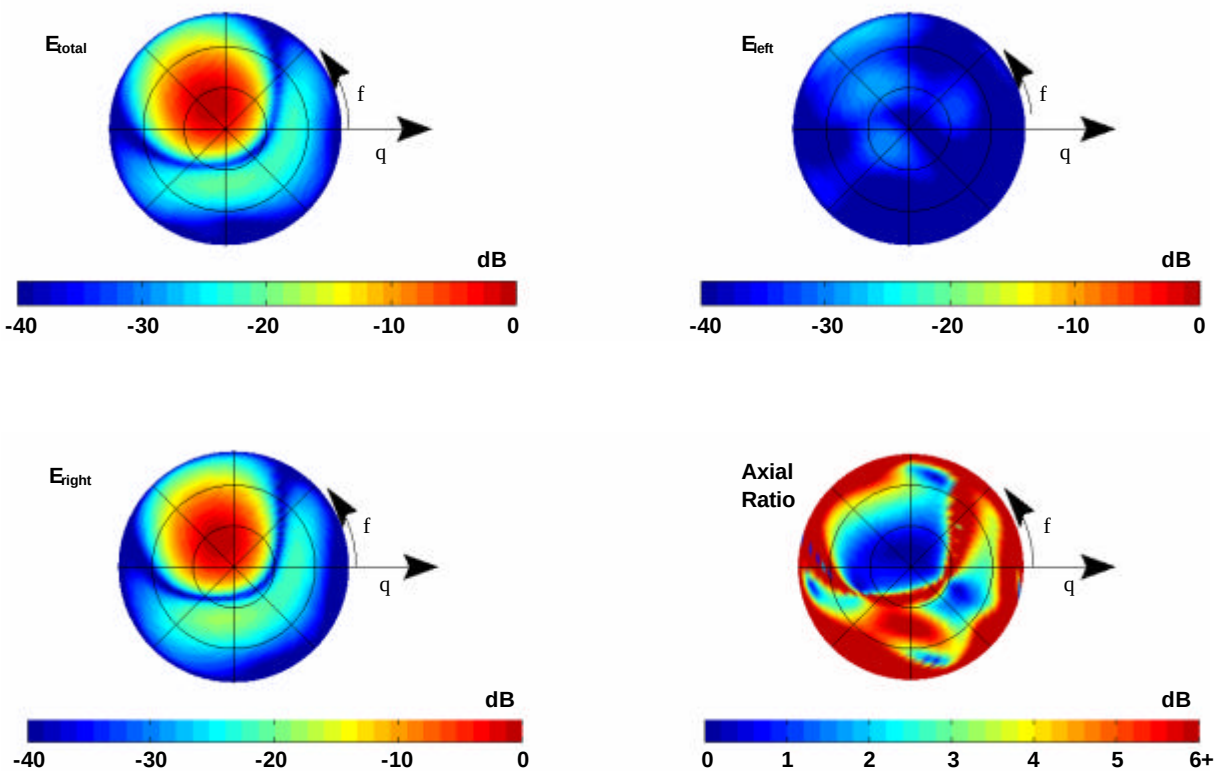

Fig. 3.14. Radiation characteristics obtained with SEQAR for the θ=20° ϕ=120° @ 1.19 GHz case.

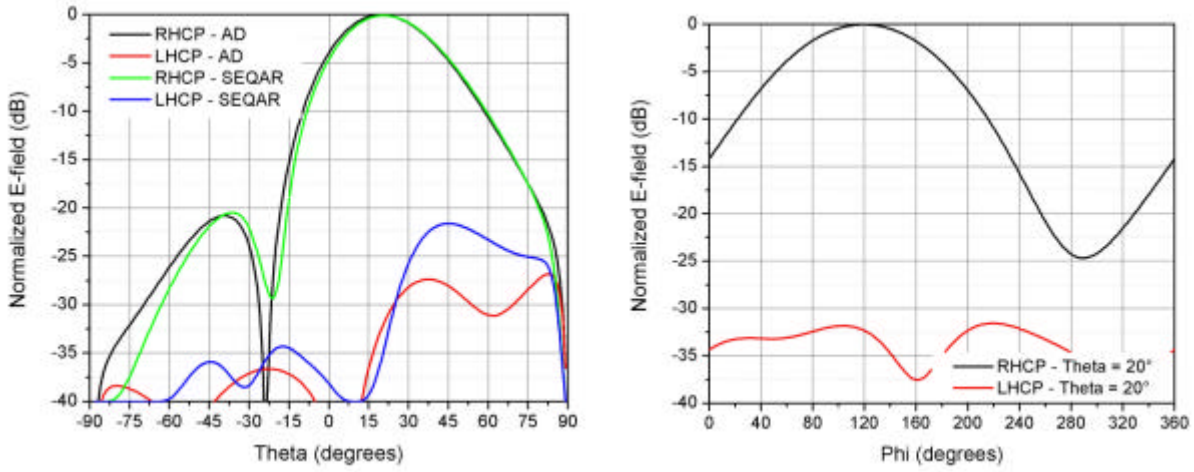

(a) (b)

Fig. 3.15. Comparison between the radiation characteristics obtained with SEQAR and those obtained with the simplified array model on Designer for the θ=20° ϕ=120° @ 1.19 GHz case. ϕ = 120° (a) and (b) θ = 20° cuts.

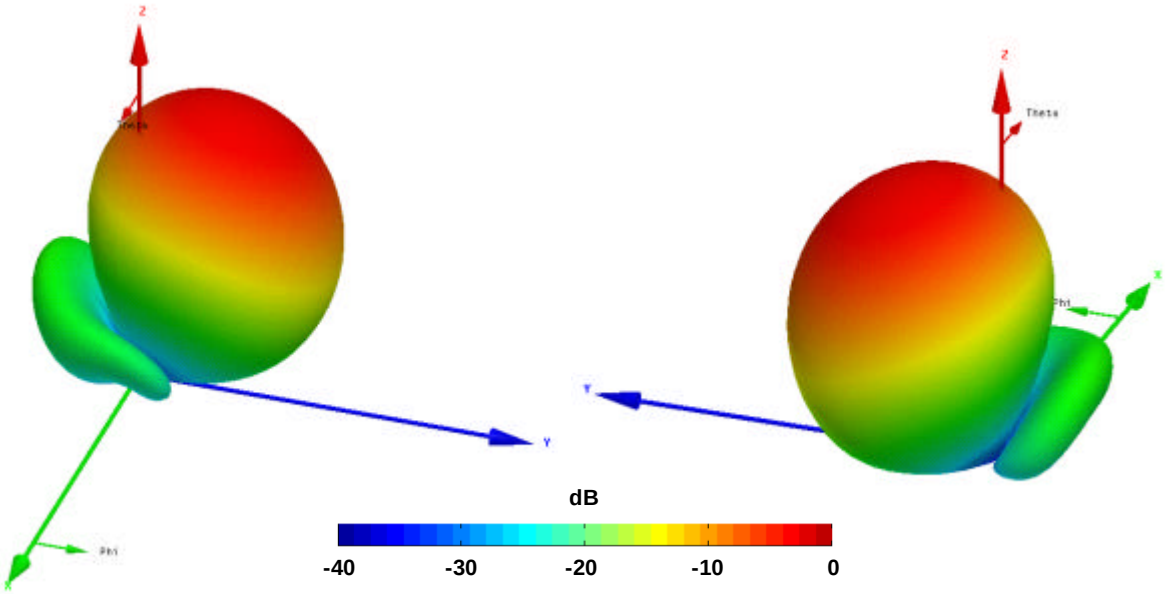

Fig. 3.16. 3D view of the normalized radiation pattern for the θ=20° ϕ=120° @ 1.19 GHz case in two different perspectives.

Case B: q=20° f=45° @ 1.27 GHz, SLL = -20 dB

The results in this case are very similar to those of the preceding one. The maximum of the main beam is pointed at θ = 20° as expected. Side lobe level suppression is greater than 20 dB for all azimuth angles. A slight increase of the cross-polarization component is observed, however it remains at least 23 dB under the co-polarization component as seen in Fig. 3.17 to 3.19.

Table 3.4. Optimal excitation coefficients for the θ=20° ϕ=45° @ 1.27 GHz case.

Patch	1	2	3	4
Amplitude (1-4)	0.31	0.84	0.75	0.3
Phase (°)	0.47	-37.9	-80.37	-119.71
Amplitude (5-8)	0.73	0.77	0.88	0.75
Phase (°)	-44.85	-89.97	-119.57	-172.1
Amplitude (9-12)	0.65	0.84	1	0.56
Phase (°)	-80.75	-96.61	-159.19	158.87
Amplitude (13-16)	0.34	0.91	0.81	0.3
Phase (°)	-119.9	-164.12	150.79	117.5

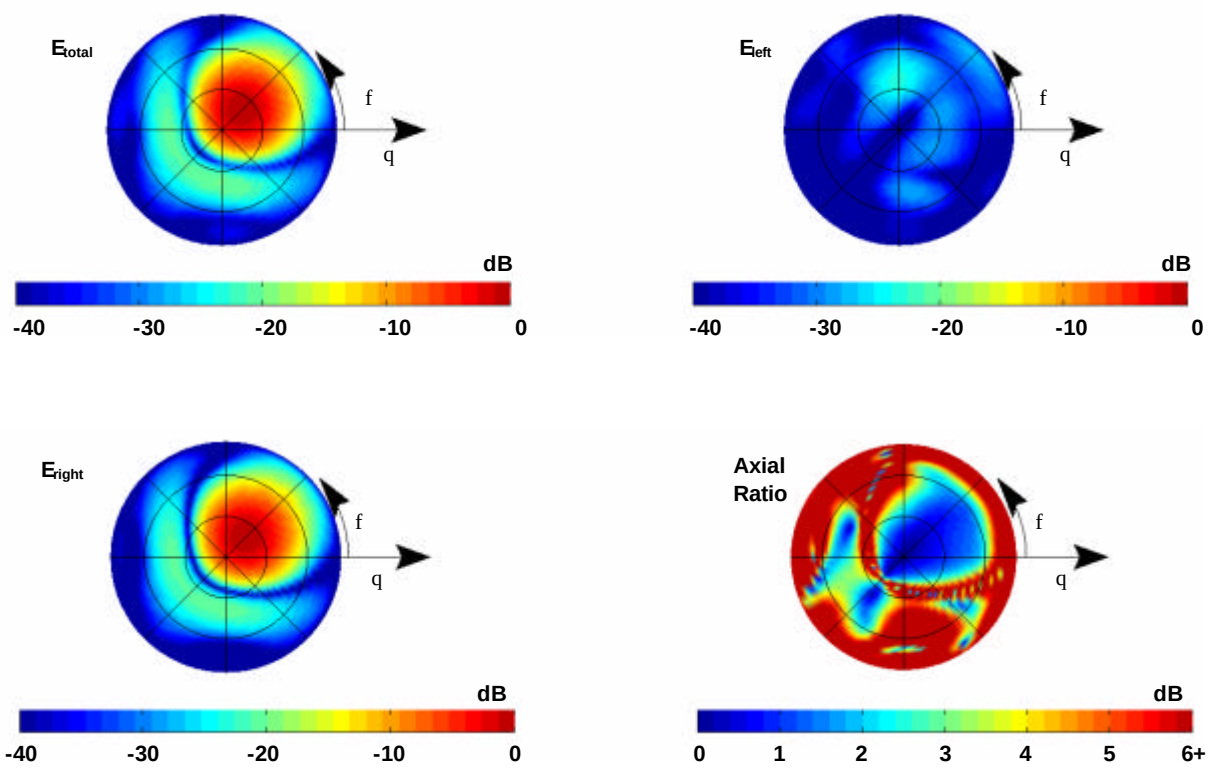

Fig. 3.17. Radiation characteristics obtained with SEQAR for the θ=20° ϕ=45° @ 1.27 GHz case.

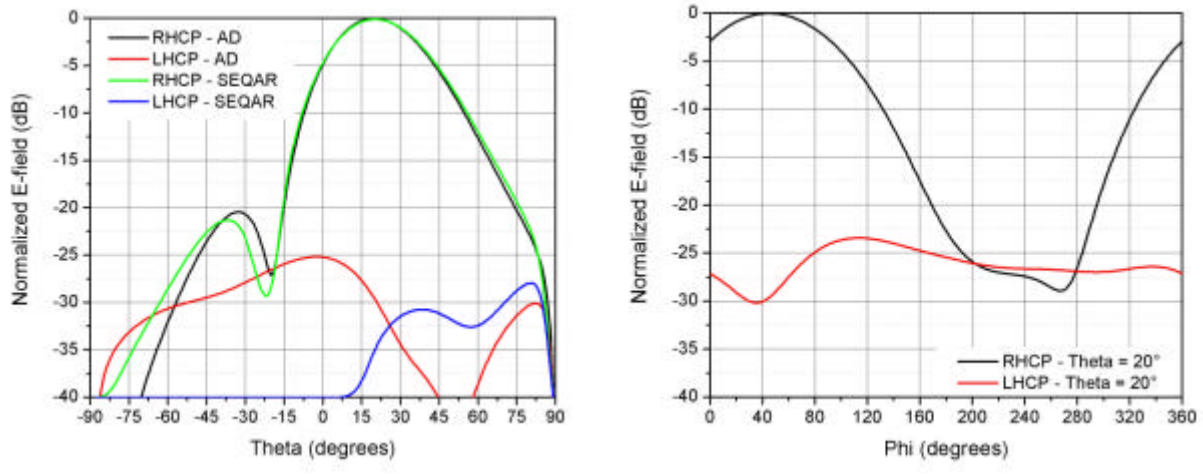

Fig. 3.18. Comparison between the radiation characteristics obtained with SEQAR and those obtained with the simplified array model on Designer for the θ=20° ϕ=45° @ 1.27 GHz case. ϕ = 45° (a) and (b) θ = 20° cuts.

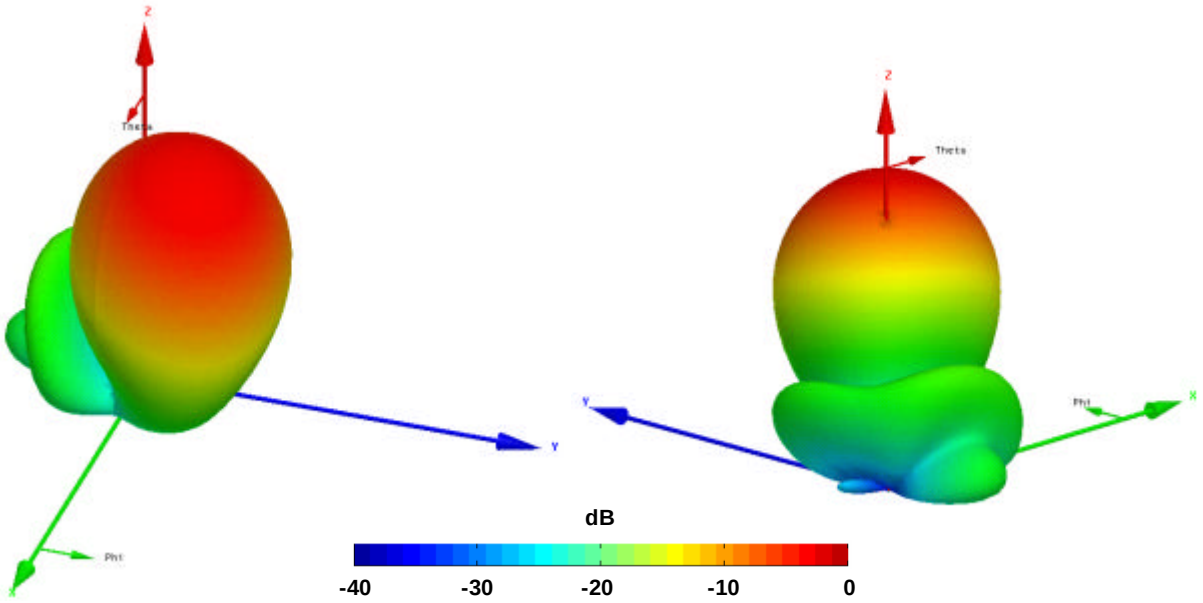

Fig. 3.19. 3D view of the normalized radiation pattern for the θ=20° ϕ=45° @ 1.27 GHz case in two different perspectives.

Case C: q=20° f=290° @ 1.57 GHz, SLL = -20 dB

The simulation results for this case show once more a good performance in terms of beampointing accuracy. In contrast, side lobe levels reach values as high as -15dB in relation to the main beam. Besides, the cross-polarization level is higher than expected, reaching values of -15dB for some angles. The effects in side lode level and cross-polarization are due to a larger inter-element distance ($0.5\lambda_0$ in this case). The overall performance is still relatively good nevertheless as the side lobes are uniformly suppressed creating a symmetrical radiation pattern as seen in Fig. 3.20 to 3.22.

Table 3.5. Optimal excitation coefficients for the θ=20° ϕ=290° @ 1.57 GHz case.

Patch	1	2	3	4
Amplitude (1-4) **Phase (°)**	0.20 69.78	0.65 37.92	0.54 19.51	0.19 6.21
Amplitude (5-8) **Phase (°)**	0.64 139.81	1 123.38	0.82 89.0	0.63 71.13
Amplitude (9-12) **Phase (°)**	0.72 -152.35	0.8 -152.16	0.9 164.39	0.58 139.54
Amplitude (13-16) **Phase (°)**	0.29 -81.01	0.56 -99.68	0.67 -125.41	0.22 -154.31

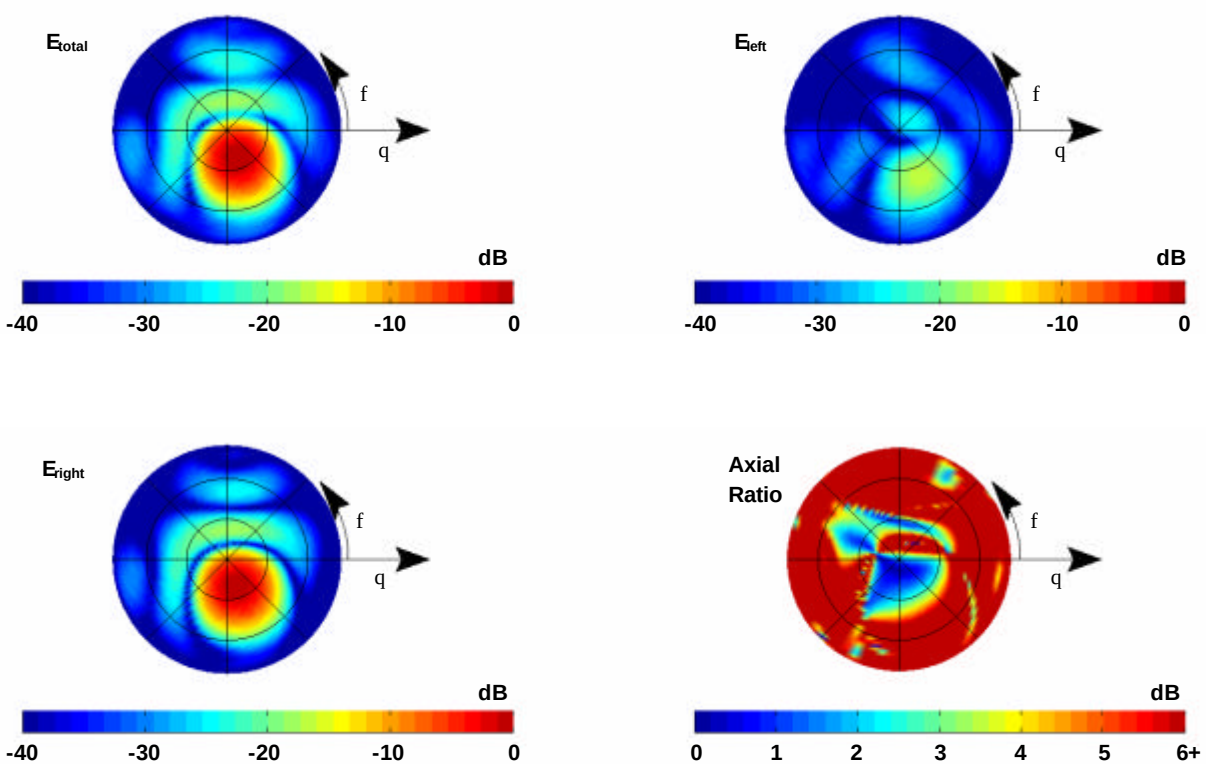

Fig. 3.20. Radiation characteristics obtained with SEQAR for the θ=20° ϕ=290° @ 1.57 GHz case.

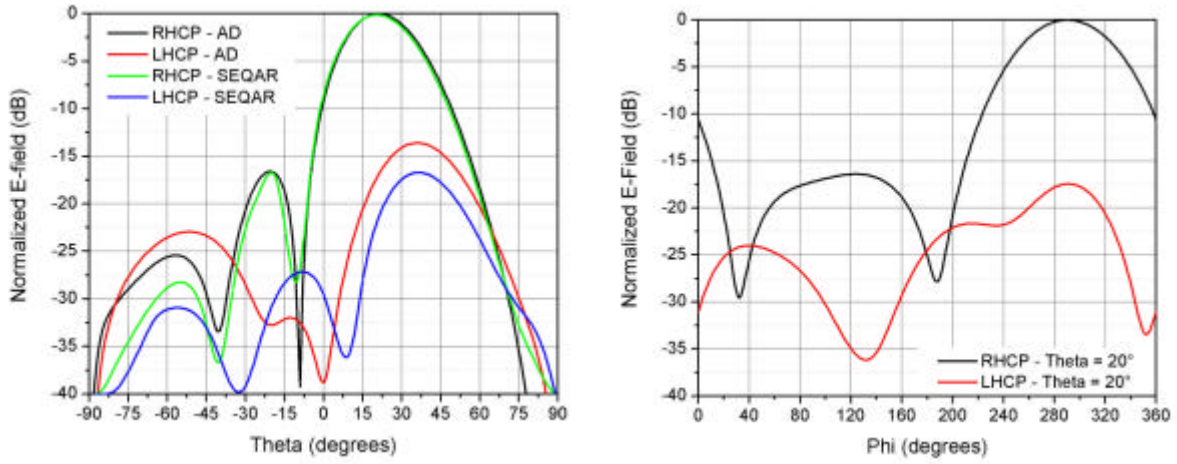

(a) (b)

Fig. 3.21. Comparison between the radiation characteristics obtained with SEQAR and those obtained with the simplified array model on Designer for the θ=20° ϕ=290° @ 1.57 GHz case. ϕ = 290° (a) and (b) θ = 20° cuts.

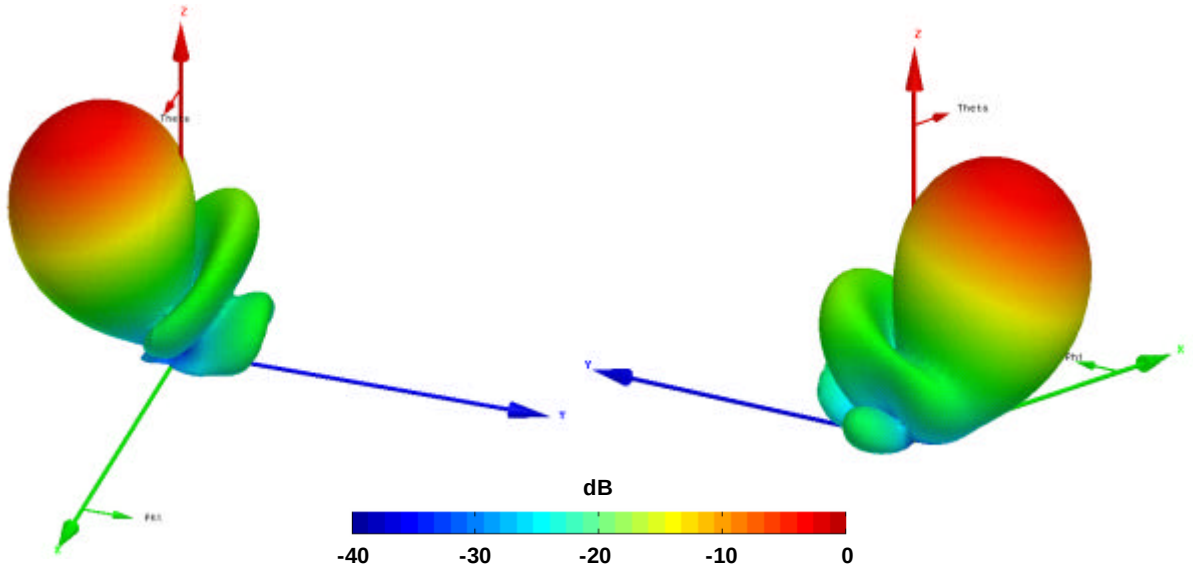

Fig. 3.22. 3D view of the normalized radiation pattern for the θ=20° ϕ=290° @ 1.57 GHz case in two different perspectives.

Case D: q=44° f=120° @ 1.19 GHz, SLL = -20 dB

Some the effects regarding the beamforming limitations discussed earlier can be observed through this case. A strong angular shift in the maximum of the main beam is observed as it is directed towards θ = 44° instead of the 70° given as an input for SEQAR. The gain level at θ = 70° is 3.67 dB lower than that on the direction of the maximum. This can be explained by the pattern multiplication property of antenna arrays where the single element pattern is constant regardless of the angle the main beam is steered to. Besides, it can be observed that the beamwidth is considerably bigger. The test shows a reasonably good performance in side lobe level suppression as they remain under -16 dB for all azimuth angles. The cross-polarization level remains reasonably low (<-18dB) for almost all angles as it can be observed in Fig. 3.23 to 3.25.

Table 3.6. Optimal excitation coefficients for the θ=44° ϕ=120° @ 1.19 GHz case.

Patch	1	2	3	4
Amplitude (1-4)	0.21	0.51	0.4	0.21
Phase (°)	7.82	77.96	126.02	170.26
Amplitude (5-8)	0.61	0.9	0.55	0.57
Phase (°)	-104.69	-25.15	45.23	76.93
Amplitude (9-12)	0.57	1	0.8	0.58
Phase (°)	147.77	-145.85	-65.07	-24.44
Amplitude (13-16)	0.18	0.5	0.51	0.19
Phase (°)	51.1	104.93	168.85	-135.22

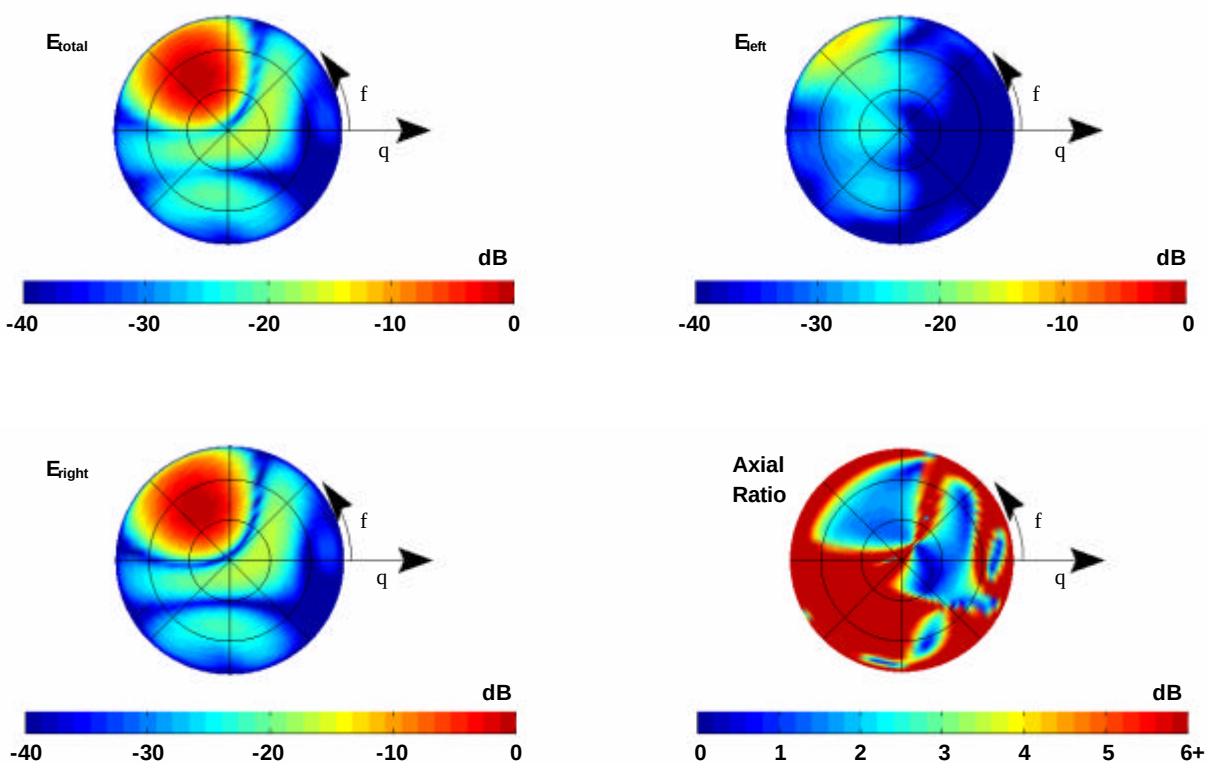

Fig. 3.23. Radiation characteristics obtained with SEQAR for the θ=44° ϕ=120° @ 1.19 GHz case.

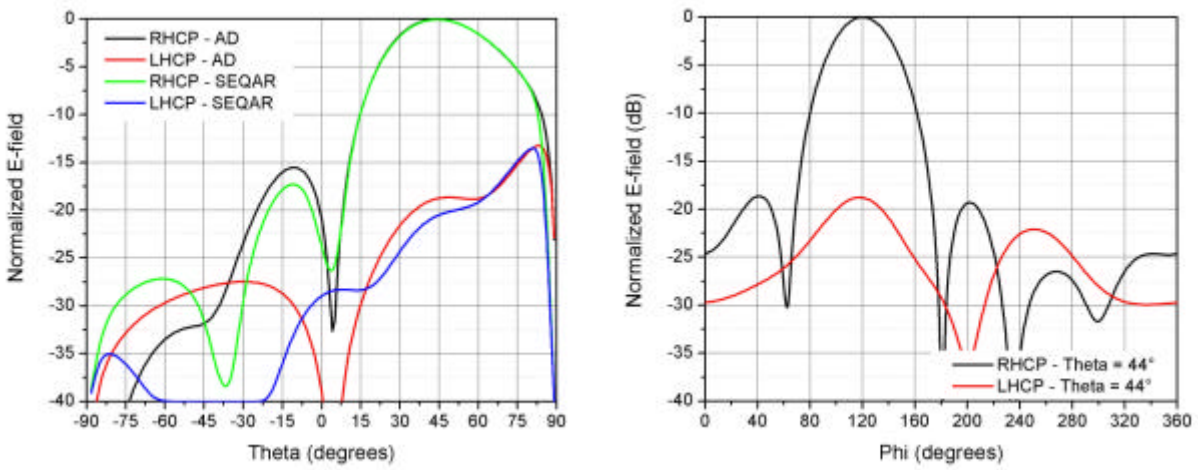

(a) (b)

Fig. 3.24. Comparison between the radiation characteristics obtained with SEQAR and those obtained with the simplified array model on Designer for the θ=44° ϕ=120° @ 1.19 GHz case. ϕ = 120° (a) and (b) θ = 44° cuts.

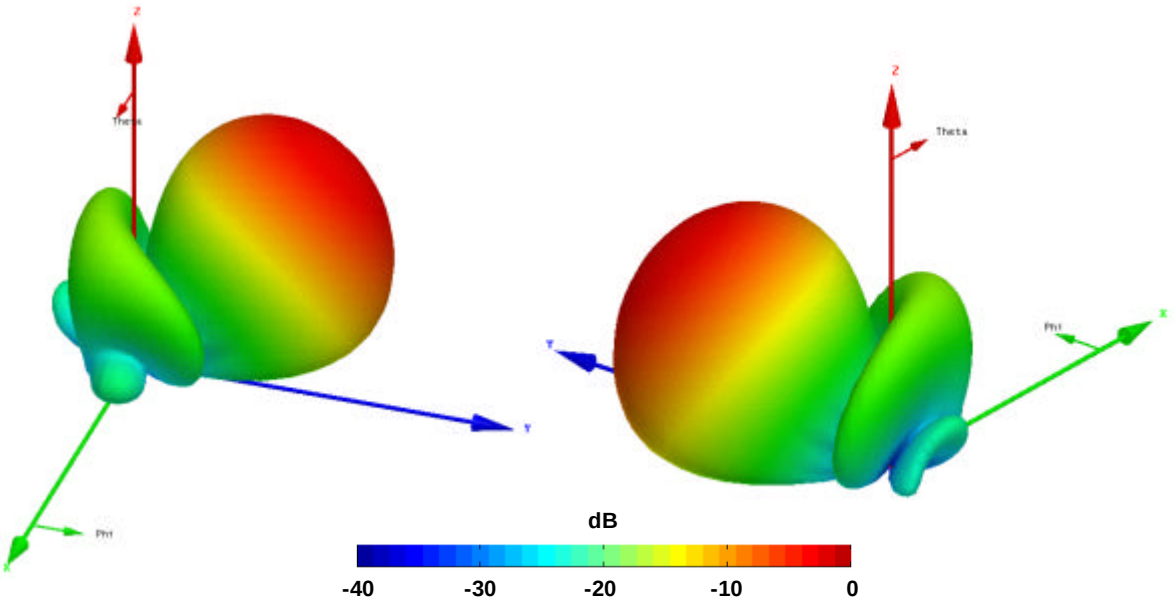

Fig. 3.25. 3D view of the normalized radiation pattern for the θ=44° ϕ=120° @ 1.19 GHz case in two different perspectives.

Case E: q=44° f=45° @ 1.27 GHz, SLL = -20 dB

This test shows also a strong angular shift as the maximum radiation is directed towards the θ = 44° angle instead of the 70° given as input for SEQAR. The power level at θ = 70° is 4 dB smaller than that on the direction of maximum radiation. The radiation patterns on Fig. 3.26 to 3.28 show that side lobe levels are kept under -16dB for all azimuth angles, which can be considered relatively good. The cross-polarization performance is good as it only goes above -20dB for a very small region on space as it can be observed in Fig. 3.26 and 3.27.

Table 3.7. Optimal excitation coefficients for the θ=44° ϕ=45° @ 1.27 GHz case.

Patch	1	2	3	4
Amplitude (1-4) **Phase (°)**	0.22 -27.95	0.61 -96.2	0.74 177.65	0.27 69.73
Amplitude (5-8) **Phase (°)**	0.51 -100.22	0.69 -174.44	1 84.04	0.61 -25.73
Amplitude (9-12) **Phase (°)**	0.51 -171.42	0.92 109.24	1 -3.45	0.49 -108.14
Amplitude (13-16) **Phase (°)**	0.28 89.87	0.9 -9.91	0.86 -110.25	0.21 166.43

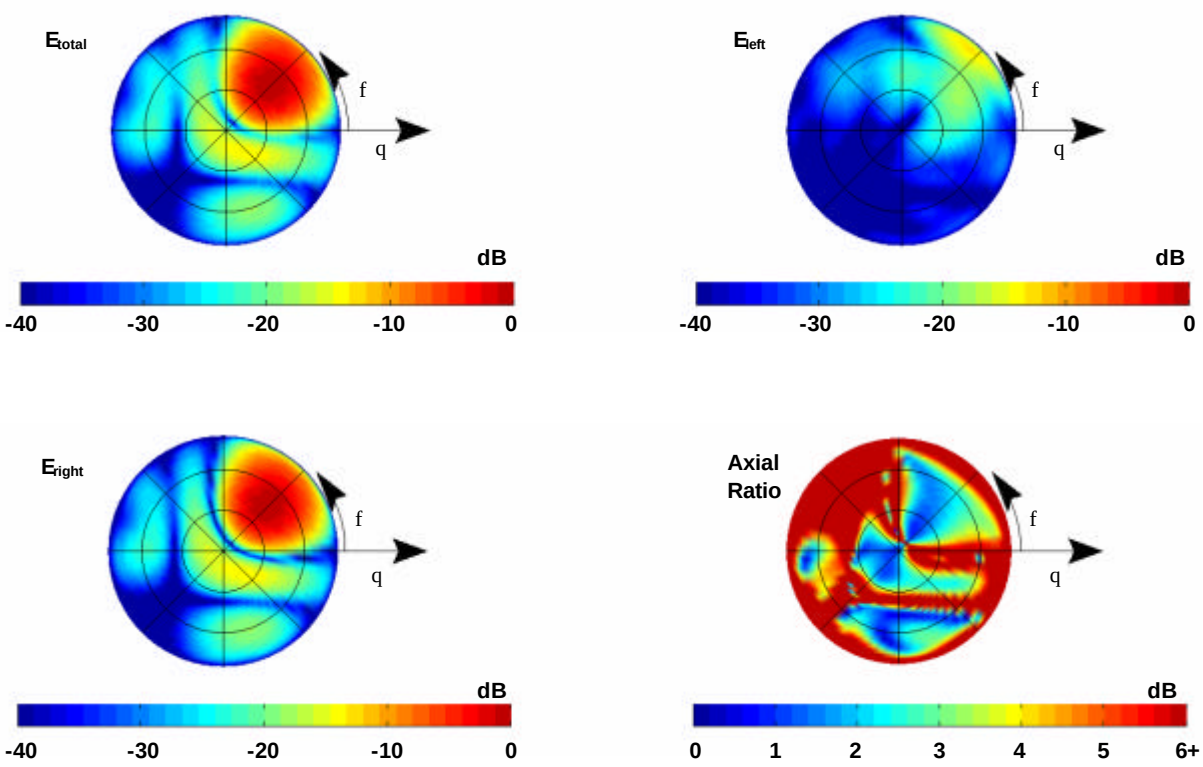

Fig. 3.26. Radiation characteristics obtained with SEQAR for the θ=44° ϕ=45° @ 1.27 GHz case.

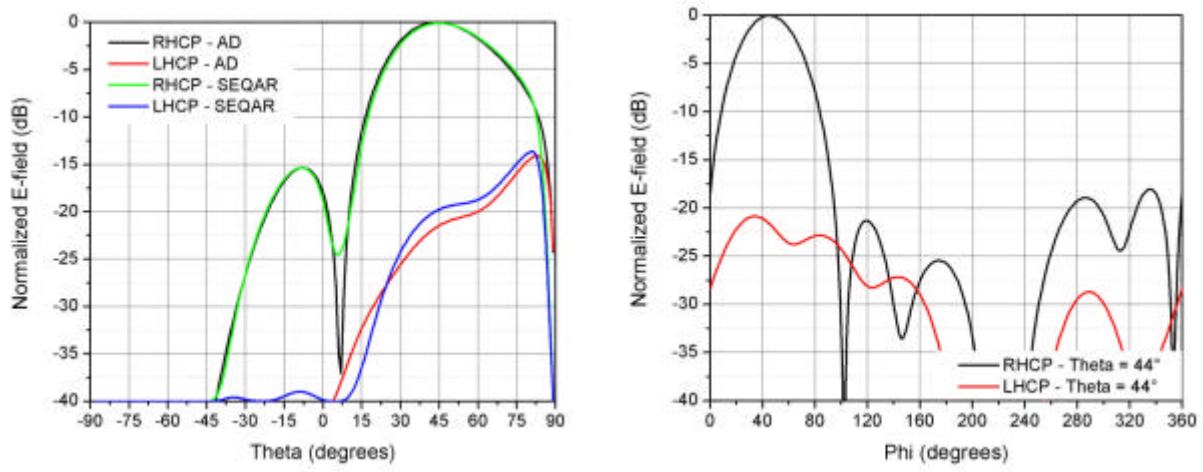

(a) (b)

Fig. 3.27. Comparison between the radiation characteristics obtained with SEQAR and those obtained with the simplified array model on Designer for the θ=44° ϕ=45° @ 1.27 GHz case. ϕ = 45° (a) and (b) θ = 44° cuts.

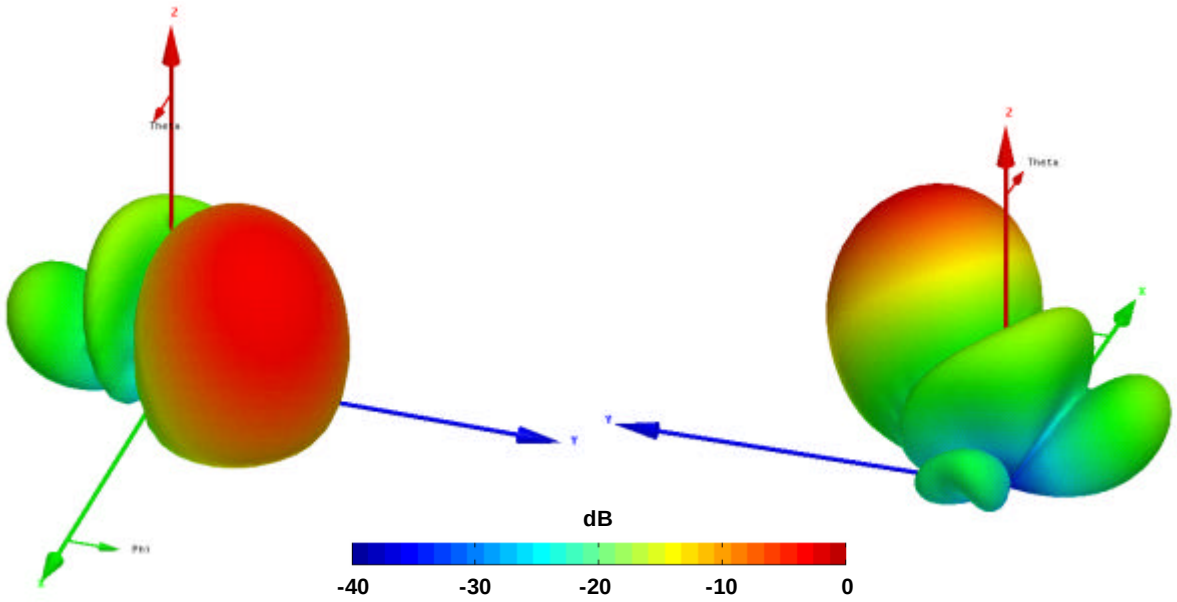

Fig. 3.28. 3D view of the normalized radiation pattern for the θ=44° ϕ=45° @ 1.27 GHz case in two different perspectives.

Case F: q=48° f=290° @ 1.57 GHz, SLL = -20 dB

This test shows a smaller angular shift as the maximum radiation is directed towards θ = 48°, but the overall performance is severely degraded. The radiation pattern shows a clear grating lobe (~ 6 dB under the main lobe) on the ϕ = 70° direction and some side lobe levels are above -15dB. Cross-polarization is very poor, being the left-hand component only 5 dB below the right-hand one in some cases as seen in Fig. 3.29 to 3.31. These effects can be explained by a larger inter-element spacing and the frequency dependant characteristics of planar arrays.

Table 3.8. Optimal excitation coefficients for the θ=48° ϕ=290° @ 1.57 GHz case.

Patch	1	2	3	4
Amplitude (1-4) **Phase (°)**	0.3 54.96	0.74 11.05	0.61 -57.08	0.06 -61.0
Amplitude (5-8) **Phase (°)**	0.77 -139.05	1 178.76	0.93 105.98	0.37 60.4
Amplitude (9-12) **Phase (°)**	0.75 19.03	0.97 -19.04	0.95 -93.01	0.39 -144.55
Amplitude (13-16) **Phase (°)**	0.22 175.71	0.67 136.73	0.61 63.84	0.07 11.8

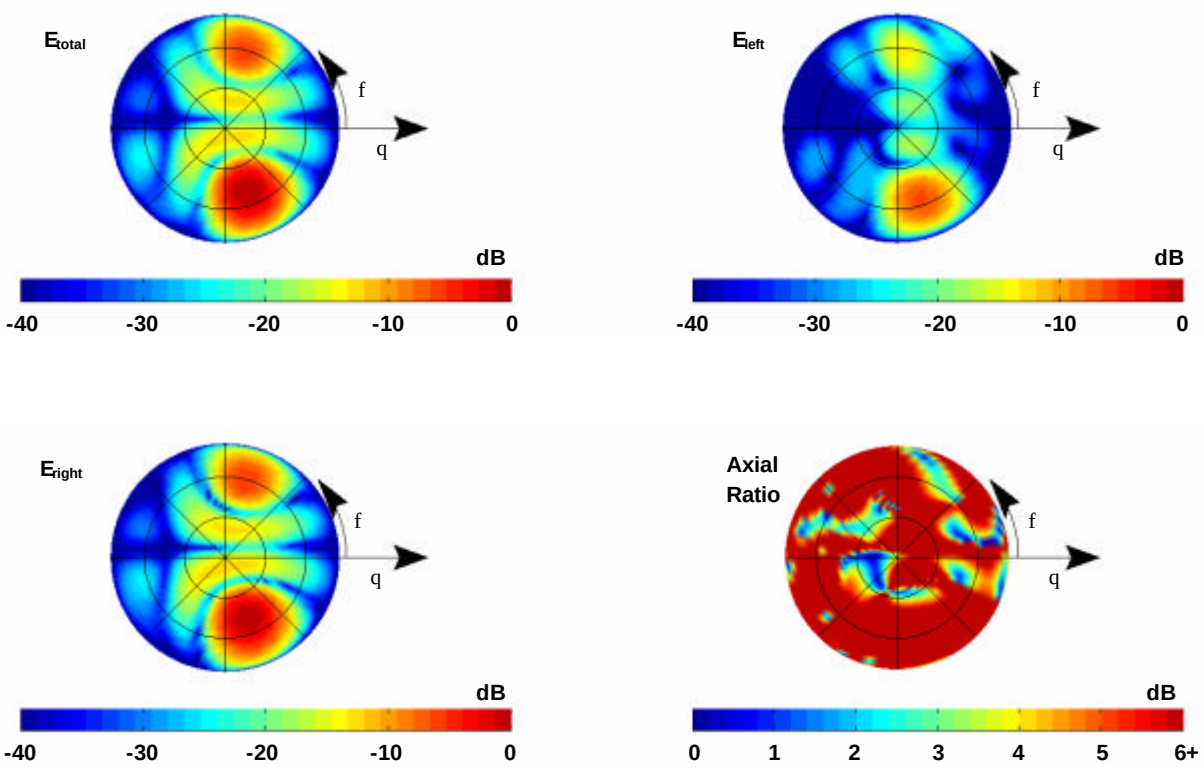

Fig. 3.29. Radiation characteristics obtained with SEQAR for the θ=48° ϕ=290° @ 1.57 GHz case.

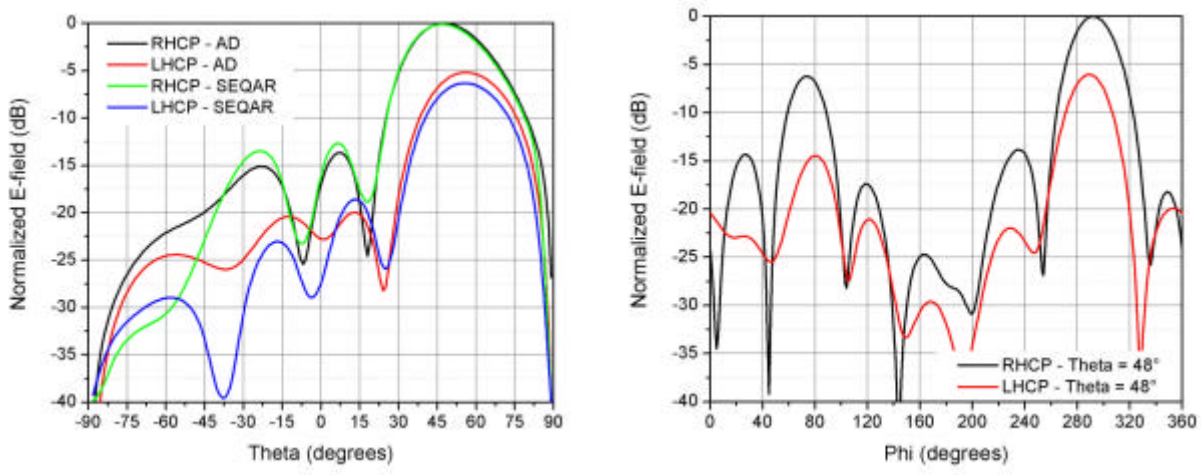

(a) (b)

Fig. 3.30. Comparison between the radiation characteristics obtained with SEQAR and those obtained with the simplified array model on Designer for the θ=48° ϕ=290° @ 1.57 GHz case. ϕ = 290° (a) and (b) θ = 48° cuts.

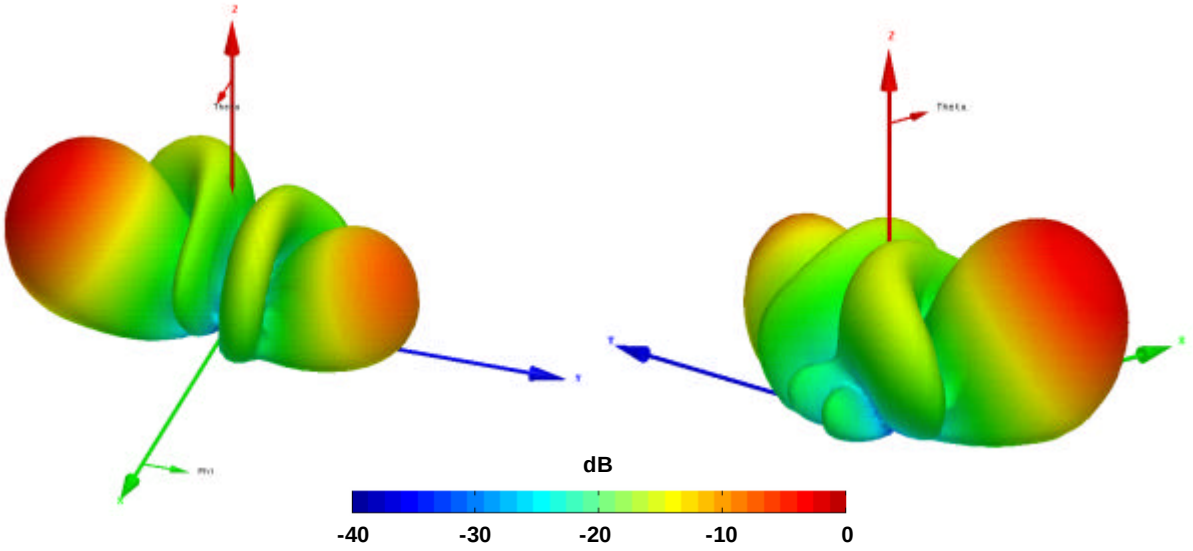

Fig. 3.31. 3D view of the normalized radiation pattern for the θ=48° ϕ=290° @ 1.57 GHz case in two different perspectives.

3.2.2.1 Remarks on the coefficients obtained and the tests with the simplified Galileo Array model

After a careful inspection of the optimal excitation coefficients it can be noticed that they do not follow any particular pattern neither in amplitude nor phase. This is the result of the use of beamforming and decoupling algorithms along with tapering. The uniform change in relative phases studied in the previous chapter is just a simplification of a more complex problem. This creates a challenging problem when designing the passive beamforming networks of this project. The way this problem is tackled is presented in the next chapter.

The series of simulations using the optimal excitation coefficients obtained with SEQAR on the simplified Galileo Antenna Array show the effects of frequency, mutual coupling, and beamsteering limits. In most cases the agreement between SEQAR and Designer is very good. There are some undesired effects especially in the highest frequency that show us that keeping a similar performance across a large band can be very difficult.

Chapter 4 - Design of the beamforming power divider networks

In chapter 3 the physical characteristics of the Galileo Antenna Array were presented and its performance in terms of mutual coupling and beamsteering limits analyzed. This knowledge led to the selection of the beamforming cases to be designed and the calculation of the optimal excitation coefficients for each antenna element using SEQAR. The development of the power divider networks to perform the passive beamforming tests is presented in this chapter.

Firstly, a brief introduction to three-port power dividers is presented. Then, the characteristics of the power divider networks, the design constraints, the way these are tackled, and an example divider are presented. The design and implementation of a MATLAB® program to accelerate the design of the power dividers and a sample output are presented afterwards. Finally, the models of the power divider designs in Ansoft Designer® and HFSS® and the simulation results obtained are presented and discussed.

4.1 Three-port power divider basics

Power dividers are used to split the input power on a transmission line into a number of smaller amounts of power to, e.g. excite the elements of an array antenna. Besides, they can be used as power combiners if the direction of operation is inverted.

An essential property of lossless reciprocal three-port junctions is that the three ports can not be matched at the same time. To divide the input power P_1 into fractions $\alpha P_1 = P_2$ and $(1-\alpha)P_1 = P_3$ at ports 2 and 3 and to have the input port 1 matched in a structure such the one showed in Fig. 4.1 we require that

$$\frac{Y_2}{Y_3} = \frac{a}{1-a} \tag{4.1}$$

and

$$Y_1 = Y_2 + Y_3 \tag{4.2}$$

where Y_2 and Y_3 are the admittances of ports 2 and 3.

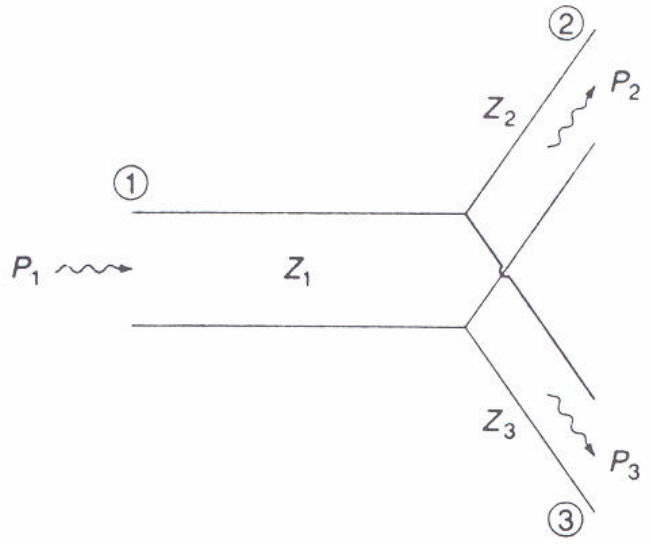

Fig. 4.1. A lossless three-port junction as a power divider.

Due to the fact that the impedances in output ports are different, these will not be matched unless additional impedance transformers are added on the ends. Besides, no isolation exists between output ports, therefore S_{23} will play a role in the operation of the divider unless it is properly matched. A popular alternative to overcome these disadvantages is the use of Wilkinson N-way power dividers [13].

The theory of power dividers has been studied extensively in the literature [14], [15], the reader can refer to it for a more thorough knowledge.

4.2 Characteristics of the desired power divider networks

The power divider networks should posses a number of characteristics to be able to provide the desired excitation coefficients to each of the antenna array elements. There are constraints in terms of precision, size, and shape that must be taken into account when designing the power dividers.

The power dividers must provide the desired excitation coefficients at the output ports with good precision in phase and particularly in amplitude. As it was proved in previous chapters, the phases provide the steering of the beam to the desired DOA; however it is not necessary that they match exactly the angles provided by SEQAR as the steering is dependant only on the relative phases among elements. This means that if the optimal phase given by SEQAR for a given element is, e.g. 85° and the one at the output of the divider is -120° it will have the same effect in the pointing of the main beam if the relative phases among elements is maintained. After doing several test simulations, it was observed that a deviation of a few degrees (<3°) from the ideal case does not affect the pointing considerably. In the case of the relative amplitudes it was found out that the design is more sensitive to changes in these. Relative amplitudes provide the beamforming and side lobe level reduction; therefore more attention has to be paid to achieve a good agreement between the ideal amplitudes and the obtained ones.

Two important constraints in the design are the size and the shape of the module containing the test beamforming networks. It can be seen on Fig. 4.2 that the power divider networks should fit into a rectangular box with dimensions 480mm x 100mm. A careful selection of the substrate material to be used as well as a good planning of the geometry of the structure must be performed before designing the dividers.

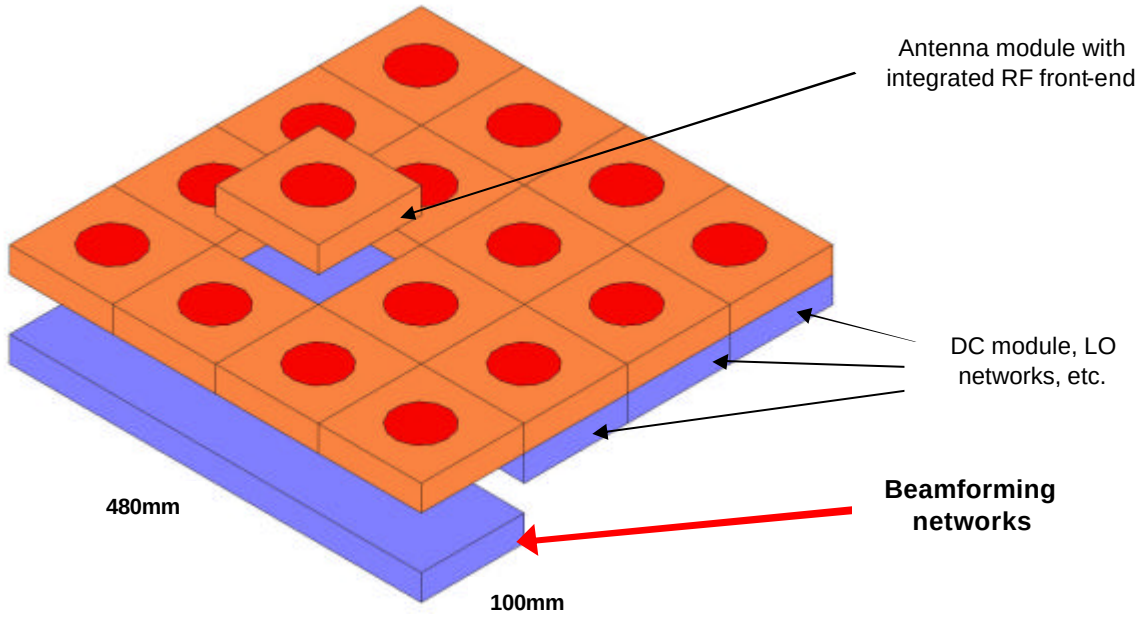

Fig.4.2. Simplified scheme of the 4 x 4 modular Galileo antenna array. Beamforming section highlighted.

4.3 Design and implementation of the beamforming divider networks

In order to fulfill the requirements presented in the previous section a careful design should be performed. In this section, the considerations that led to the chosen power divider geometry are discussed and an example divider presented.

4.3.1 Considerations regarding the power divider geometry

A list of the most important factors that need to be taken into account in the actual physical implementation of the divider networks and their solutions is presented below.

- **Non-alignment of divider output ports and antenna input ports.** The beamforming networks will be placed in a rectangular module on the lower part of the array as seen in Fig. 4.2. This means that the output ports will not be aligned with the input ports of the antenna elements. Phase-stable cables (i.e. with the exact same physical length, regardless of the port they are connected to) are used to guarantee that each antenna input port gets the same phase as the divider output. The aforementioned cables, whose measured characteristics are shown in Fig. 4.3, have a maximum deviation of half degree and induce a loss of approximately 0.4dB in the frequency range of the Galileo antenna array.

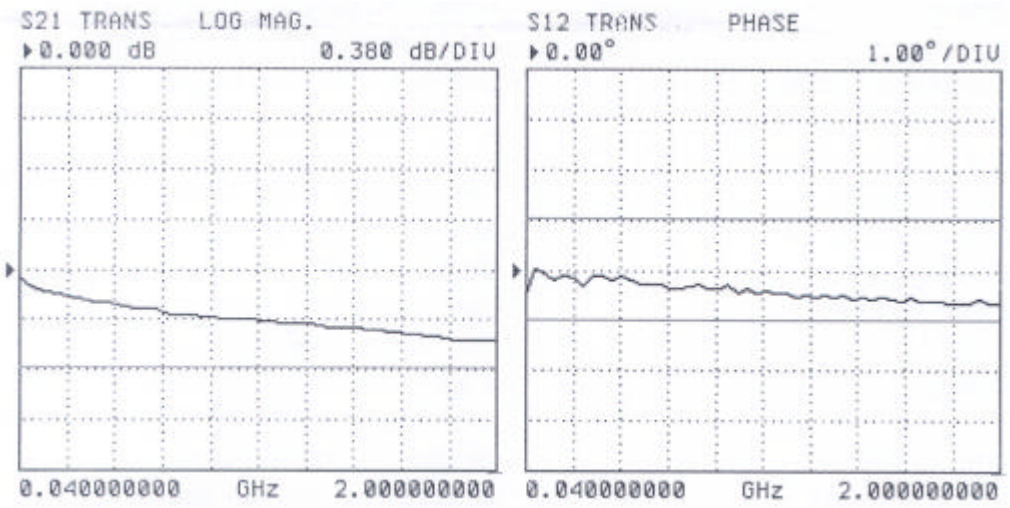

Fig. 4.3. Transmission loss and phase deviation characteristics of the phase-stable cables.

- **Space for different transmission line lengths in output ports.** There are beamsteering cases when the relative phases between output ports changes uniformly between lines and/or columns. In these cases, such as the one in Fig. 4.4, the shift of the phases can be gradually done for the corresponding lines or columns. This allows having a symmetrical structure where the output lines are aligned. In our case, if the phases of the optimal coefficients presented in the previous chapter are examined it can be observed that these are in a non-uniform and non-symmetrical distribution. Therefore, different transmission line lengths in the output ports in order to provide the corresponding phases must be used. This poses a problem as the difference between lengths of the lines can be considerably large if the material selected has a low dielectric constant.

- **Substrate material selection.** The choice of the substrate material to be used is very important. It is desirable to have a low dielectric constant (ε_r) material to avoid surface waves and losses. However, the costs of using such material are longer and wider transmission lines as compared with the use of a material with higher dielectric constant. As an example, a 50Ω line would be 1.99mm wide and 183.8mm/wavelenght long at 1.19 GHz for a material with ε_r=2.2 in contrast with 0.95mm and 120.1mm for a material with ε_r=6.15. The area available for the dividers is limited

(480mm x 100mm) so a compromise has to be made in order to be able to fit the structures in it, regardless of the frequency.

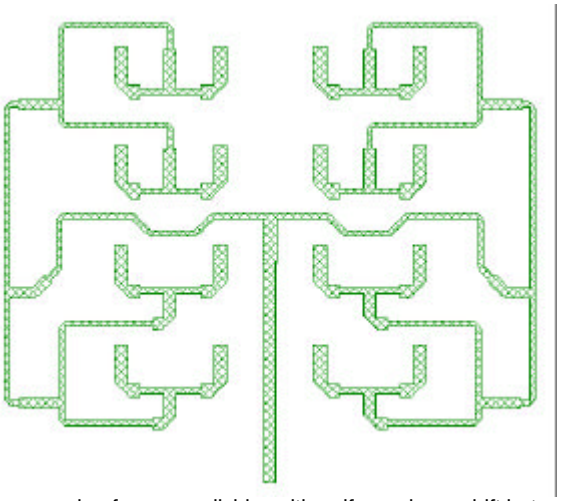

Fig. 4.4. An example of a power divider with uniform phase shift between lines.

- **Space for connectors and walls.** Each of the output ports will have a square SMA connector as the one in Fig. 4.5 whose external dimensions are 12.7mm x 12.7mm. Hence, the minimum distance between two contiguous output lines should be 13mm to avoid an overlap of the areas where the connectors will be placed. In the case they are close to the walls the minimum distance required is 6.5 mm. The structure will be enclosed in a box so the dividers, including connectors, can not extend up to 480mm in longitude or 100mm in width. The width of the box walls should also be taken into account, therefore the available area is reduced.

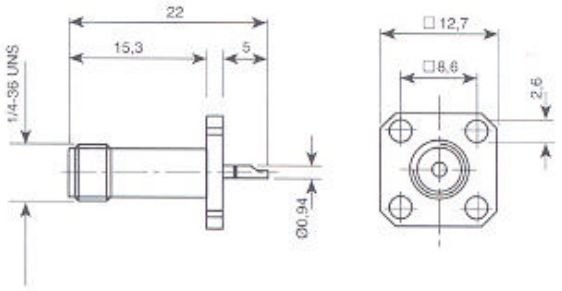

Fig. 4.5. SMA connector dimensions in mm.

The geometry designed to take into account the considerations presented is shown in Fig. 4.6. The structure consists of 8 output ports on each end. The chosen material was Rogers RT/duroid® 3006 with a dielectric constant of 6.15 and 0.64 mm thickness. This material assures that even in the worst-case scenario where there is a 360° phase difference between the output lines at the lowest frequency (i.e. longer transmission lines) the structure will fit within the given area. Besides, it allows designing dividers with low-impedance lines with moderate widths to keep the structure losses low.

A trade-off had to be made when selecting the separation between output lines, which is fixed at 10 mm. The width for all dividers including connectors, independent of the frequency, is fixed at 83mm. This gives an 8.5mm margin on both ends to account for the width of the box walls; however means there can not be two contiguous output lines whose length difference is less than 13mm in order to fit the connectors, demanding a careful design for each particular case of beamforming. The length of the structures varies with frequency and the particular phase differences for each case so the margin is different for each structure. In general the margin is always bigger than 50mm on both ends. The lines at all frequencies and beamforming cases are terminated in a 50Ω line. The compensations for

possible input impedance mismatches due to mutual coupling were already performed by the algorithm used by SEQAR to calculate the optimal excitation coefficients. In case further tuning needs to be done the technique presented in [8] can be used.

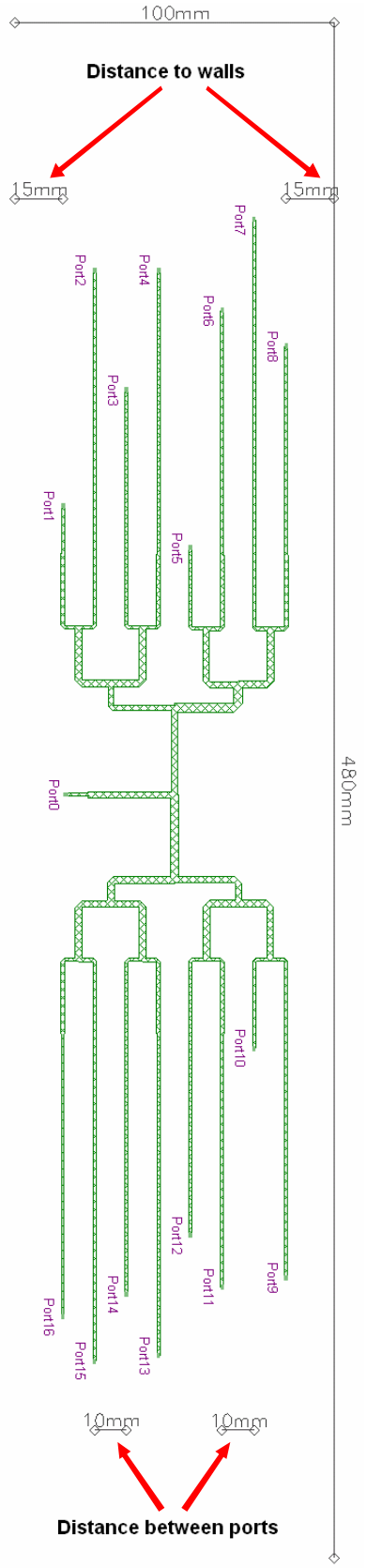

Fig. 4.6. An actual beamforming power divider with its dimensions (not in scale).

4.4 MATLAB program for power divider design

If the optimal beamforming coefficients obtained in chapter 3 are examined it can be noticed that neither the amplitudes nor phases follow any particular pattern, therefore tailor-made design is needed for each particular case. Performing by hand the design of the power dividers taking into account the characteristics and size they possess would be a time-consuming task subject to errors in the process and therefore it results impractical. This calls for the development of a method to accelerate the design of the power divider networks. An algorithm to expedite the design and its implementation in a MATLAB® program are presented in this section.

4.4.1 Program inputs

To be able to perform the necessary calculations the program needs the user to provide a number of inputs particular for each beamforming case. These inputs include the amplitudes and phases of the beamforming coefficients, the input and output impedances, and the length of a quarter-wave 50 Ω line at the design frequency. Optionally, the structure efficiency can be specified. All these parameters are explained in Table 4.1 and a snapshot of the input section of the program is shown in Fig. 4.7.

Table 4.1. Input parameters of the beamforming power divider design program in MATLAB.

Parameter	Description
Dimension	The dimension of the input square matrix. In the case of the calculations for this project it is fixed at 4x4; however this parameter is thought for more general cases where this program can be used in the future.
Z_{in}	Impedance of the input port. In this project it is fixed at 50Ω.
Z_{out}	Impedance of the output ports. In this project it is fixed at 50Ω.
Z_{base}	Impedance used to calculate the intermediate transformers, i.e. not the ones at the input or output. This parameter allows to match the intermediate quarter-wave transformers to an impedance different to 50Ω. This is particularly useful when the resulting line widths using 50Ω for the calculations are either too wide or too thin. In this project it is fixed at 30Ω as this allowed having lines wider than 1mm to minimize the errors due to tolerances in the etching process.
Efficiency	Efficiency of the structure. This allows to take into account the losses in the power dividers and it is used to provide a more realistic figure of the relative amplitudes in the output ports. In this project it was set to 0.95.
L_{50}	The length of a λ/4 line at the design frequency. This parameter is used to calculate the lengths of the output lines and should be provided as the guided wavelength depends on the material used and the width of the transmission line. It changes for each particular case.
Amplitudes	The matrix with optimal beamforming amplitudes obtained with SEQAR. Optionally, it can be a matrix filled with ones if a uniform distribution is used. This option is thought for future use with more general cases.
Line phases	The matrix with optimal beamsteering phases obtained with SEQAR. Optionally, it can be a matrix filled with zeros for broadside arrays is used. This option is thought for future use with more general cases.

```
%%%%% variable value input %%%%%

Dimension = 4;                          % Matrix dimension
Zin = 50;                               % Input impedance
Zout = 50;                              % Output impedance
Zbase = 30;                             % Base impedance for intermediate transformers
Efficiency = 0.95;                      % Structure efficiency, used to obtain the theoretical output relative levels for a a given efficiency
L50 = 111.7;                            % Lenght of a 50 Ohm line at the design frequency


%%%%% Load amplitude matrix %%%%%

%amplitudes = ones(Dimension)           % when there is a uniform distribution, choose this option for a ones matrix
                                        %
amplitudes = [                          % else write the matrix with the coefficients for each element in the desired order
     0.21    0.27    0.22    0.28
     0.49    0.51    0.51    0.61
     0.61    0.69    0.74    0.86
     0.92    0.90    1.00    1.00
];


%%%% Load phase matrix %%%%

%line phases = zeros(Dimension)                 % When a broadside array is desired
                                                %
line_phases = [                                 % else write the phases for each of the lines in the amplitude matrix in the same order
    166.43      69.73       -27.95      89.87
    -108.14     -171.42     -100.22     -25.73
    -96.2       -174.44     177.65      -110.25
    109.24      -9.91       84.04       -3.45
];
```

Fig. 4.7. Inputs for the beamforming network calculator in MATLAB.

4.4.2 The algorithm

The power dividers are a sequence of three-way unequal power dividers formed by quarter-wave transformers, followed by different lengths of 50Ω lines to provide the amplitudes and phases required for each beamforming case. The purpose of the algorithm is to perform the necessary calculations in order to find the impedances of all the quarter-wave transformers along the chain and the lengths of the output lines. In top of that, calculations should be performed in order to compensate for the losses on the different lengths of transmission line at different power levels.

A simplified flow diagram of the process the input data undergoes is shown in Fig. 4.8 below. A more detailed explanation of the process follows.

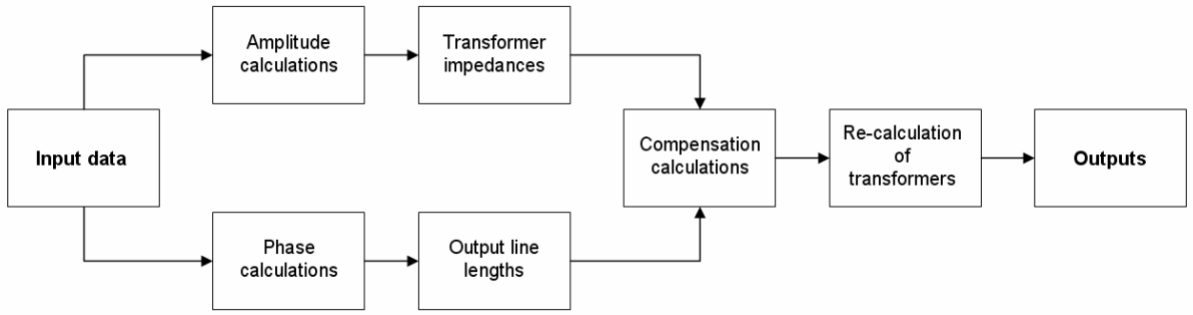

Fig 4.8. Simplified flow diagram of the beamforming network calculator program algorithm.

4.4.2.1 Output line lengths calculations

Lagging in phase implies a delay, thus if we assume that all signals in the dividers travel with the same velocity this means that a lagging signal travels a larger distance.

The optimal coefficient phases obtained with SEQAR are in the range [-180°, 180°] as the input signals are assumed to have a sinusoidal nature. To calculate the transmission line lengths of the last segment the first step is to find the line with the largest positive phase. This would become the reference and the shortest line in the layout. The biggest possible difference between two signals is 360° and hence the largest possible line in the output would be one wavelength longer than the shortest. The physical length for each particular case depends on the phase difference from the reference, the frequency, and the substrate material. In this project all output lines are 50Ω therefore the guided wavelength is constant for all lines at each of the design frequencies.

A considerable increase in output phase precision can be achieved if the structure is first simulated without the output lines and the phase differences between output ports are calculated and compensated. These phase differences might be caused by the difference in width of the divider arms at line junctions as well as by the line bends as seen in Fig. 4.9. In the case of junctions, the centers of the three segments have been placed in one point, with the intention of having a symmetrical structure and to avoid fringing effects on the lower discontinuity that vanishes when segments are merged. In the upper part of the junction there is an impedance step or discontinuity whose effect according to [16] is an increase in the effective length of the wider line due to fringing effects. The fringing effects in microstrip lines can be represented in a circuit point of view as a shunt impedance and physically as an extra length of transmission line with the same characteristics as the actual physical line as seen in Fig. 4.10.

The fact that only quarter-wave transformers are used to form the dividers and the physical implementation of the junctions might have some effects that are difficult to ponder. The input and output transformers are one quarter-wavelength long, however when merged to form the junction they become shorter and hence the impedance transforming might be incomplete or imprecise. This can cause inaccuracies in the amplitudes obtained at the output ports due to an accumulation of small errors in the power division throughout the structure. In terms of phase, the approach used to calculate the distance traveled by input signals assumes that they follow a straight line in the center of the transmission line until the end of the transformer and then turn 90° as seen in Fig 4.11. This approximation may not be accurate as the signals travel mostly near the edges of the line where the current is concentrated and are most likely to turn with a softer angle rather than with a 90° one.

In the case of the bends it was decided to cut the corners out with a 45° angle so as to avoid the capacitive effects of the concentration of electric field at the outer corner [17]. The distance traveled by the signal was approximated as a straight line from the center of the horizontal segment to the center of the vertical segment as seen in Fig. 4.12. This estimation may not be accurate, [16] proposes a more precise way to calculate this distance.

The effects of these approximations at frequencies smaller than 10 GHz are really small for a single transformer but it is important to consider them as they might be considerable for the whole chain.

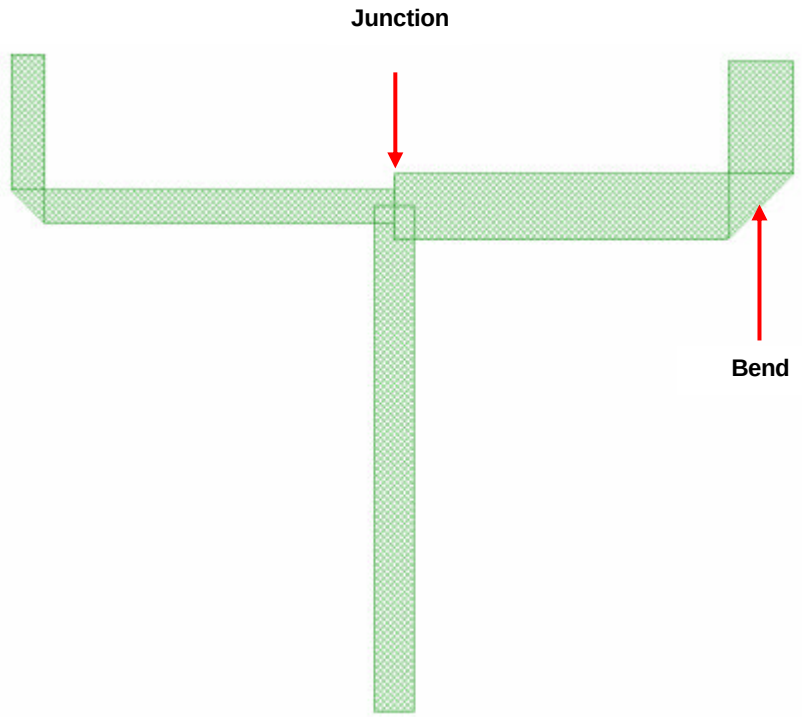

Fig. 4.9. An example of a power divider with highlighted junction and bend.

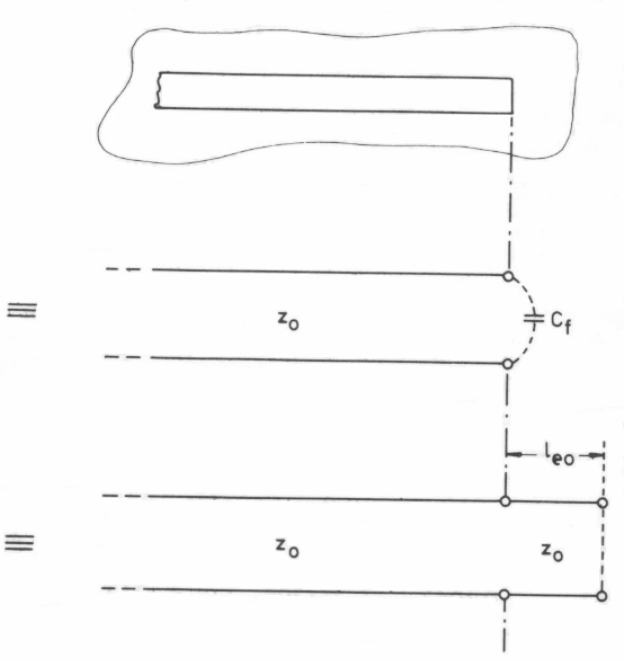

Fig. 4.10. Equivalents of a microstrip line due to fringing effects. The top picture shows the original line, the middle picture shows the circuit equivalent, and the picture on bottom shows the transmission line equivalent.

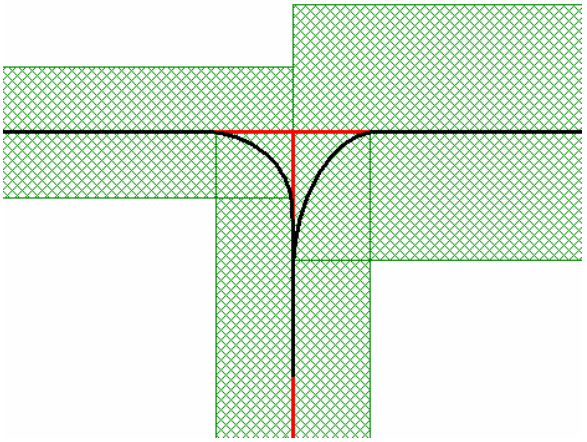

Fig. 4.11. A magnified view of a junction. The red line indicates the estimated trajectory of the wave and the black line shows a more realistic trajectory.

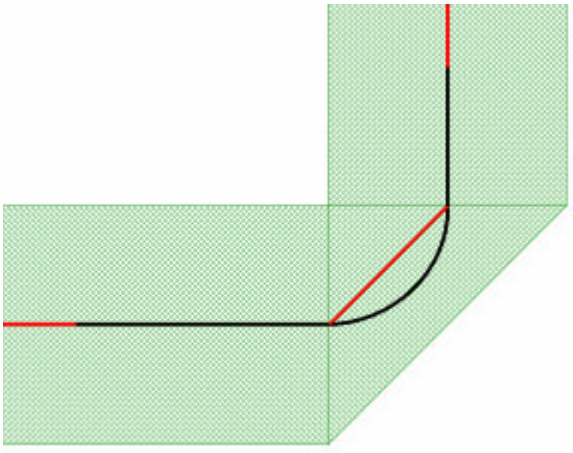

Fig. 4.12. A magnified view of a bend. The red line indicates the estimated trajectory of the wave and the black line shows a more realistic trajectory.

4.4.2.2 Amplitude and transformer impedance calculations

Once the lengths of the lines in the output level are known, and as a previous step before calculating the transformers to be used along the chain, it is necessary to sort them in such a way that the length difference between two contiguous ports is equal or larger than 13 mm. This is needed, as explained in section 4.3.1, to prevent the connectors from colliding with each other.

As a first step for calculating the transformer impedances the amplitude coefficients are used to find a normalization constant that will allow to reference the input power as unity or the efficiency value given as input (Equation 4.3).

$$Normalization = \frac{Efficiency}{\sum_{1}^{16} Amplitudes} \tag{4.3}$$

The amplitude coefficient matrix is then multiplied by this normalization constant and added on each level (Fig 4.13) to obtain the normalized output power value of each transformer on every stage.

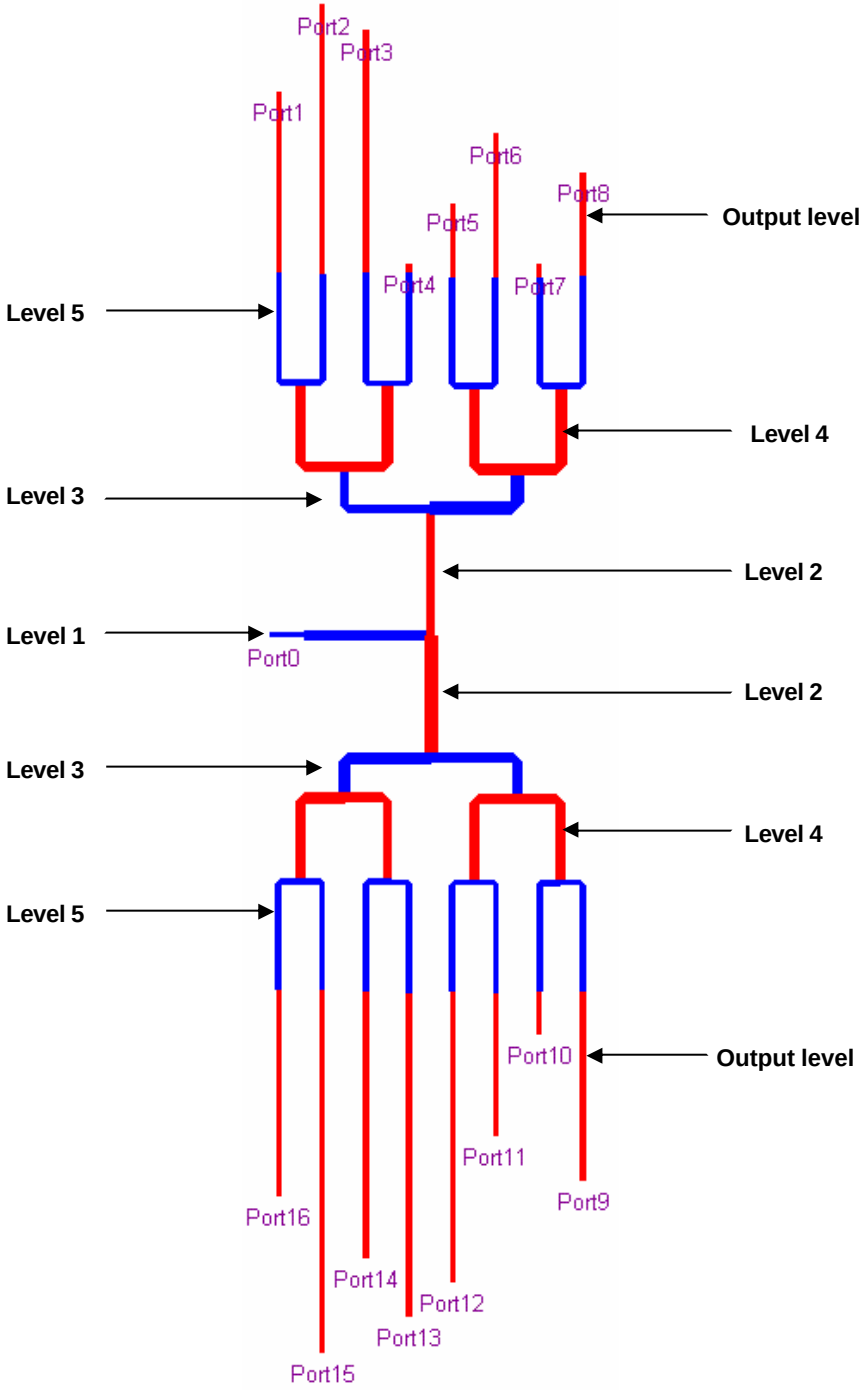

Fig. 4.13. Identification of the transformer levels.

Once these powers are known, the ratio of power that should be provided by each of the dividers at each junction can be calculated and the impedances of the transformers calculated as follows

$$K = \frac{P_{out2}}{P_{out3}} \tag{4.4}$$

$$Z_2 = Z_{base}\sqrt{\frac{1+K^2}{K^3}} \tag{4.5}$$

$$Z_3 = Z_{base}\sqrt{K\left(1+K^2\right)} \tag{4.6}$$

where K is the ratio between output powers in ports 2 and 3 and Z_2, Z_3, and Z_{base} are the impedances of the divider arm where less power should go, the arm where more power should go, and the reference or base impedance respectively.

The actual value of the transformers is calculated following a top-bottom approach. First the transformers in level 5 are calculated by matching each of the values of Z_2 or Z_3 to the specified output impedance, in this case 50Ω

$$T_{L5} = \sqrt{Z_{out} \cdot Z_{2,3(L5)}} \tag{4.7}$$

The transformers on the subsequent levels are calculated by matching the corresponding Z_2 or Z_3 to the parallel of the transformers in the upper level, i.e. the impedance at the junction

$$T_{levelN} = \sqrt{Z_{2,3N} \cdot \left(Z_{2(N+1)} \| Z_{3(N+1)}\right)} \tag{4.8}$$

Finally, the transformer in level 1 matches the input impedance to the parallel of the transformers in level 2

$$T_{L1} = \sqrt{Z_{in} \cdot \left(Z_{2(L2)} \| Z_{3(L2)}\right)} \tag{4.9}$$

When this step is completed there is need to calculate the points where the transformers will bend in order to fit the structure within the specified area. The way these are calculated is explained in the following sub-section.

4.4.2.3 Bend position calculations

If the selected geometry is observed it can be seen that transformers from level 3 to 5 need to be bended so as to fit them in the given area of the box that contains them. The width of the dividers including connectors is, as mentioned earlier, fixed to 83mm; therefore in order to have a symmetrical structure it was decided to fix the points where the transformers bend to a distance of 20mm, 30mm, and 35mm from the center out for levels 3, 4, and 5 respectively. The total width of the corresponding levels is 40mm, 20mm, and 10mm measured from the center of the vertical lines on both sides as seen in Fig. 4.14.

Nevertheless, the guided wavelength varies for the different frequencies of operation and so the points where the lines bend change depending on frequency. In the case of the dividers at 1.57 GHz this scheme was changed because the lines in level 3 were too short and would have been too close to those of level 4 if bended at 20mm. In order to avoid mutual coupling between the lines in level 3 and level 4 the scheme shown in Fig. 4.15 was adopted.

A short MATLAB program, independent of the beamforming power divider calculator, to compute the exact point where the lines should bend was developed. The inputs of this program are simply the guided wavelengths for each of the transformers in the chain. Then, depending on the frequency of operation and assuming that the signal at the bend describes a straight line as in Fig. 4.12, the physical lengths of all the sub-segments along the chain are calculated and given as the program output.

When all the computations presented in the previous sub-sections are completed, all the information necessary to create a model of the dividers in Ansoft Designer is available. The model can then be drawn in a faster way.

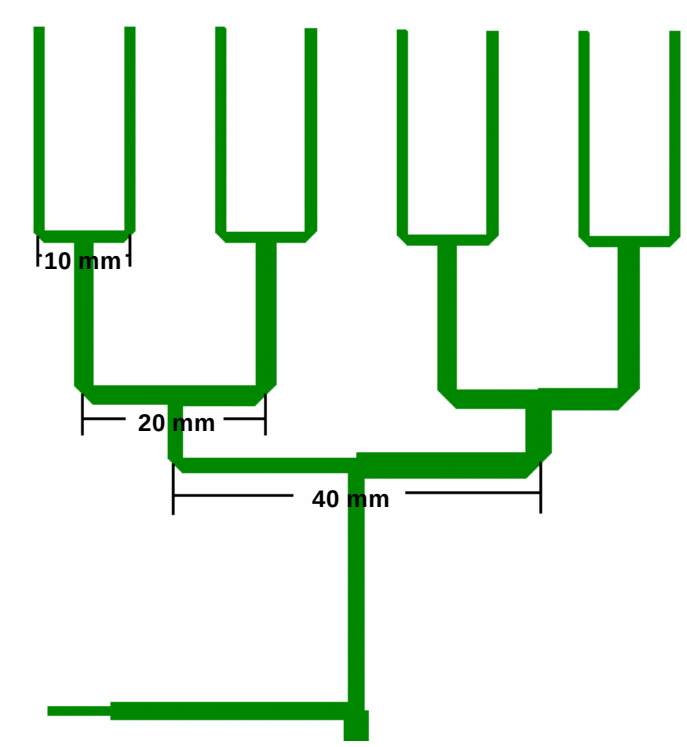

Fig. 4.14. Width measures of levels 3, 4, and 5 for the dividers at 1.19 GHz and 1.27 GHz.

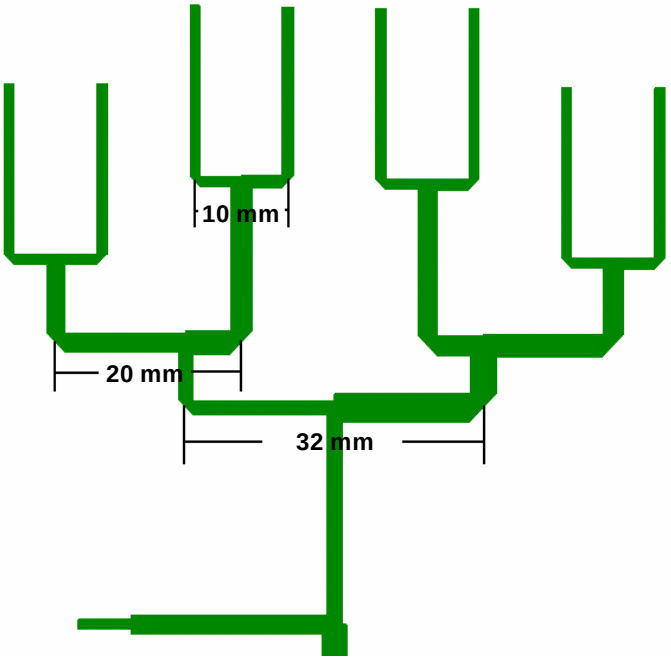

Fig. 4.15. Width measures of levels 3, 4, and 5 for the divider at 1.57GHz.

4.4.3 Program outputs: an example

The outputs obtained from the beamforming power divider calculator program for case D (θ=44° and ϕ=120° at 1.19 GHz) presented in chapter 3 are shown in Fig. 4.16 to Fig. 4.18 in a tabular and graphical way. It is important to mention that data has been ordered in the same fashion as the output ports, i.e. in a clockwise manner (from left to right on top and from right to left on bottom).

4.4.3.1 Output line physical lengths

Port	1	2	3	4	5	6	7	8
Physical length (mm)	4.92	34.93	65.30	28.76	90.81	110.47	88.32	65.19

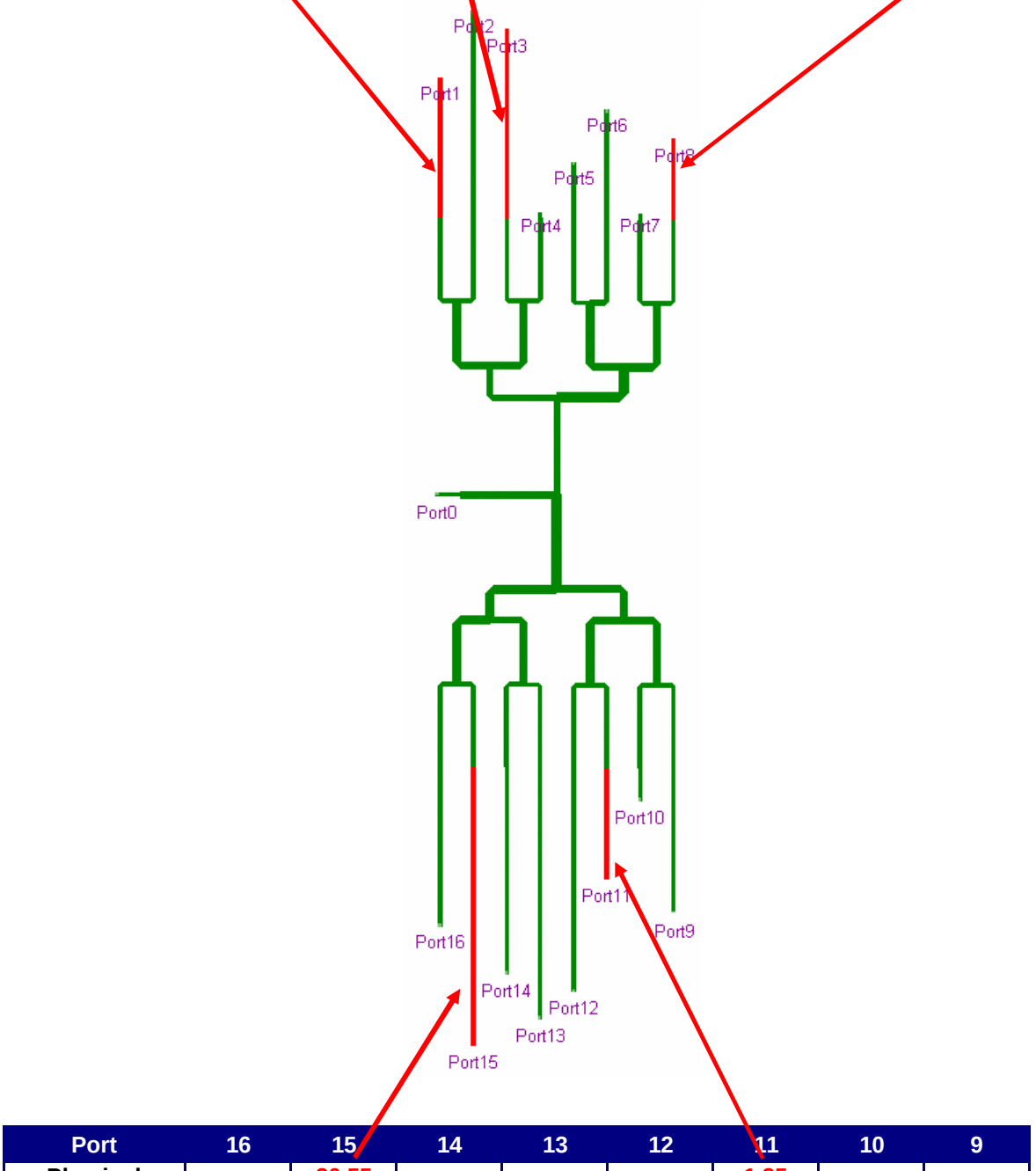

Port	16	15	14	13	12	11	10	9
Physical length (mm)	57.77	30.55	59.53	22.76	90.67	1.35	110.52	86.44

Fig. 4.16. Physical lengths of the lines in the output level for the θ=44° and ϕ=120° at 1.19 GHz case.

4.4.3.2 Transformer impedances

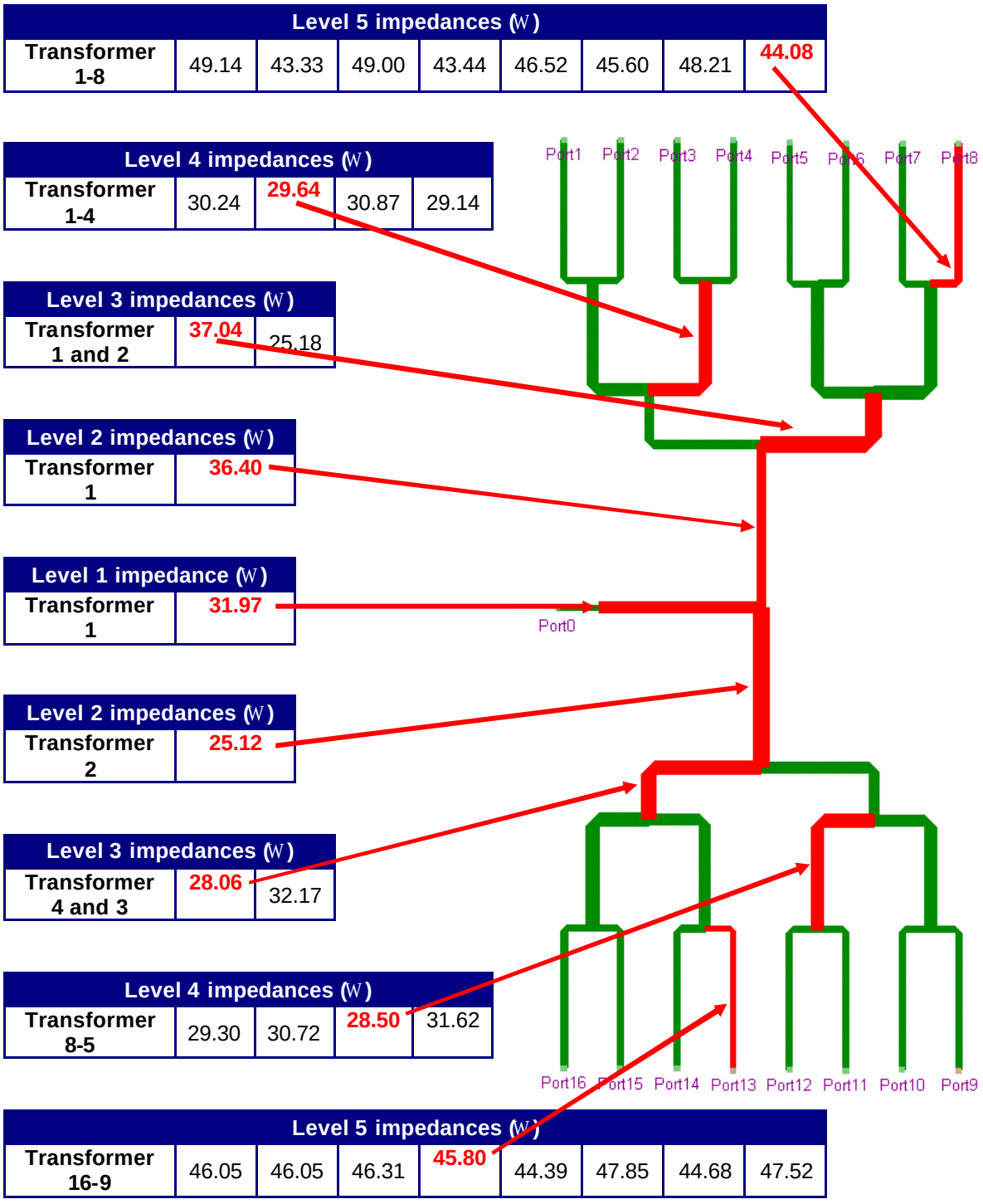

Fig. 4.17. Transformer impedance values for the θ=44° and ϕ=120° at 1.19 GHz case.

4.4.3.3 Relative power levels at each level

Knowing the relative power in dB at the output of every transformer on each of the levels for a given efficiency can be useful for design verification in intermediate stages of the model design. One of the program outputs, as shown in Fig. 4.18, is an approximate value of these relative powers and is later used to validate the simulation results of the power dividers.

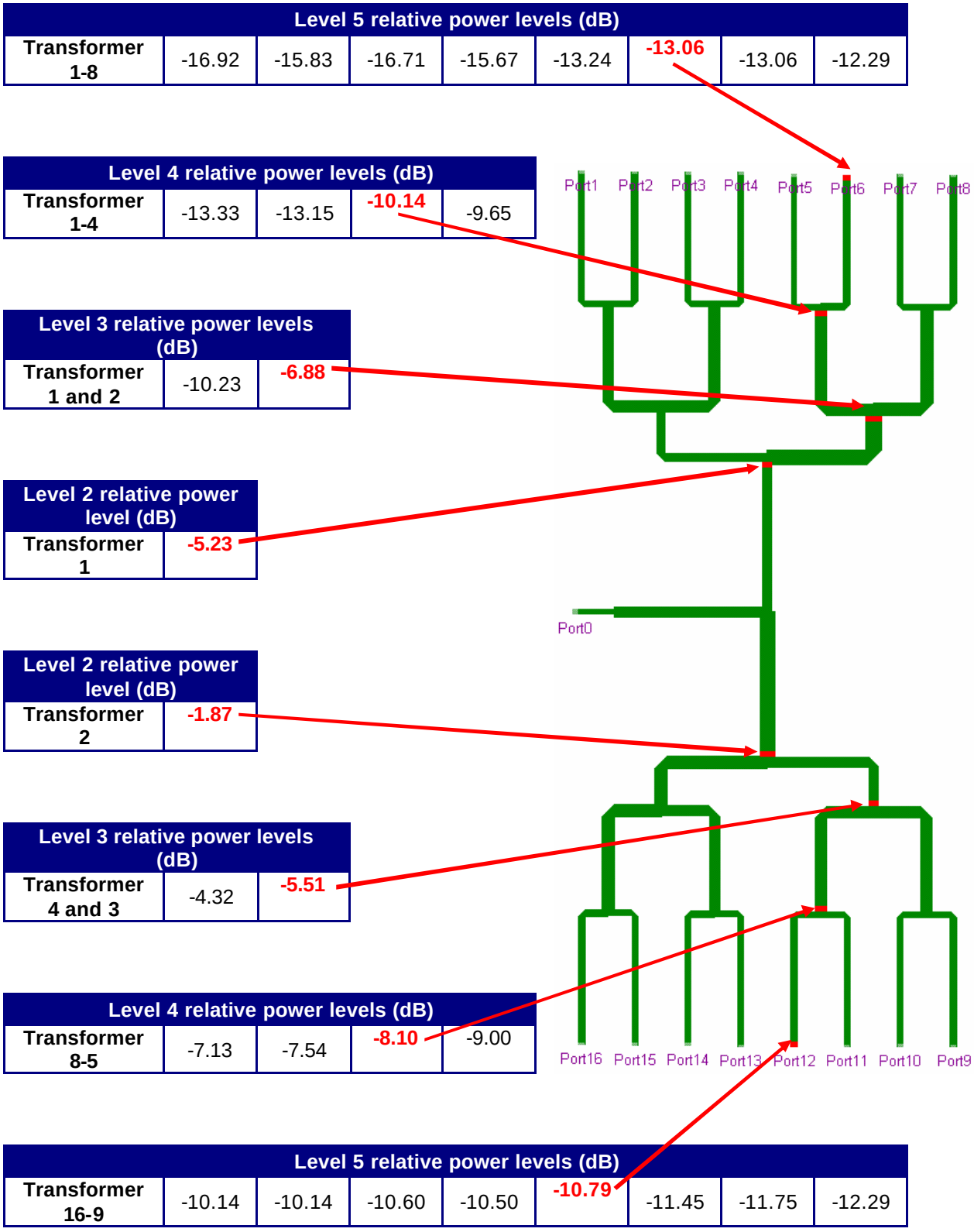

Fig. 4.18. Relative amplitudes in dB at each level for the θ=44° and ϕ=120° at 1.19 GHz case.

This section showed an example of the output for one of the beamforming cases studied in this project. The full MATLAB program code can be found in Appendix A.

4.5 Models and simulation results in Ansoft Designer® and HFSS®

In the previous sections the procedure followed to design the beamforming power dividers was presented. With this information in hand it is possible to create models of the power dividers in order to verify their performance before manufacturing them. These models were created with the Planar EM Simulator of Ansoft Designer® and later exported to HFSS®. This section presents the models and the results of the simulations obtained with them are compared with the theoretical results presented in chapter 3.

4.5.1 Power divider models and simulation results

In this section the models developed in Ansoft Designer and HFSS for each of the beamforming power dividers are presented along with a summary of the simulation results. Each of the cases is presented following the same structure: first the physical layout in Designer is presented, then a table comparing the 'ideal' results (as presented in the previous chapter) with the simulation results, and finally a comparison of the ideal radiation patterns with those obtained using the output powers obtained from simulations on the simplified model of the antenna array are presented.

Case A: q=20° f=120° @ 1.19 GHz, SLL = -20 dB

The Designer and HFSS models for this case are presented in Fig. 4.19 and 4.20 respectively. Table 4.2 presents the comparison between the ideal (SEQAR) case and the Designer and HFSS simulated results. Only one figure is presented in the case of phases as the results from Designer and HFSS are almost identical in this parameter. The radiation patterns in Fig. 4.21 and 4.22 show a good agreement between the reference case and the simulations. Side lobe level is slightly higher than -20dB for simulation, however the pattern is almost unchanged. The performance in terms of cross polarization is very good as the LHCP component stays below -23 dB for all angles.

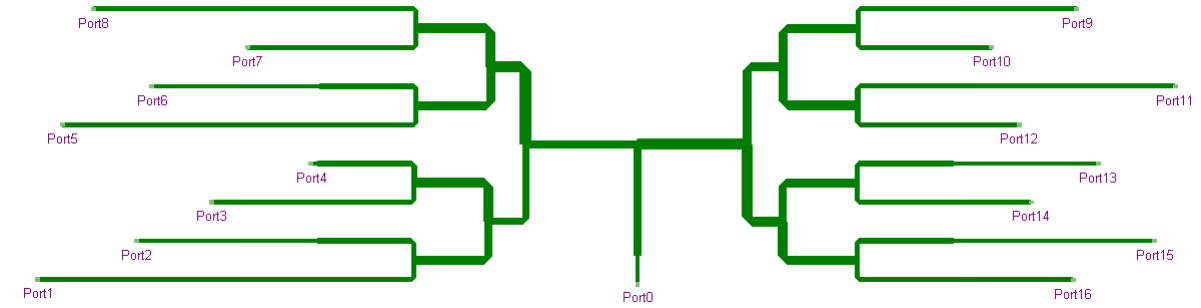

Fig. 4.19. Designer model of the θ=20° ϕ=120° @ 1.19 GHz divider.

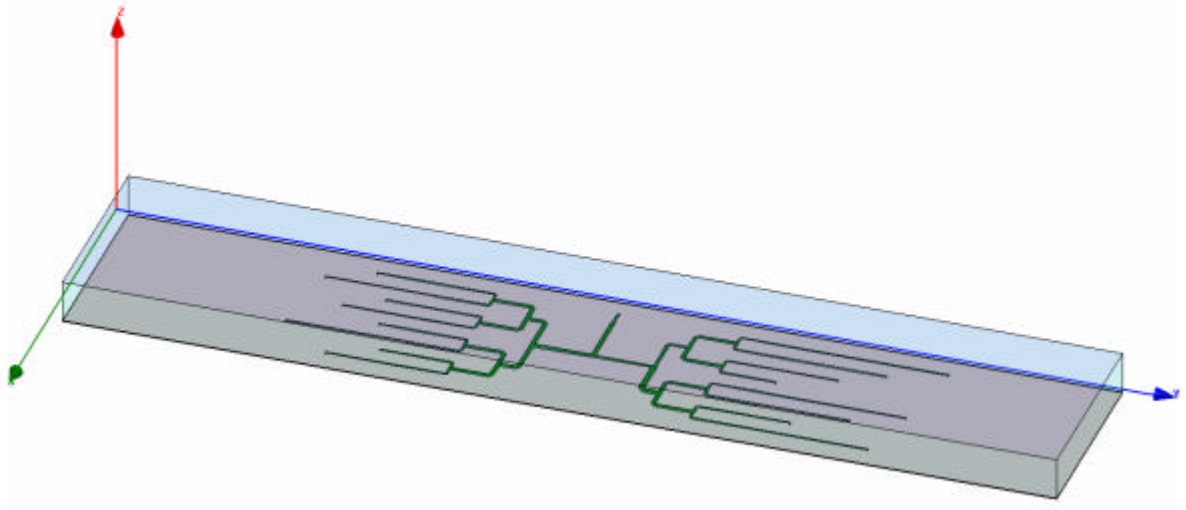

Fig. 4.20. HFSS model of the θ=20° ϕ=120° @ 1.19 GHz divider.

Table 4.2. Result comparison between the ideal case and simulations for the θ=20° ϕ=120° @ 1.19 GHz case.

Divider q=20° f=120° @ 1.19 GHz						
Identifier		**Amplitudes**			**Normalized phases**	
		Ideal	**Designer**	**HFSS**	**Ideal**	**Simulated**
Antenna port	Divider port	Relative level dB	Obtained dB	Obtained dB	Phase (°)	Phase (°)
13	1	**-16.53**	-16.68	-16.65	**0**	0
16	2	**-16**	-16.12	-16.07	**76.78**	75.03
1	3	**-16**	-15.92	-16.18	**135.89**	135.26
4	4	**-15.38**	-15.58	-15.11	**-146.7**	-146.82
14	5	**-12.44**	-12.62	-12.56	**19.8**	20.28
5	6	**-12.09**	-12.07	-12.42	**89.61**	88.63
2	7	**-11.96**	-11.84	-12.23	**163.9**	163.9
9	8	**-12.23**	-12.39	-12.29	**43.79**	42.26
12	9	**-12.02**	-12	-12.16	**122.96**	122.32
3	10	**-12.02**	-12.27	-11.75	**-171.12**	-170.14
15	11	**-11.89**	-12.07	-11.91	**45.57**	44.32
8	12	**-11.64**	-11.6	-11.96	**167.25**	167.92
11	13	**-10.2**	-10.25	-10.4	**105.51**	103.95
7	14	**-11.34**	-11.42	-11.39	**158.6**	158.97
10	15	**-10.15**	-10.24	-10.27	**61.39**	60.53
6	16	**-10.37**	-10.29	-10.8	**125.54**	125.68

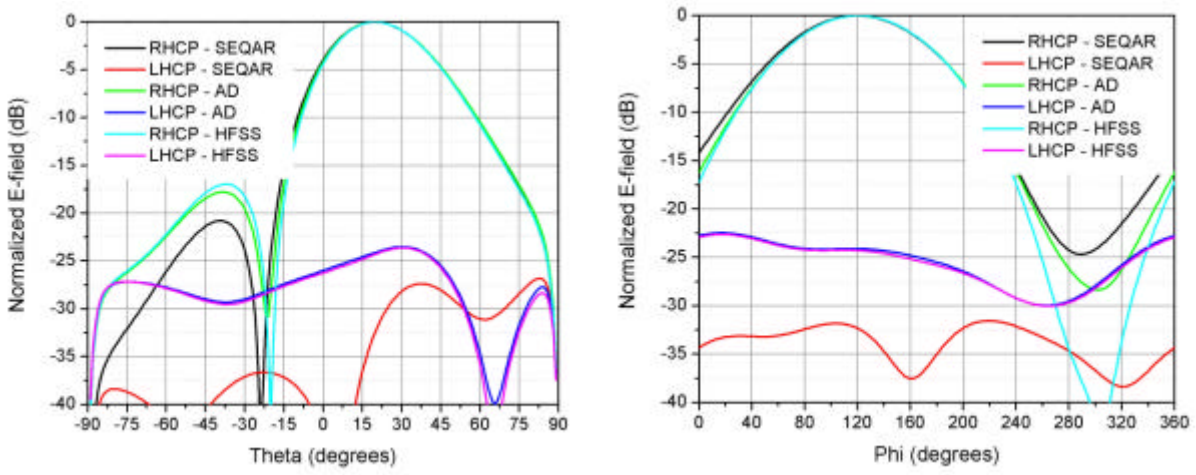

(a) (b)

Fig. 4.21. Comparison between the radiation characteristics obtained with SEQAR and those obtained using the output powers of the divider simulations in Designer and HFSS on the simplified array model for the θ=20° ϕ=120° @ 1.19 GHz case. ϕ = 120° (a) and (b) θ = 20° cuts.

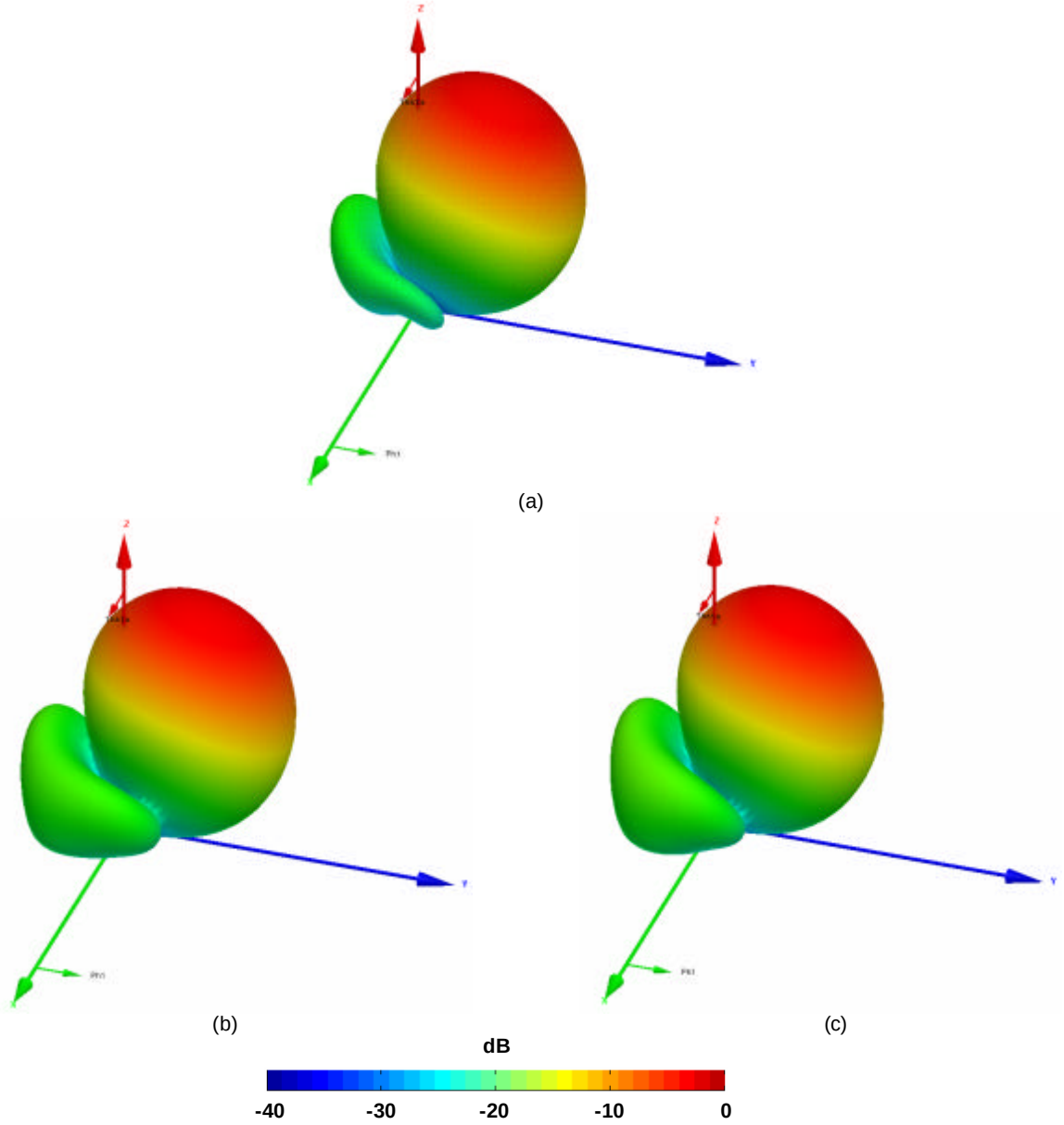

Fig. 4.22. Comparison between the 3D radiation patterns for the SEQAR case (a), Designer (b), and HFSS (c) simulations for the θ=20° ϕ=120° @ 1.19 GHz case.

Case B: q=20° f=45° @ 1.27 GHz, SLL = -20 dB

This case shows similar results to those of the preceding one. The Designer and HFSS models for this case are presented in Fig. 4.23 and 4.24 respectively. Table 4.3 presents the comparison between the SEQAR case and the Designer and HFSS simulated results. The radiation patterns in Fig. 4.25 and 4.26 show a good agreement between the reference case and the simulations especially for the Designer case. Side lobe level is slightly improved compared to the previous case, but still above -20dB. The performance in terms of cross polarization is again very good.

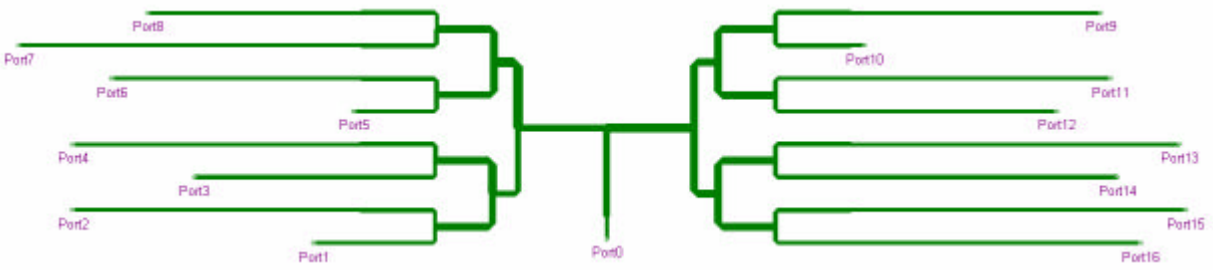

Fig. 4.23. Designer model of the θ=20° ϕ=45° @ 1.27 GHz divider.

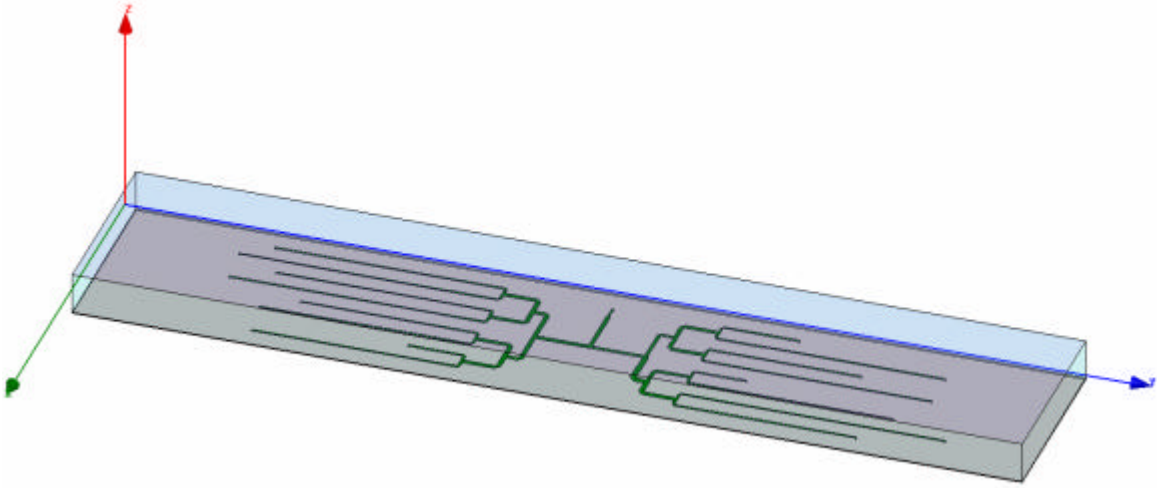

Fig. 4.24. HFSS model of the θ=20° ϕ=45° @ 1.27 GHz divider.

Table 4.3. Result comparison between the ideal case and simulations for the θ=20° ϕ=45° @ 1.27 GHz case.

Divider q=20° f=45° @ 1.27 GHz						
Identifier		**Amplitudes**			**Normalized phases**	
		Ideal	**Designer**	**HFSS**	**Ideal**	**Simulated**
Antenna port	Divider port	Relative level dB	Obtained dB	Obtained dB	Phase (°)	Phase (°)
16	1	**-15.71**	-15.77	-15.66	**0**	0
4	2	**-15.71**	-15.7	-15.97	**122.79**	120.14
1	3	**-15.57**	-15.73	-15.62	**-117.03**	-118.01
13	4	**-15.17**	-15.02	-15.54	**122.79**	120.14
12	5	**-13.00**	-13.28	-12.93	**-162.35**	-162.87
9	6	**-12.36**	-12.37	-12.61	**152.53**	150.16
8	7	**-11.73**	-11.78	-12.03	**70.4**	66.5
5	8	**-11.85**	-11.86	-12.09	**-162.35**	-162.87
3	9	**-11.73**	-11.69	-11.99	**161.75**	161.36
15	10	**-11.40**	-11.54	-11.45	**33.29**	32.6
6	11	**-11.62**	-11.65	-12.01	**122.93**	120.25
2	12	**-11.24**	-11.53	-11.24	**-155.4**	-157.1
11	13	**-10.48**	-10.63	-10.72	**83.31**	78.37
10	14	**-11.24**	-11.21	-11.66	**145.89**	142.55
14	15	**-10.89**	-11	-11.08	**78.38**	74.59
7	16	**-11.04**	-10.99	-11.5	**122.93**	120.25

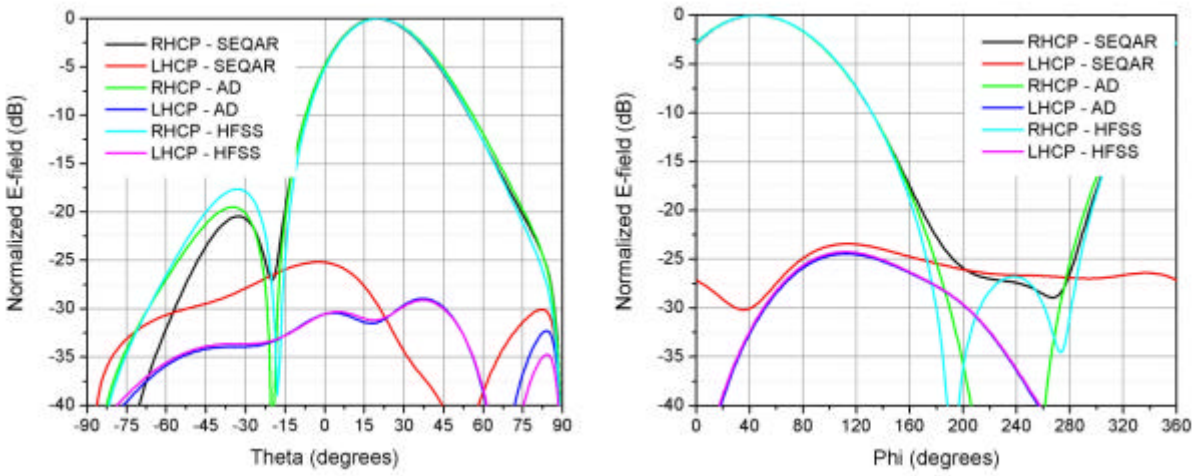

Fig. 4.25. Comparison between the radiation characteristics obtained with SEQAR and those obtained using the output powers of the divider simulations in Designer and HFSS on the simplified array model for the θ=20° ϕ=45° @ 1.27 GHz case. ϕ = 45° (a) and (b) θ = 20° cuts.

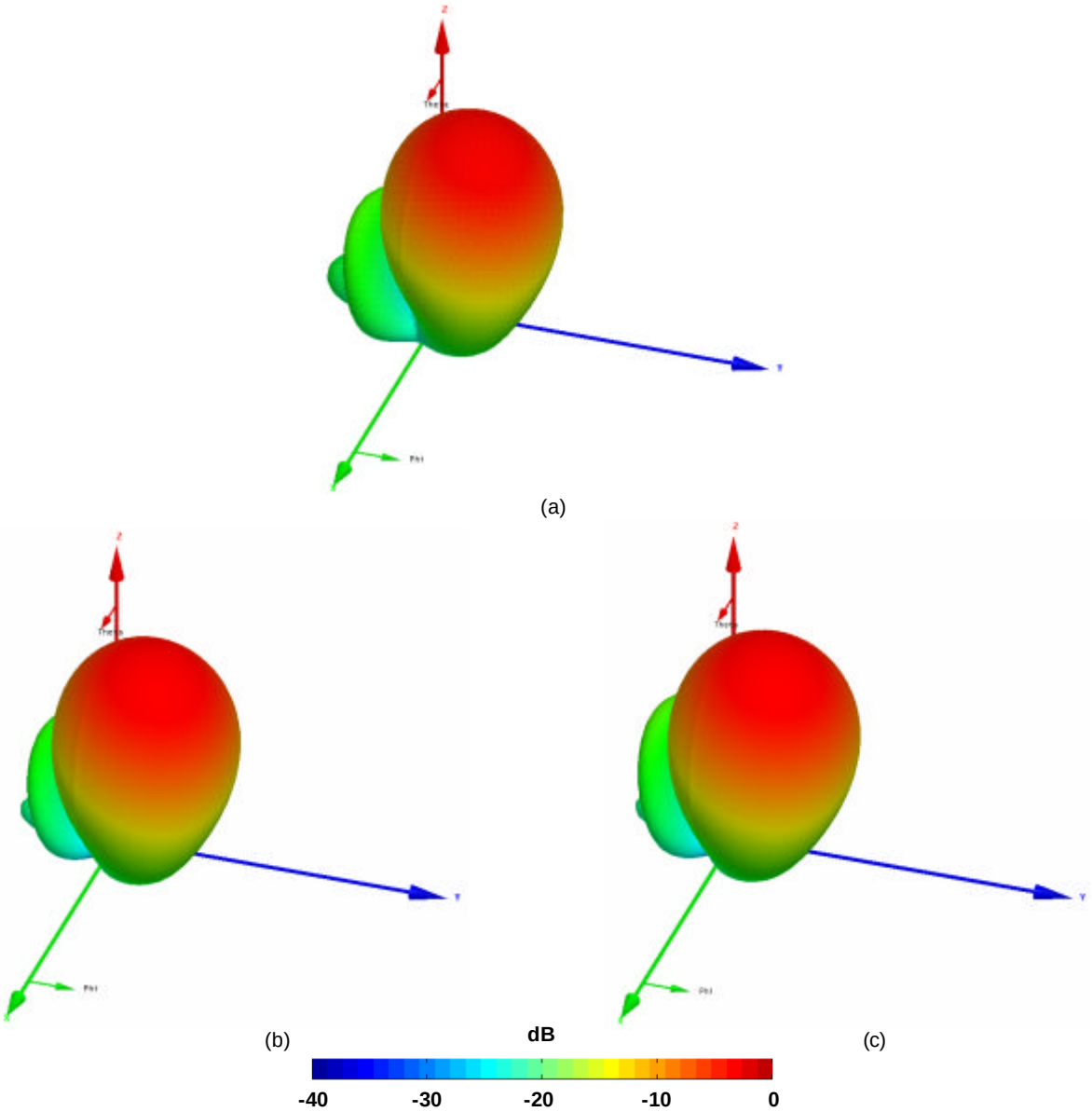

Fig. 4.26. Comparison between the 3D radiation patterns for the SEQAR case (a), Designer (b), and HFSS (c) simulations for the θ=20° ϕ=45° @ 1.27 GHz case.

Case C: q=20° f=290° @ 1.57 GHz, SLL = -20 dB

This case shows results that differ slightly to those of the preceding ones. The Designer and HFSS models for this case are presented in Fig. 4.27 and 4.28 respectively. Table 4.4 presents the comparison between the SEQAR case and the Designer and HFSS simulated results. The radiation patterns in Fig. 4.29 and 4.30 show that the simulation cases have better performance in terms of side lobe level suppression and cross polarization than the reference case.

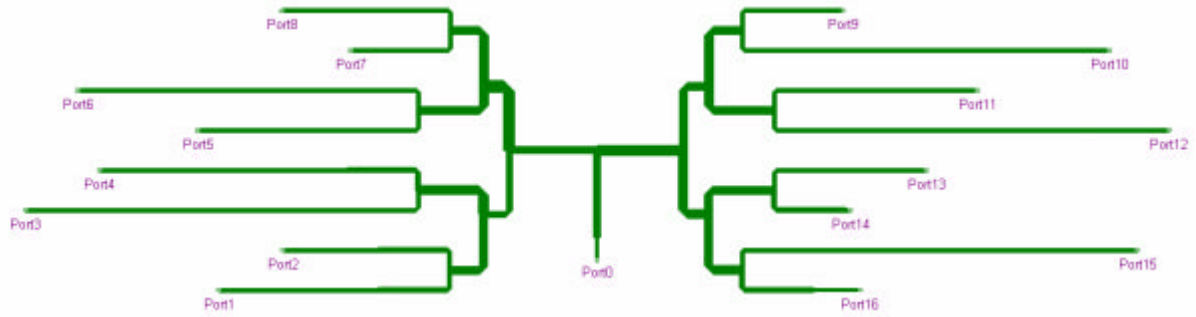

Fig. 4.27. Designer model of the θ=20° ϕ=290° @ 1.57 GHz divider.

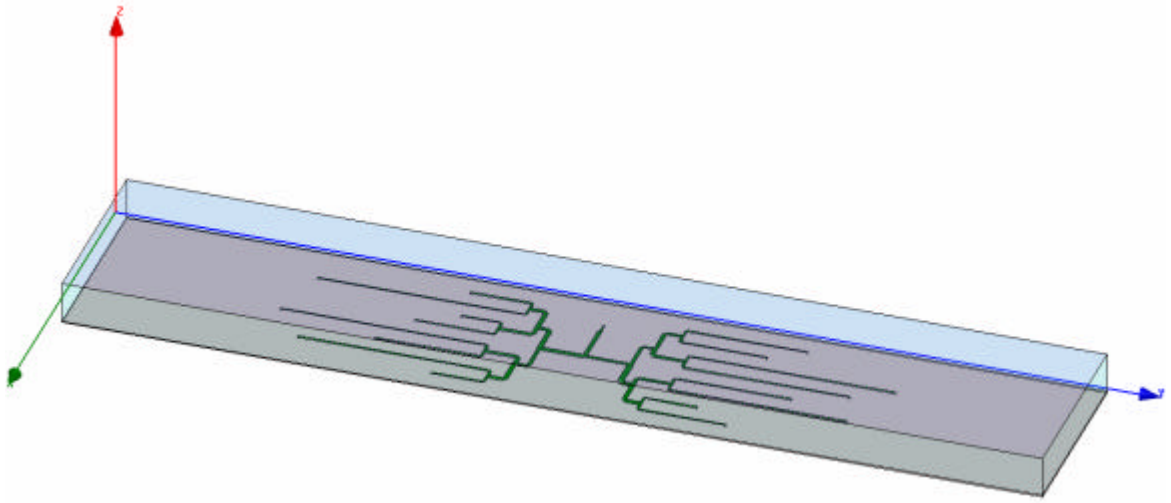

Fig. 4.28. HFSS model of the θ=20° ϕ=290° @ 1.57 GHz divider.

Table 4.4. Result comparison between the ideal case and simulations for the θ=20° ϕ=290° @ 1.57 GHz case.

Divider q=20° f=290° @ 1.57 GHz						
Identifier		**Amplitudes**			**Normalized phases**	
		Ideal	**Designer**	**HFSS**	**Ideal**	**Simulated**
Antenna port	Divider port	Relative level dB	Obtained dB	Obtained dB	Phase (°)	Phase (°)
4	1	**-17.16**	-17.38	-16.82	**0**	0
1	2	**-16.94**	-16.86	-16.93	**63.57**	64.33
16	3	**-16.53**	-16.7	-16.17	**-160.52**	-162.71
13	4	**-15.33**	-15.43	-15.23	**-87.22**	-88.15
3	5	**-12.63**	-12.75	-12.55	**13.3**	13.2
14	6	**-12.47**	-12.38	-12.73	**-105.89**	-105.7
12	7	**-12.32**	-12.32	-12.24	**133.33**	134.65
8	8	**-11.96**	-11.77	-12.13	**64.92**	65.14
5	9	**-11.89**	-11.75	-11.87	**133.6**	134.69
15	10	**-11.69**	-11.44	-11.77	**-131.62**	-132.78
2	11	**-11.82**	-11.79	-12.18	**31.71**	32.56
9	12	**-11.38**	-11.39	-11.61	**-158.56**	-159.08
7	13	**-10.81**	-10.67	-11.18	**82.79**	83.86
11	14	**-10.41**	-10.45	-10.47	**158.18**	159.58
10	15	**-10.92**	-10.97	-11.18	**-158.37**	-158.93
6	16	**-9.95**	-9.83	-10.17	**117.17**	119.04

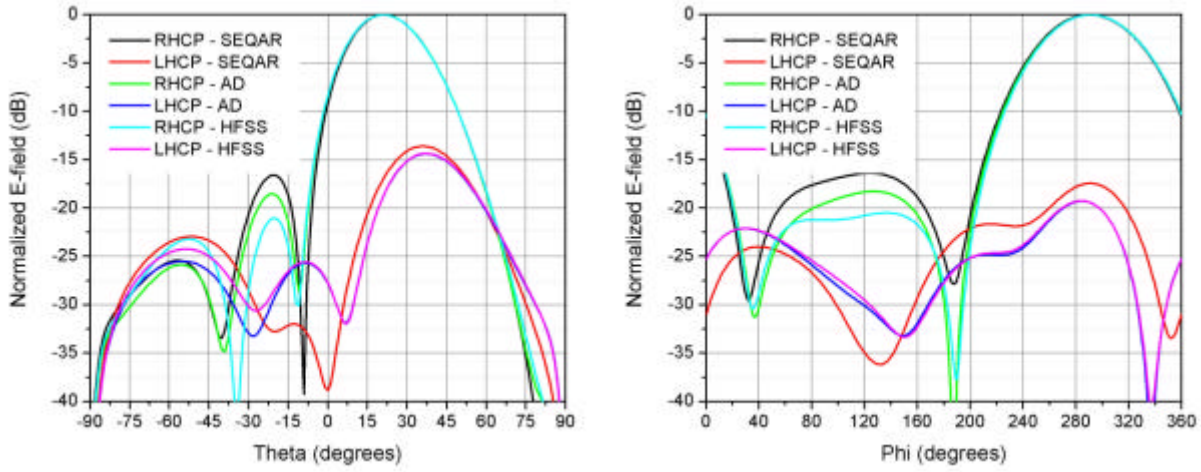

(a) (b)

Fig. 4.29. Comparison between the radiation characteristics obtained with SEQAR and those obtained using the output powers of the divider simulations in Designer and HFSS on the simplified array model for the θ=20° ϕ=290° @ 1.57 GHz case. ϕ = 290° (a) and (b) θ = 20° cuts.

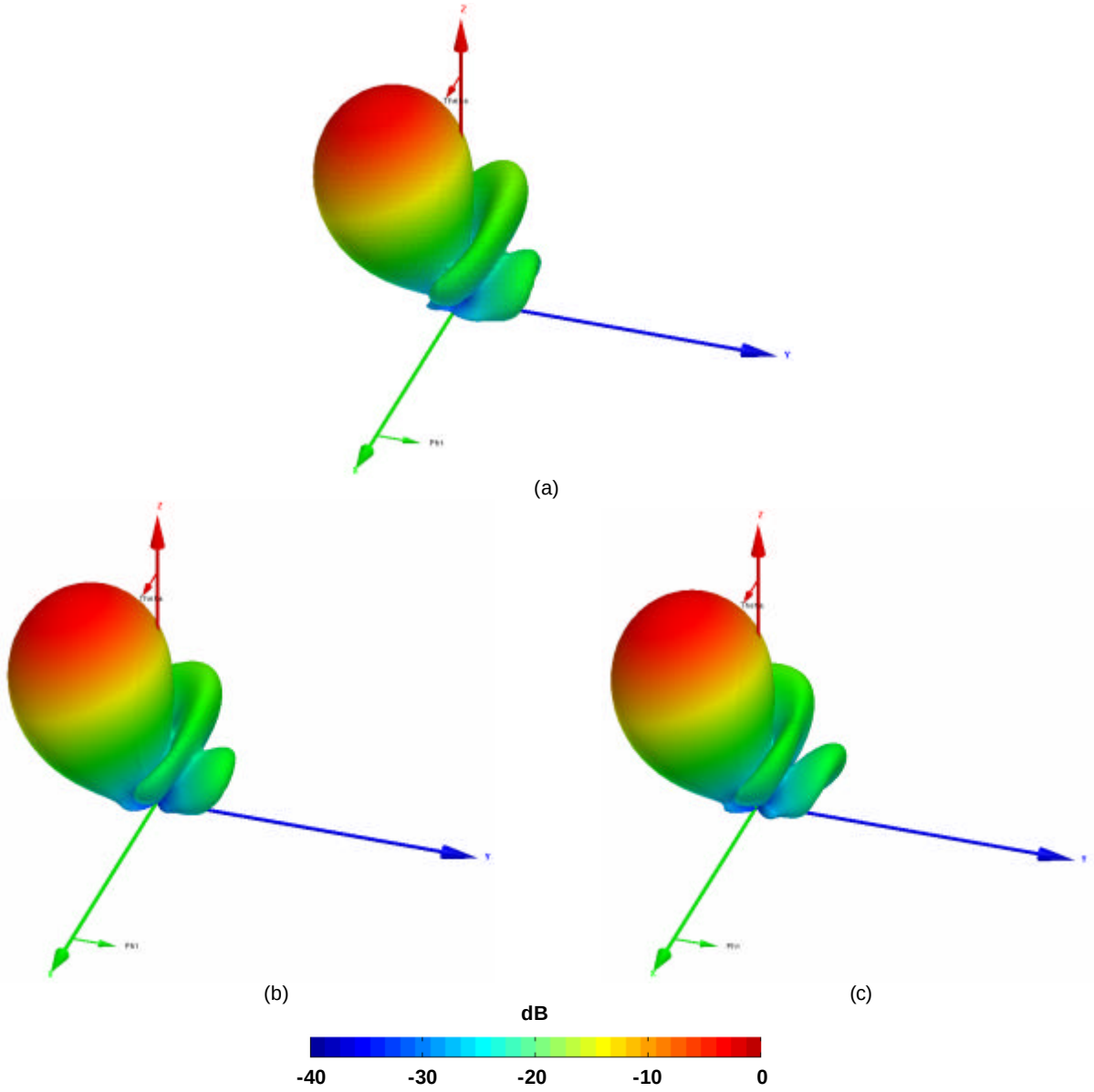

Fig. 4.30. Comparison between the 3D radiation patterns for the SEQAR case (a), Designer (b), and HFSS (c) simulations for the θ=20° ϕ=290° @ 1.57 GHz case.

Case D: q=44° f=120° @ 1.19 GHz, SLL = -20 dB

This case is probably the one where the simulation results follow the reference case with more precision. The Designer and HFSS models for this case are presented in Fig. 4.31 and 4.32 respectively. Table 4.5 presents the comparison between the SEQAR case and the Designer and HFSS simulated results. The radiation patterns in Fig. 4.33 and 4.34 show that the simulation cases have a performance than closely resembles that of the reference case.

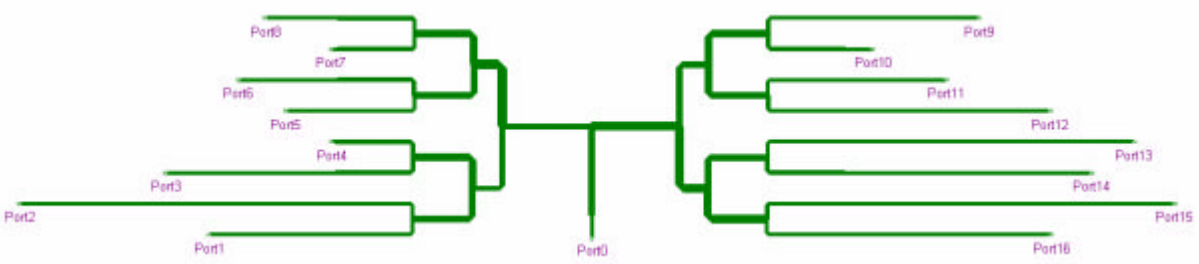

Fig. 4.31. Designer model of the θ=44° ϕ=120° @ 1.19 GHz divider.

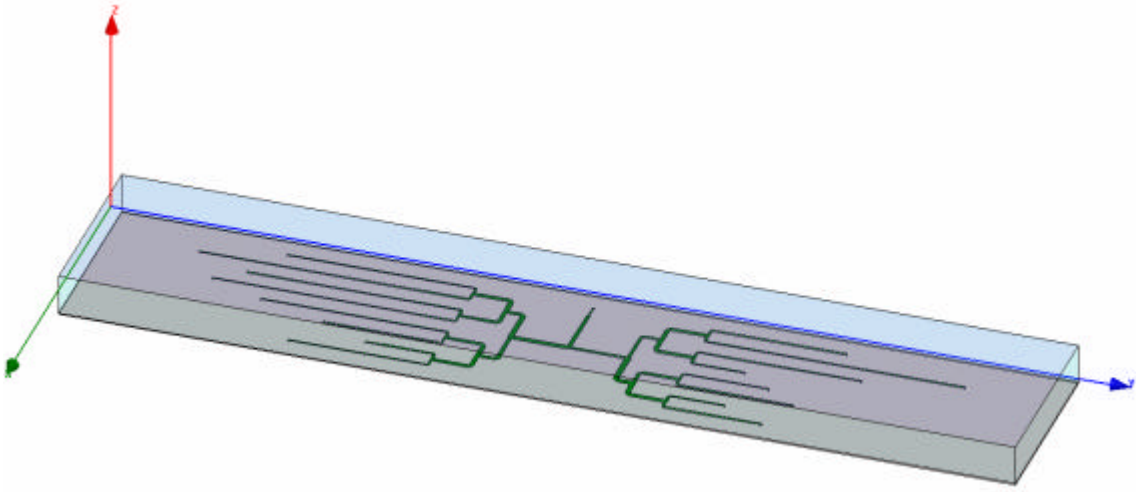

Fig. 4.32. HFSS model of the θ=44° ϕ=120° @ 1.19 GHz divider.

Table 4.5. Result comparison between the ideal case and simulations for the θ=44° ϕ=120° @ 1.19 GHz case.

Divider q=44° f=120° @ 1.19 GHz						
Identifier		**Amplitudes**			**Normalized phases**	
		Ideal	**Designer**	**HFSS**	**Ideal**	**Simulated**
Antenna port	Divider port	Relative level dB	Obtained dB	Obtained dB	Phase (°)	Phase (°)
13	1	**-16.83**	-17.14	-16.64	**0**	0
16	2	**-16.60**	-16.99	-16.25	**173.68**	172.7
1	3	**-16.16**	-16.29	-16.07	**-43.28**	-44.78
4	4	**-16.16**	-16.26	-15.96	**119.16**	119.06
3	5	**-13.36**	-13.58	-13.55	**74.92**	77.54
2	6	**-12.31**	-12.35	-12.52	**26.86**	27.95
15	7	**-12.31**	-12.38	-12.49	**117.75**	119.24
14	8	**-12.39**	-12.17	-12.86	**53.83**	56.41
7	9	**-11.98**	-11.89	-12.19	**-5.87**	-6.34
9	10	**-11.82**	-11.82	-11.95	**96.67**	99.07
8	11	**-11.82**	-11.73	-12.15	**25.83**	25.82
12	12	**-11.75**	-11.9	-11.85	**-75.54**	-74.99
5	13	**-11.53**	-11.72	-11.74	**-155.79**	-157.71
11	14	**-10.35**	-10.55	-10.55	**-116.17**	-115.87
10	15	**-9.38**	-9.34	-9.89	**163.05**	162.59
6	16	**-9.84**	-9.77	-10.52	**-76.25**	-73.7

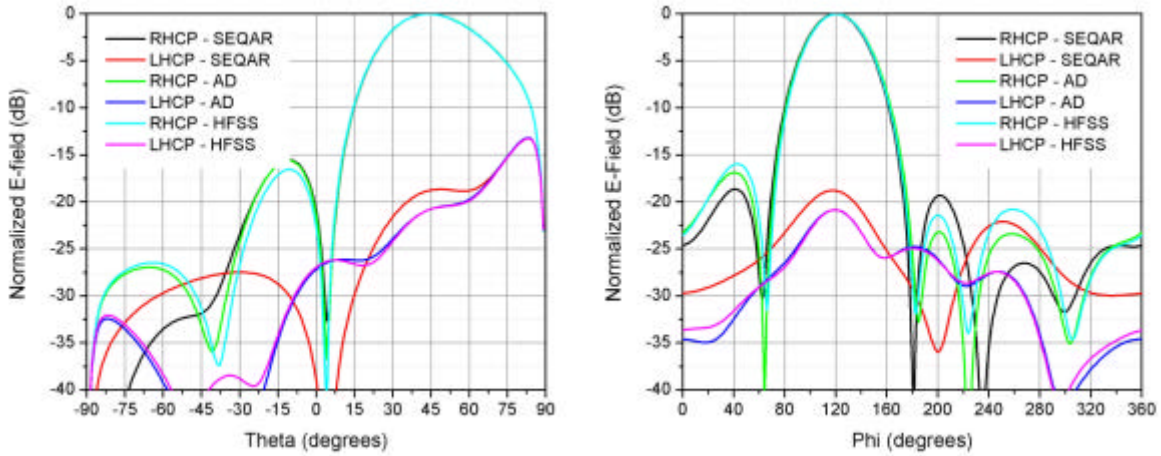

(a) (b)

Fig. 4.33. Comparison between the radiation characteristics obtained with SEQAR and those obtained using the output powers of the divider simulations in Designer and HFSS on the simplified array model for the θ=44° ϕ=120° @ 1.19 GHz case. ϕ = 120° (a) and (b) θ = 44° cuts.

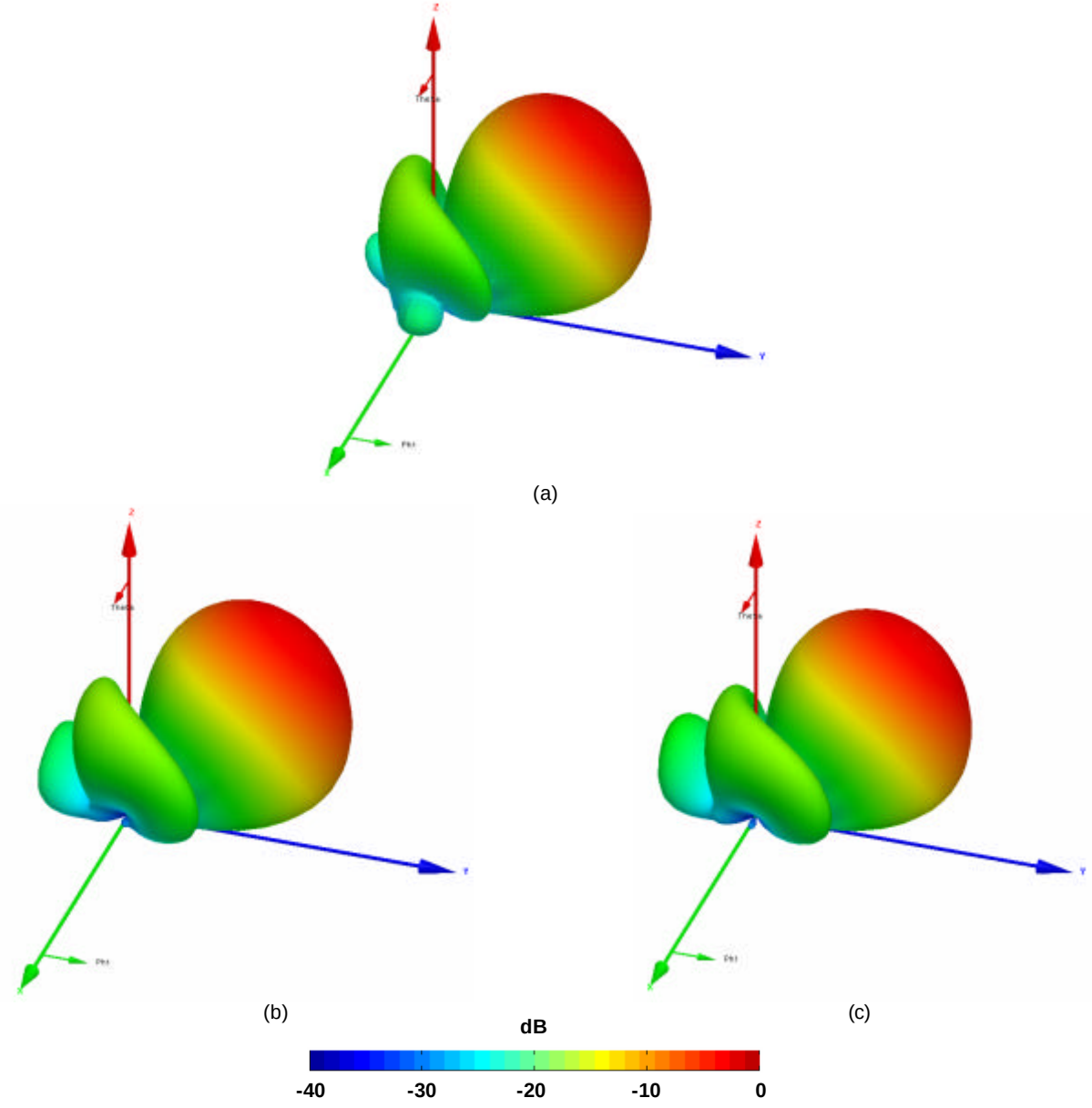

(a)

(b) (c)

Fig. 4.34. Comparison between the 3D radiation patterns for the SEQAR case (a), Designer (b), and HFSS (c) simulations for the θ=44° ϕ=120° @ 1.19 GHz case.

Case E: q=44° f=45° @ 1.27 GHz, SLL = -20 dB

This case shows some changes in the shape of the radiation patterns. The Designer and HFSS models for this case are presented in Fig. 4.35 and 4.36 respectively. Table 4.6 presents the comparison between the SEQAR case and the Designer and HFSS simulated results. The radiation patterns in Fig. 4.37 and 4.38 show that in some regions the simulation cases have better performance in terms of side lobe level suppression but in some others this performance is degraded in 5 dB or more. In the case of cross polarization the reference case is followed with more precision.

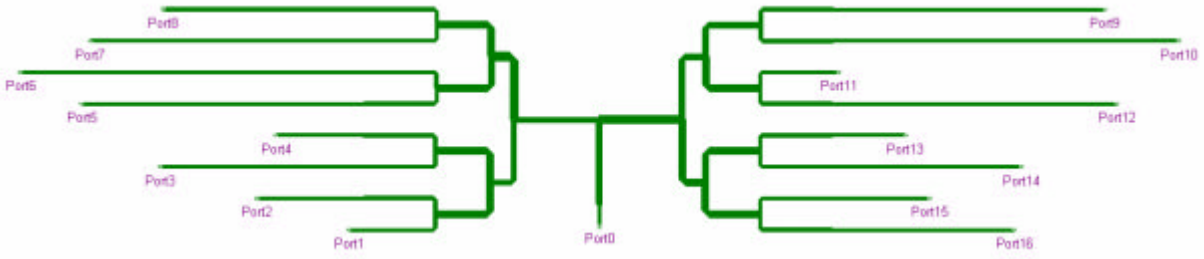

Fig. 4.35. Designer model of the θ=44° ϕ=45° @ 1.27 GHz divider.

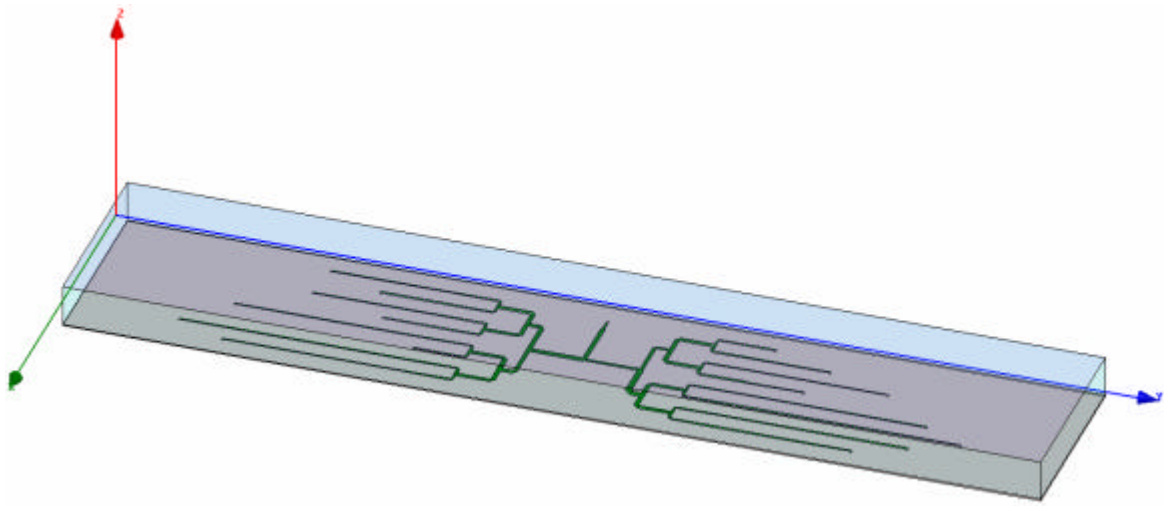

Fig. 4.36. HFSS model of the θ=44° ϕ=45° @ 1.27 GHz divider.

Table 4.6. Result comparison between the ideal case and simulations for the θ=44° ϕ=45° @ 1.27 GHz case.

Divider @ 1.27 GHz - High Scan Angle						
Identifier		**Amplitudes**			**Normalized phases**	
		Ideal	**Designer**	**HFSS**	**Ideal**	**Simulated**
Antenna port	Divider port	Relative level dB	Obtained dB	Obtained dB	Phase (°)	Phase (°)
16	1	**-16.90**	-17.15	-16.72	**0**	0
4	2	**-15.80**	-15.79	-15.97	**-96.7**	-98.19
1	3	**-16.69**	-17.07	-16.63	**165.62**	163.18
13	4	**-15.65**	-15.64	-15.81	**-76.56**	-79.26
12	5	**-13.22**	-13.26	-13.61	**85.43**	82.96
9	6	**-13.04**	-13.3	-13.19	**22.15**	19.94
5	7	**-13.04**	-13.11	-13.28	**93.35**	88.86
8	8	**-12.26**	-12.45	-12.26	**167.84**	166.14
2	9	**-12.26**	-12.12	-12.59	**97.37**	94.3
6	10	**-11.73**	-11.8	-11.87	**19.13**	16.55
3	11	**-11.43**	-11.48	-11.42	**11.22**	10.07
15	12	**-10.77**	-10.64	-11.09	**83.32**	80.75
10	13	**-10.48**	-10.35	-10.76	**-57.19**	-59.14
14	14	**-10.58**	-10.65	-10.62	**-176.34**	-178.91
7	15	**-10.12**	-9.93	-10.32	**-82.39**	-83.85
11	16	**-10.12**	-10.19	-10.16	**-169.88**	-170.61

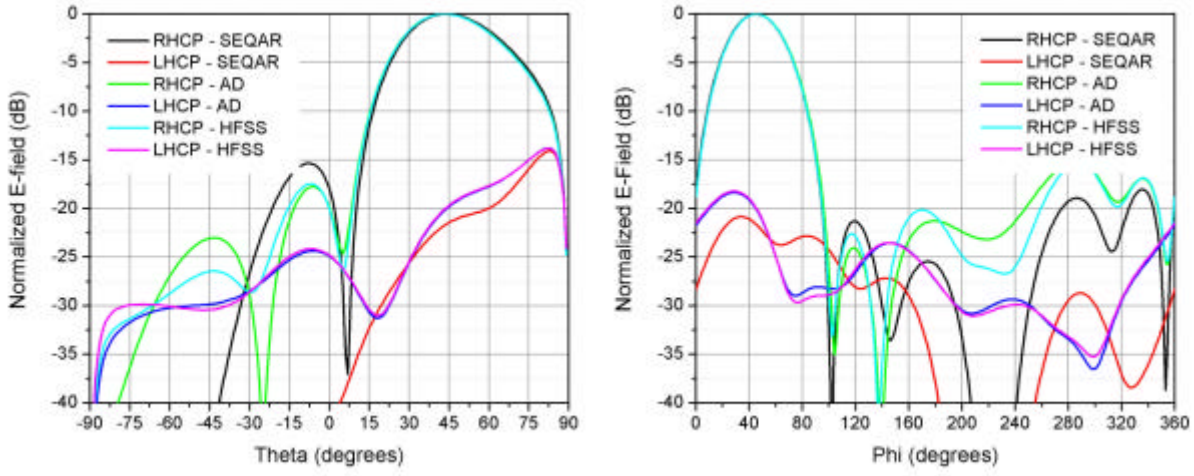

(a) (b)

Fig. 4.37. Comparison between the radiation characteristics obtained with SEQAR and those obtained using the output powers of the divider simulations in Designer and HFSS on the simplified array model for the θ=44° ϕ=45° @ 1.27 GHz case. ϕ = 45° (a) and (b) θ = 44° cuts.

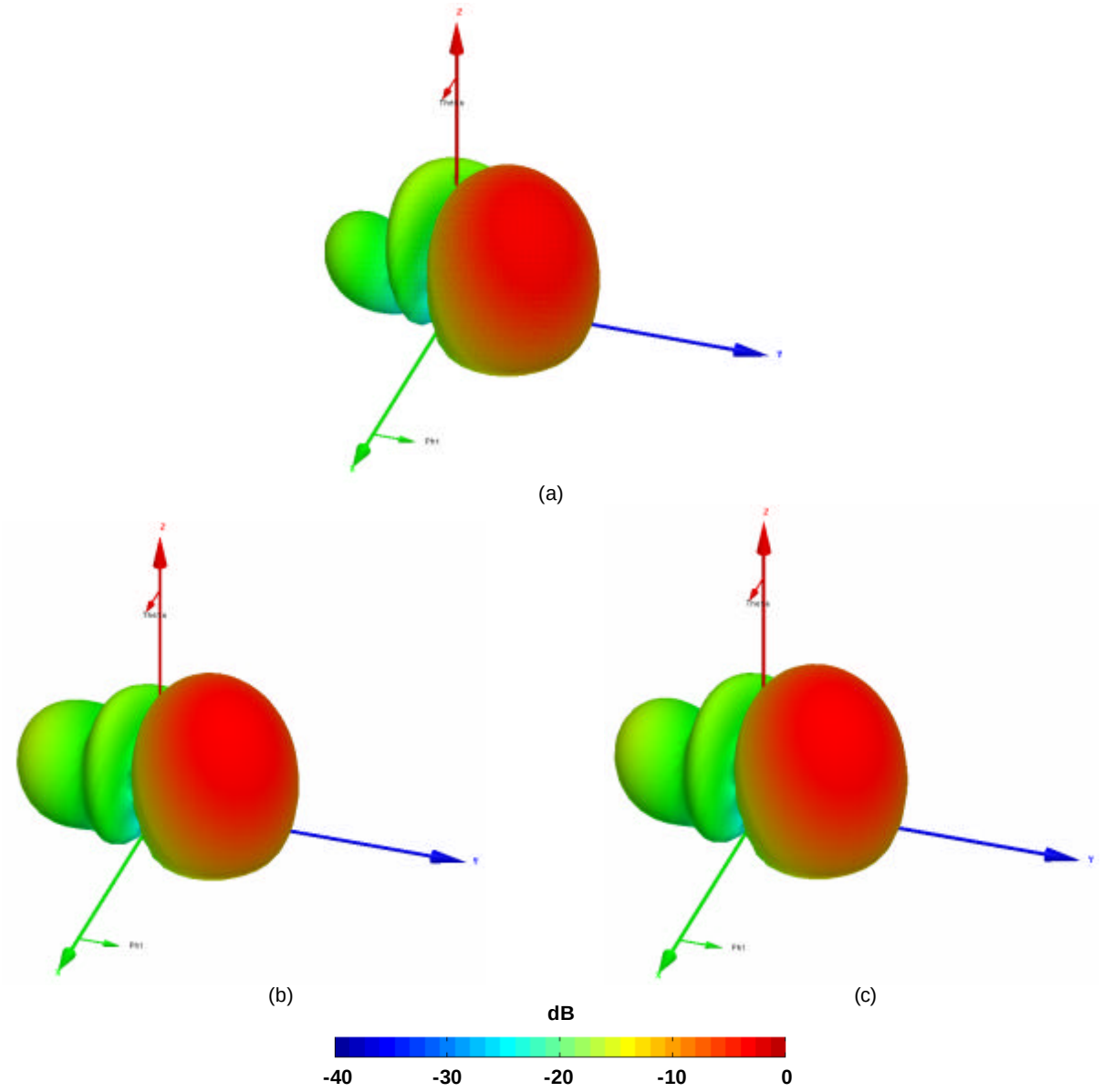

Fig. 4.38. Comparison between the 3D radiation patterns for the SEQAR case (a), Designer (b), and HFSS (c) simulations for the θ=44° ϕ=45° @ 1.27 GHz case.

Case F: q=48° f=290° @ 1.57 GHz, SLL = -20 dB

This case is where the difference between the simulation results for Designer and HFSS is the biggest. The Designer and HFSS models for this case are presented in Fig. 4.39 and 4.40 respectively. Table 4.7 presents the comparison between the SEQAR case and the Designer and HFSS simulated results. The radiation patterns in Fig. 4.41 and 4.42 show that the simulations on Designer and HFSS move in different directions from the reference case. In some regions one is has better performance and the other has poorer performance when compared to the reference and for some other region the opposite is valid. The reason for this discrepancy is to be found experimentally.

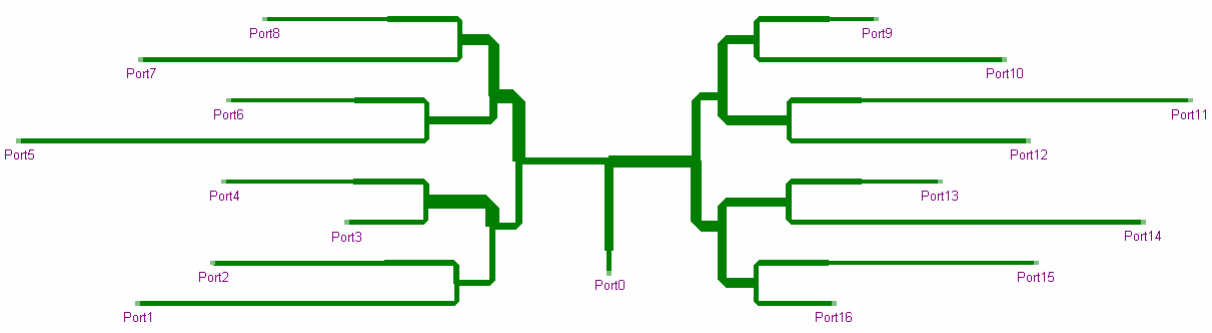

Fig. 4.39. Designer model of the θ=48° ϕ=290° @ 1.57 GHz divider.

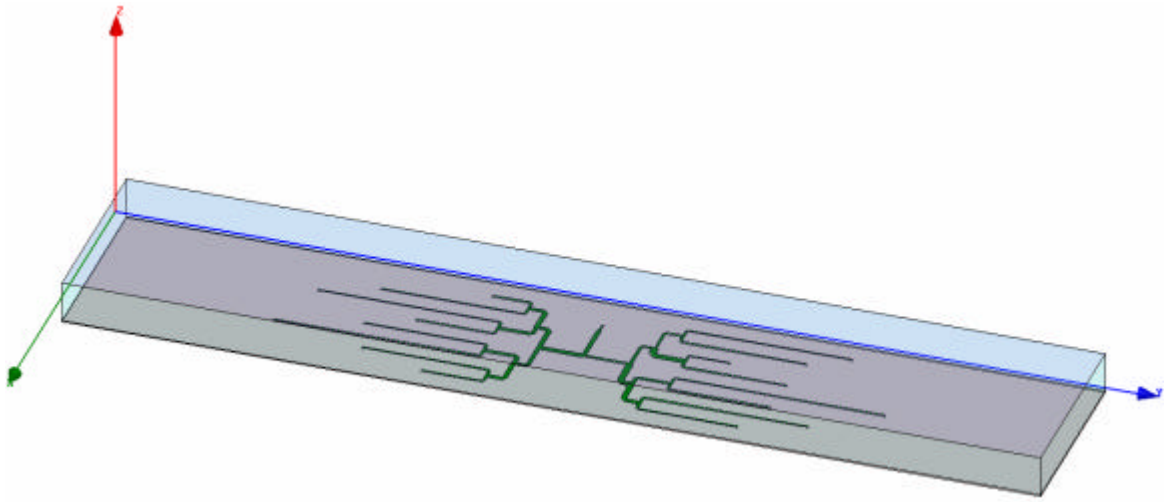

Fig. 4.40. HFSS model of the θ=48° ϕ=290° @ 1.57 GHz divider.

Table 4.7. Result comparison between the ideal case and simulations for the θ=48° ϕ=290° @ 1.57 GHz case.

Divider @ 1.57 GHz - High Scan Angle						
Identifier		**Amplitudes**			**Normalized phases**	
		Ideal	**Designer**	**HFSS**	**Ideal**	**Simulated**
Antenna port	Divider port	Relative level dB	Obtained dB	Obtained dB	Phase (°)	Phase (°)
13	1	**-22.18**	-22.52	-21.75	**0**	0
16	2	**-21.51**	-21.95	-20.43	**72.8**	72.41
1	3	**-16.53**	-16.89	-16.04	**-123.29**	-120.49
4	4	**-15.19**	-15.34	-14.87	**115.96**	117.09
3	5	**-14.05**	-14.28	-14.14	**-83.55**	-82.15
2	6	**-14.28**	-14.49	-14.4	**121.4**	123.5
15	7	**-12.11**	-12.15	-12.12	**3.92**	5.82
14	8	**-12.11**	-12.1	-12.02	**124.84**	125.23
7	9	**-11.70**	-11.5	-11.94	**-162.27**	-160.38
9	10	**-11.27**	-11.23	-11.35	**72.05**	71.76
8	11	**-11.09**	-11.03	-11.56	**-78.05**	-77.29
12	12	**-11.21**	-11.25	-11.45	**80.03**	81.79
5	13	**-10.27**	-10.29	-10.46	**166.98**	169.9
11	14	**-10.18**	-10.23	-10.53	**-32.01**	-32.5
10	15	**-10.09**	-9.82	-10.65	**41.96**	43.72
6	16	**-9.96**	-9.68	-10.43	**-120.24**	-118.28

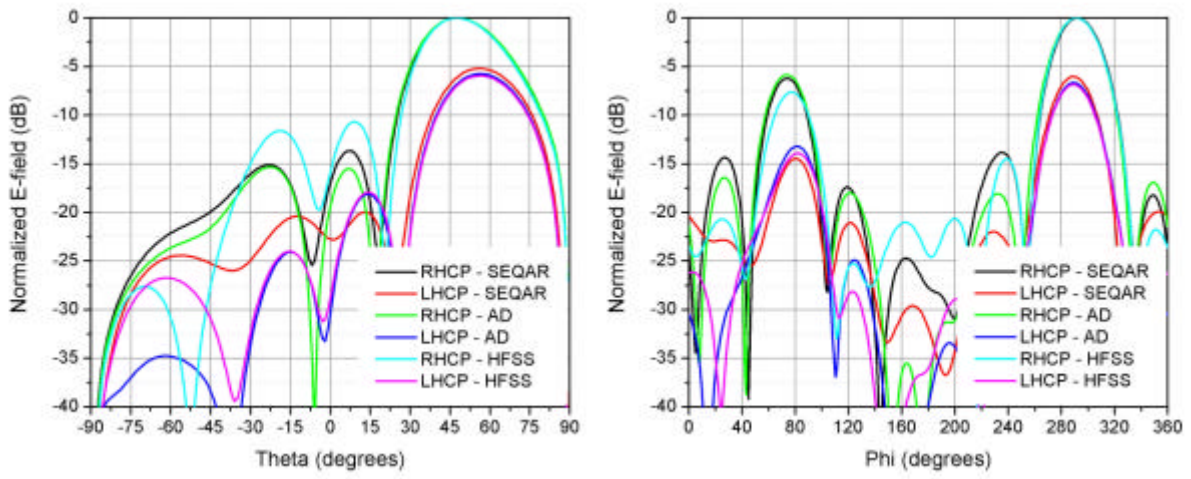

(a) (b)

Fig. 4.41. Comparison between the radiation characteristics obtained with SEQAR and those obtained using the output powers of the divider simulations in Designer and HFSS on the simplified array model for the θ=48° ϕ=290° @ 1.57 GHz case. ϕ = 290° (a) and (b) θ = 48° cuts.

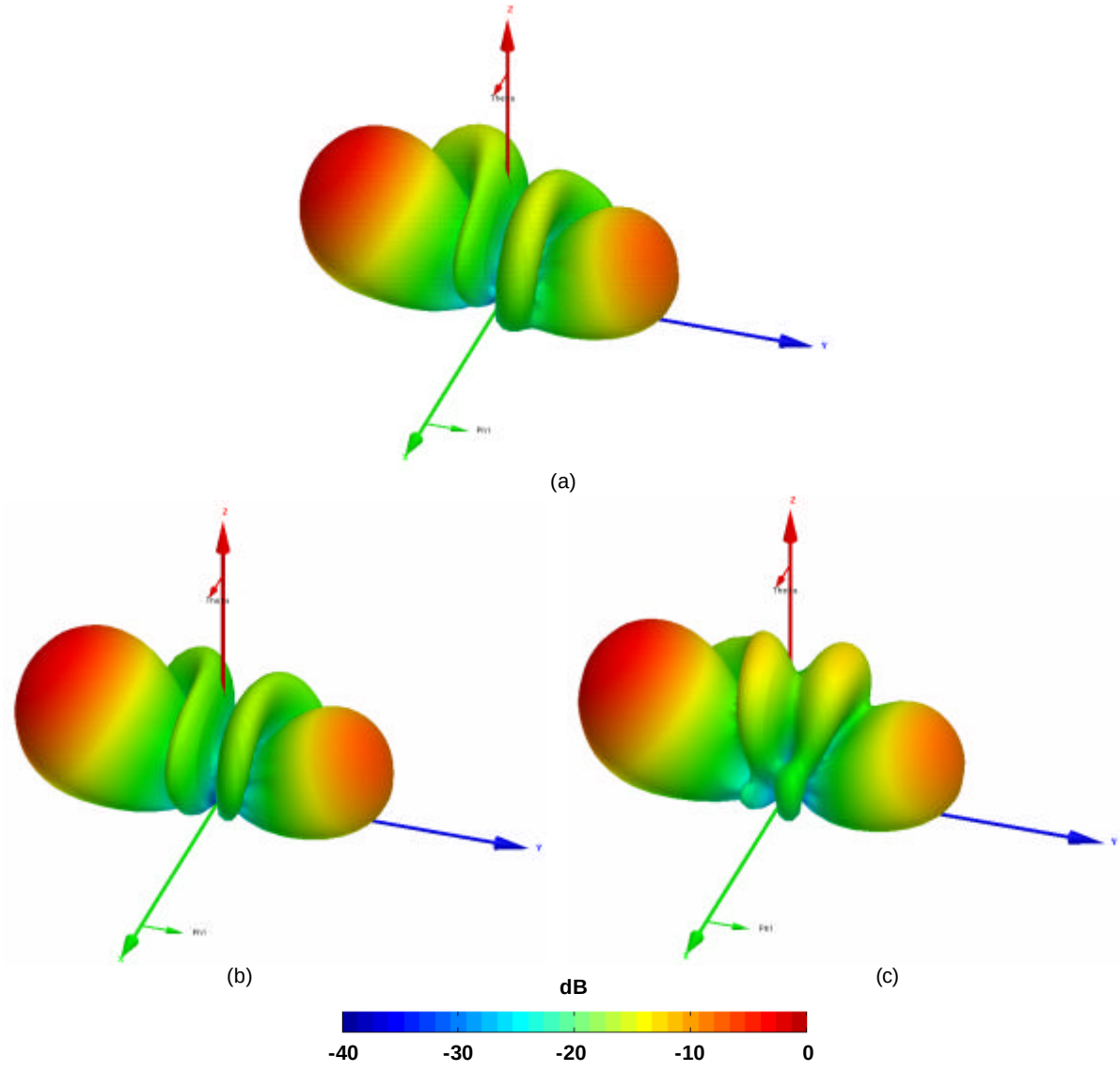

(a)

(b) (c)

Fig. 4.42. Comparison between the 3D radiation patterns for the SEQAR case (a), Designer (b), and HFSS (c) simulations for the θ=48° ϕ=290° @ 1.57 GHz case.

4.5.1.1 Remarks on the comparison of simulation and reference cases

Through the comparison of the simulation and the reference or 'ideal' case it was shown that there are small discrepancies between the results of the different tools used to analyze them. The main reason for the differences between the Designer and the HFSS models is the fact that Designer considers an infinitely large ground plane and substrate while HFSS is able to truncate it to its actual size, at the expense of a much longer computing time. Therefore, the results obtained with HFSS can be considered more precise. The SMA connectors were not simulated as this was not possible with the computational power available. These connectors have an effect on performance and the way to evaluate their effect is by measuring the physical structure. The fabrication and measurement details are presented in the next section.

4.6 Beamforming power divider construction

On the previous sections the process of designing the beamforming power dividers and the simulation results were presented. This section gives a brief description of the construction process as this step hasn't been completed yet.

As mentioned in previous sections, the beamforming power dividers should fit in a rectangular box 480 mm long and 100 mm wide (see Fig. 4.2). It was also mentioned that the actual effective area is reduced to account for the width of the box walls. The dimensions of the box match exactly the size of the metallic box used in HFSS, therefore the simulations of the dividers done with this tool are expected to be more precise than those done with Designer. The dimensions of the box are shown in a detailed sectional cut in Fig. 4.43 below.

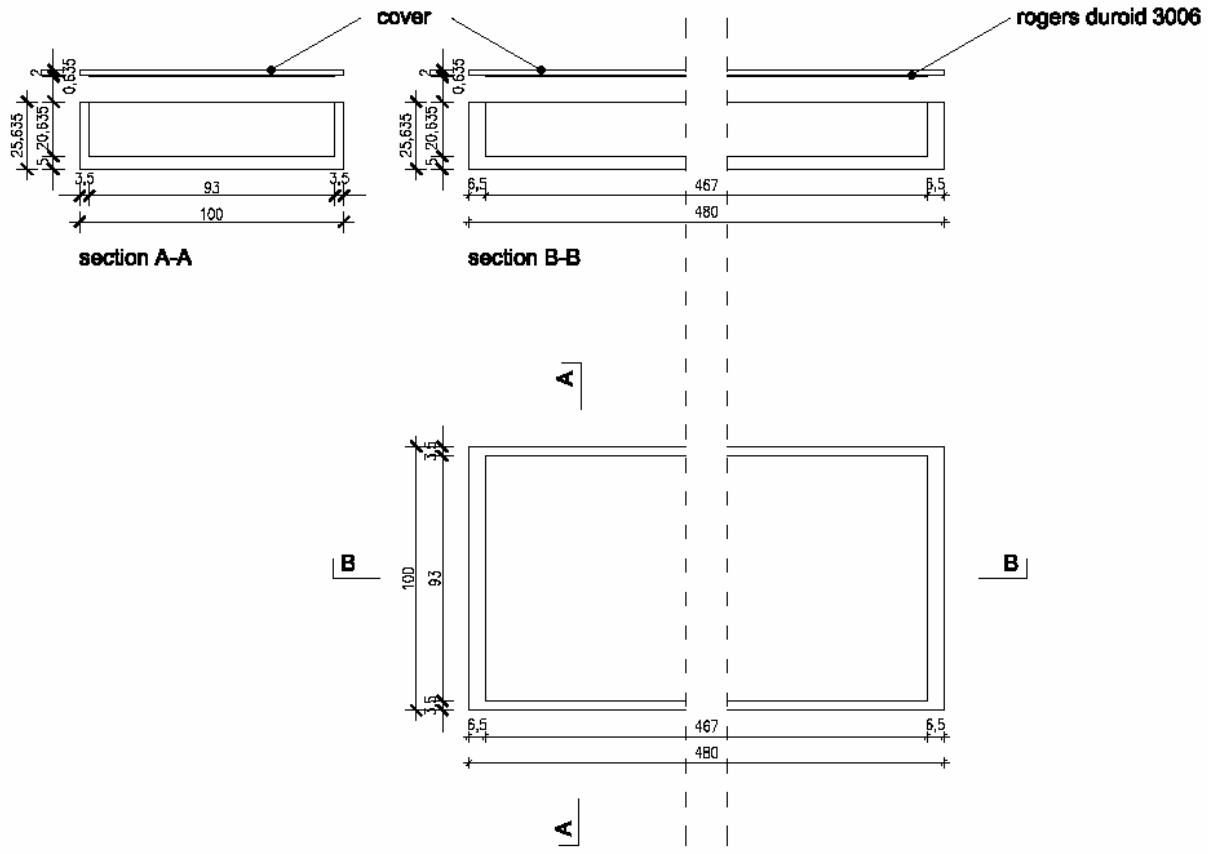

Fig. 4.43. Sectional cuts of the metallic box containing the power dividers.

An example of the substrate with the etched power divider is shown in Fig 4.44. The power divider will be placed just below the metallic cover with the etched surface facing down. Holes will be made in the

top cover to fix the connectors with screws and to solder the probe to the output ports of the divider underneath.

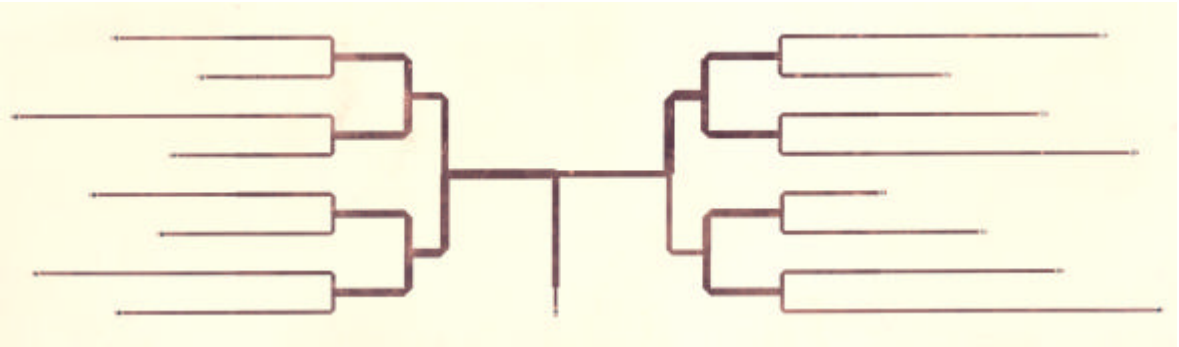

Fig. 4.44. One of the dividers etched in the Rogers Duroid 3006 substrate.

The construction of the boxes, the drilling of holes and the soldering of the connectors is in progress at the mechanical workshops of DLR, thus no more details about it are available.

Chapter 5 – Conclusions and future work

The analysis of the beamforming capabilities of the Galileo antenna array and the design of a series of passive power dividers for testing the beamforming capabilities of the array were presented in this work. Useful information about the Galileo antenna array was gathered and the simulation results of the power dividers show a good performance; therefore, good results are expected on the measurement when their fabrication is completed.

The process followed to achieve the results was a logic sequence as presented in this report. First a review of the microstrip antenna, passive microwave circuit, and phased array theory was performed. In parallel, some time was used to get familiar with the simulation tools used in this project: Ansoft Designer® and HFSS®. Once this stage was over, a series of tests to understand the principles of beamforming were performed with linear and planar arrays using a simple probe-fed square patch optimal at the center frequency of the Galileo band. The next step was studying in deep the characteristics of the Galileo antenna array that, as presented, was a necessary step before moving into the design of the beamforming power dividers. The result of this study phase was a good picture of the capabilities and limitations of the array. During this stage, a big amount of simulations using a simplified model of the array were performed and a conference paper with the title 'Beamforming Analysis on a Broadband Antenna Array for the Galileo System', presented in Appendix B, was written as a result. The mentioned paper was accepted and will be presented at the 2006 IEEE international symposium on Antennas and Propagation in Albuquerque New Mexico on July 2006.

The next step was designing the power divider networks. The main contributions during this stage were the programs created in MATLAB® to accelerate the design process as they can be used in the future for similar applications with minor changes in the code. Preliminary designs were ready by early April and were sent out for fabrication. The purpose of fabricating these tests was to have a measurement reference, along with the simulation results, to further optimize the designs by implementing a series of compensations in the MATLAB program for the losses due to different transmission line lengths at the output of the dividers. Unfortunately, due to administrative problems it was not possible to have these tests manufactured and further optimize or implement the compensations.

The status of the project at the moment this is written is that due to a large work backlog in the different workshops at DLR, the fabrication of the dividers and the Galileo antenna array is still unfinished. It is expected to have this stage completed in the next weeks and then have the opportunity to measure both.

Future work includes the conclusion of the fabrication stage and measurement of the S-parameters of the beamforming power dividers. If the measurement results do not agree with the simulations, further optimization of the designs has to be performed. One way of doing this is by implementing compensations for the losses due to different transmission line lengths at the divider outputs in the MATLAB program used to design them. If the divider measurements are satisfactory, measurements using them in the Galileo antenna array have to be performed to evaluate the performance of the physical implementation of the array and compare it with the expected behavior. This information can be then used for the design of the digital signal processing module that will be used for beamforming in the final design

Final words

This project was very rewarding in the professional and personal aspects as it gave me the possibility to participate in an innovative project related to the Galileo navigation technology that will be part of our lives in the near future. There were naturally positive and negative situations and things that could have been done in a different way; however the positive aspects surpass the negative ones greatly.

Thanks again to everyone that made this possible and very special thanks to you that took the time to read this master thesis.

References

[1] C.A. Balanis, *Antenna Theory Analysis and Design*. 2nd edition. USA: John Wiley & Sons, 1997.

[2] L. C. Godara, "Applications of antenna arrays to mobile communications, part I: performance improvement, feasibility, and system considerations," *Proceedings of the IEEE*, vol. 85. pp. 1031-1060, July 1997.

[3] R.C. Hansen, *Microwave Scanning Antennas*. Volume 2. USA: Academic Press, 1966.

[4] R. J. Mailloux, *Phased Array Antenna Handbook*. USA: Artech House, 1994.

[5] N. Fourikis, *Phased Array-Based Systems and Applications*. USA: John Wiley & Sons, 1997.

[6] E. S. Neves, A. Dreher, and P. De Vita, "Smart antenna array for Galileo and GPS applications," *2nd ESA Workshop on Satellite Navigation User Equipment Technologies*, Noordwijk, The Netherlands, 8 pages on CD-ROM, Dec. 2004.

[7] E. S. Neves, A. Dreher, and P. De Vita, "Modular smart antenna array for GPS and Galileo Applications," *The European Navigation Conference ENC-GNSS*, Munich, Germany, 12 pages on CD-ROM, Jul. 2005.

[8] M. Clergeaud, M. Thiel, "Algorithms for beamforming and beamsteering of adaptive antennas for satellite communications and navigation". Internal Report, DLR-IB 554-04/01, DLR, Germany, 2003.

[9] D. C. M. Maciel, "Circularly polarized microstrip antenna arrays," *M.S. thesis,* Instituto Tecnológico de Aeronáutica, Brazil, 2005. (*in Portuguese*)

[10] M. Thiel and A. Dreher, "Sequential rotation in a smart antenna terminal for broadband communication," *IEEE Antennas Propagat. Soc. Int. Symp. Dig.,* Monterey, CA, June 2004.

[11] F.-I Tseng and D.K Cheng, "Optimum scannable planar arrays with an invariant sidelobe level," *Proceedings of the IEEE*, vol. 56, no. 11, pp. 1771-177, Nov. 1968.

[12] I.S. Reed, J.D. Mallet, and L.E. Brennan, "Rapid convergence rate in adaptive arrays," *IEEE Transactions on AES*, vol 10, pp. 853-863, Nov. 1974.

[13] E. Wilkinson, "An N-way hybrid power divider," *IEEE Transactions*, vol. 8. pp. 116-118, Jan. 1960.

[14] R. E. Collin, *Foundations for Microwave Engineering*. 2nd edition. USA: McGraw-Hill, 1992.

[15] D.M. Pozar, *Microwave Engineering*. 3rd edition. USA: John Wiley & Sons, 2004.

[16] T.C. Edwards, *Foundations for Microstrip Circuit Design*. UK: John Wiley & Sons, 1981.

[17] P. Silvester and P. Benedek, "Microstrip discontinuity capacitances for right-angle bends, T-junctions, and crossings," *IEEE Transactions on Microwave Theory and Techniques*, vol. MTT-21, no. 5, pp. 341-346, May 1973.

Appendix A – MATLAB program for beamforming power divider design

```
%%%%%%%%% Power divider calculator for beamforming networks %%%%%%%%%%
%
% This program calculates the line lenghts and impedances for power
% dividers to be used in beamforming networks given the required output phases and
% amplitudes.
%
%
% Created by Arturo Arango Selga on February 2006
%
%%%%%%%%%%%%%%%%%%%%%%%%%%%%%%%%%%%%%%%%%%%%%%%%%%%%%%%%%%%%%%%%%%%%%%%%%%%%%%%


clear all;


                                %%%%% variable value input %%%%%

Dimension = 4;                          % Matrix dimension
Zin = 50;                               % Input impedance
Zout = 50;                              % Output impedance
Zbase = 30;                             % Base impedance for intermediate transformers
Efficiency = 0.95;                      % Structure efficiency, used to obtain the theoretical
output relative levels for a a given efficiency
L50 = 111.7;                            % Lenght of a 50 Ohm line at the design frequency



%%%%% Load amplitude matrix %%%%%

%amplitudes = ones(Dimension)           % when there is a uniform distribution, choose this
option for a ones matrix
                                        %
amplitudes = [                          % else write the matrix with the coefficients for each
element in the desired order
     0.21    0.27    0.22    0.28
     0.49    0.51    0.51    0.61
     0.61    0.69    0.74    0.86
     0.92    0.90    1.00    1.00
];



%%%% Load phase matrix %%%%

%line phases = zeros(Dimension)                 % When a broadside array is desired
                                                %
line_phases = [                                 % else write the phases for each of the lines
in the amplitude matrix in the same order
    166.43      69.73       -27.95      89.87
    -108.14     -171.42     -100.22     -25.73
    -96.2       -174.44     177.65      -110.25
    109.24      -9.91       84.04       -3.45
];



                                %%%%% Amplitude calculations %%%%%


%%%%% Normalization %%%%%

Level1 = sum(sum(amplitudes))

Normalization = Efficiency/Level1;

Level5b= Normalization*amplitudes

Level4b= [
    (Level5b(1,1)+Level5b(1,2))   (Level5b(1,3)+Level5b(1,4))   (Level5b(2,1)+Level5b(2,2))
(Level5b(2,3)+Level5b(2,4))
    (Level5b(3,1)+Level5b(3,2))   (Level5b(3,3)+Level5b(3,4))   (Level5b(4,1)+Level5b(4,2))
(Level5b(4,3)+Level5b(4,4))
     ]

Level3b= [
    (Level4b(1,1)+Level4b(1,2))   (Level4b(1,3)+Level4b(1,4))
    (Level4b(2,1)+Level4b(2,2))   (Level4b(2,3)+Level4b(2,4))
    ]
```

```
Level2b= [
    (Level3b(1,1)+Level3b(1,2))   (Level3b(2,1)+Level3b(2,2))
    ]

Level1b= [
    (Level2b(1,1)+Level2b(1,2))
    ]


%%%%% Divider impedances %%%%%

% Level 5
K51 = Level5b(1,1)/Level5b(1,2);
K52 = Level5b(1,3)/Level5b(1,4);
K53 = Level5b(2,1)/Level5b(2,2);
K54 = Level5b(2,3)/Level5b(2,4);

K55 = Level5b(3,1)/Level5b(3,2);
K56 = Level5b(3,3)/Level5b(3,4);
K57 = Level5b(4,1)/Level5b(4,2);
K58 = Level5b(4,3)/Level5b(4,4);

Z3_51 = Zbase*sqrt(sqrt(K51)*(1+K51));
Z2_51 = Zbase*sqrt((1+K51)/(sqrt(K51))^3);
Z3_52 = Zbase*sqrt(sqrt(K52)*(1+K52));
Z2_52 = Zbase*sqrt((1+K52)/(sqrt(K52))^3);

Z3_53 = Zbase*sqrt(sqrt(K53)*(1+K53));
Z2_53 = Zbase*sqrt((1+K53)/(sqrt(K53))^3);
Z3_54 = Zbase*sqrt(sqrt(K54)*(1+K54));
Z2_54 = Zbase*sqrt((1+K54)/(sqrt(K54))^3);

Z3_55 = Zbase*sqrt(sqrt(K55)*(1+K55));
Z2_55 = Zbase*sqrt((1+K55)/(sqrt(K55))^3);
Z3_56 = Zbase*sqrt(sqrt(K56)*(1+K56));
Z2_56 = Zbase*sqrt((1+K56)/(sqrt(K56))^3);

Z3_57 = Zbase*sqrt(sqrt(K57)*(1+K57));
Z2_57 = Zbase*sqrt((1+K57)/(sqrt(K57))^3);
Z3_58 = Zbase*sqrt(sqrt(K58)*(1+K58));
Z2_58 = Zbase*sqrt((1+K58)/(sqrt(K58))^3);

%Transformer Level4 --> Level5

T2_51 = sqrt(Z2_51*Zout);
T3_51 = sqrt(Z3_51*Zout);
T2_52 = sqrt(Z2_52*Zout);
T3_52 = sqrt(Z3_52*Zout);

T2_53 = sqrt(Z2_53*Zout);
T3_53 = sqrt(Z3_53*Zout);
T2_54 = sqrt(Z2_54*Zout);
T3_54 = sqrt(Z3_54*Zout);

T2_55 = sqrt(Z2_55*Zout);
T3_55 = sqrt(Z3_55*Zout);
T2_56 = sqrt(Z2_56*Zout);
T3_56 = sqrt(Z3_56*Zout);

T2_57 = sqrt(Z2_57*Zout);
T3_57 = sqrt(Z3_57*Zout);
T2_58 = sqrt(Z2_58*Zout);
T3_58 = sqrt(Z3_58*Zout);

TL5 = [
    T2_51       T3_51       T2_52       T3_52       T2_53       T3_53       T2_54       T3_54
    T2_55       T3_55       T2_56       T3_56       T2_57       T3_57       T2_58       T3_58
]

% Level 4
K41 = Level4b(1,1)/Level4b(1,2);
K42 = Level4b(1,3)/Level4b(1,4);
K43 = Level4b(2,1)/Level4b(2,2);
K44 = Level4b(2,3)/Level4b(2,4);

Z3_41 = Zbase*sqrt(sqrt(K41)*(1+K41));
Z2_41 = Zbase*sqrt((1+K41)/(sqrt(K41))^3);

Z3_42 = Zbase*sqrt(sqrt(K42)*(1+K42));
Z2_42 = Zbase*sqrt((1+K42)/(sqrt(K42))^3);

Z3_43 = Zbase*sqrt(sqrt(K43)*(1+K43));
Z2_43 = Zbase*sqrt((1+K43)/(sqrt(K43))^3);

Z3_44 = Zbase*sqrt(sqrt(K44)*(1+K44));
Z2_44 = Zbase*sqrt((1+K44)/(sqrt(K44))^3);
```

```
%Transformer Level3 --> Level4

T2_41 = sqrt(Z2_41*parallel(Z2_51,Z3_51));
T3_41 = sqrt(Z3_41*parallel(Z2_52,Z3_52));
T2_42 = sqrt(Z2_42*parallel(Z2_53,Z3_53));
T3_42 = sqrt(Z3_42*parallel(Z2_54,Z3_54));

T2_43 = sqrt(Z2_43*parallel(Z2_55,Z3_55));
T3_43 = sqrt(Z3_43*parallel(Z2_56,Z3_56));
T2_44 = sqrt(Z2_44*parallel(Z2_57,Z3_57));
T3_44 = sqrt(Z3_44*parallel(Z2_58,Z3_58));

TL4 = [
    T2_41       T3_41       T2_42       T3_42
    T2_43       T3_43       T2_44       T3_44
]

%Level 3

K31 = Level3b(1,1)/Level3b(1,2);
K32 = Level3b(2,1)/Level3b(2,2);

Z3_31 = Zbase*sqrt(sqrt(K31)*(1+K31));
Z2_31 = Zbase*sqrt((1+K31)/(sqrt(K31))^3);
Z3_32 = Zbase*sqrt(sqrt(K32)*(1+K32));
Z2_32 = Zbase*sqrt((1+K32)/(sqrt(K32))^3);

%Transformer Level2 --> Level3

T2_31 = sqrt(Z2_31*parallel(Z2_41,Z3_41));
T3_31 = sqrt(Z3_31*parallel(Z2_42,Z3_42));
T2_32 = sqrt(Z2_32*parallel(Z2_43,Z3_43));
T3_32 = sqrt(Z3_32*parallel(Z2_44,Z3_44));

TL3 = [
    T2_31       T3_31
    T2_32       T3_32
]

%Level 2

K2 = Level2b(1,1)/Level2b(1,2);

Z3_2 = Zbase*sqrt(sqrt(K2)*(1+K2));
Z2_2 = Zbase*sqrt((1+K2)/(sqrt(K2))^3);

%Transformer Level1--> Level2
T21 = sqrt(Z2_2*parallel(Z2_31,Z3_31));
T22 = sqrt(Z3_2*parallel(Z2_32,Z3_32));

TL2 = [
    T21
    T22
]

%Transformer Level1

TL1 = sqrt(Zin*parallel(Z2_2,Z3_2))



%%%%% Relative amplitudes for each level in dB %%%%%

relative_amplitudes_Level5b_dB = 10*log10(Level5b)
relative_amplitudes_Level4b_dB = 10*log10(Level4b)
relative_amplitudes_Level3b_dB = 10*log10(Level3b)
relative_amplitudes_Level2b_dB = 10*log10(Level2b)



                %%%%% Last segment line lenght calculations %%%%%%

reference = max(max(line_phases));                  % Reference the highest phase value

if line_phases <= 0
    difference = abs(reference) + abs(line_phases);
else
    difference = abs(reference)-line_phases;
end

 phase_shift_correction = [                    % Simulated phase shift error before adding
last segment
     -2.32  -2.31   -2.12   -2.05
     -0.09  0       -0.18   -0.23
     -2.24  -2.85   -2.62   -2.64
     -2.01  -2.67   -2.11   -1.89
 ];
```

```
corrected = difference+L50/16+phase_shift_correction;  % L50/16 segment added to avoid
negative distances when considering the phase shift correction

Deg2Rad_diff= (corrected*pi)/180;

Physical_Lenght_lines= (L50*Deg2Rad_diff)/(2*pi)
Percentage_of_50_Ohm_Lenght = Physical_Lenght_lines/L50
```

Appendix B – APS conference paper

Beamforming Analysis on a Broadband Antenna Array for the Galileo System

E. S. Neves*, M. V. T. Heckler, A. A. Selga and A. Dreher

German Aerospace Center (DLR), Institute of Communications and Navigation, Oberpfaffenhofen, D-82234 Wessling, Germany

1. Introduction

Future navigation services provided by the upcoming Galileo satellite system will require corresponding improvements on the navigation receiving systems. The first part of any navigation receiving system is the antenna or antenna terminal. In order to obtain the best possible navigation accuracy, exploiting the full capabilities offered by this new system, design of state-of-the-art antenna systems must be pursuit.

In this work, beamforming analyses on a broadband antenna array designed for the whole Galileo frequency band [1], [2] are shown. The beamforming software [3] was developed by the DLR antenna group and employs a combination of an optimized Chebychev pattern [4] with the Sample Matrix Inversion (SMI) algorithm [5].

This paper begins with a description of the antenna array used for the simulations and its antenna element, and then the construction concepts are presented and commented. Finally, the results of the beamforming analyses are shown and discussed.

2. Antenna Array Setup

The single element for the Galileo antenna array [1], [2] consists of a circular microstrip patch antenna fed by means of capacitive coupling. The element has been designed with an integrated feeding system composed of a 180° hybrid (rat-race) and two 90° hybrids in order to generate a progressive phase shift of 90 degrees at the four feeding points. A schematic of the antenna element as well as a first prototype are shown in Fig. 1.

The impedance bandwidth of this element is approximately 31% (full Galileo band) in which the axial ratio is below 3 dB for elevation angles from 90° down to 30°.

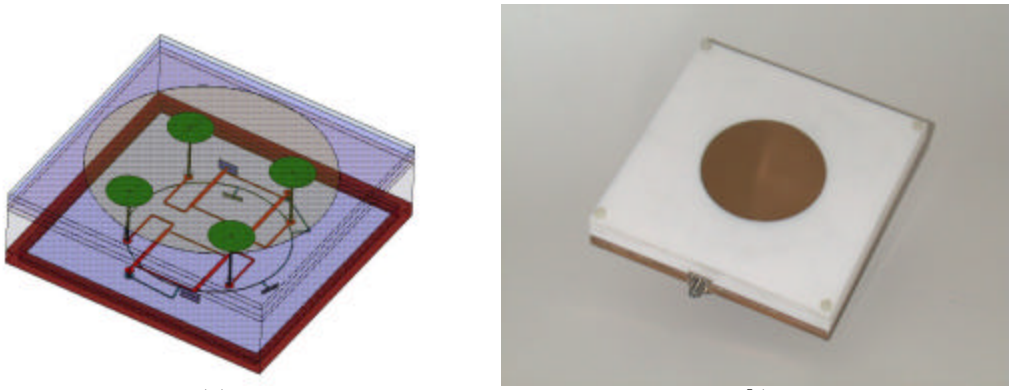

(a) (b)

Fig. 1. Single element (a) schematic and (b) prototype.

Fig. 2 shows the antenna array schematic in a perspective and a side view. The array size is 4x4 elements and it is mounted using a modular concept, i.e. each antenna element is a module itself. Based on the capabilities of a 4x4 antenna array using the element described above, a set of desired specifications was made as follows:

Table 1. Antenna array specifications

Parameter	Specification
bandwidth	1164 MHz to 1591 MHz (31%)
return loss	-10 dB min
polarization	RHCP
azimuth scanning	360°
elevation scanning	from 30° to 90° (from 0° to 30° desired)
gain	10 dBi min.over all scan angles (30° to 90° elevation)
axial ratio	3 dB min. over all scan angles (30° to 90° elevation)
cross-polarization	15 dB minimum, 25 dB or better is desirable

The overall antenna array surface is 38 cm x 38 cm, since each module measures 95 mm x 95 mm. The feeding of each element is performed by means of phase-stable coaxial cables. The adopted mechanical concept provides flexibility to the array prototype, allowing real time electronic steering as well as passive switched beamforming tests on the same platform by means of switching modules. In addition, any part of the antenna array may be easily tested isolated from the others.

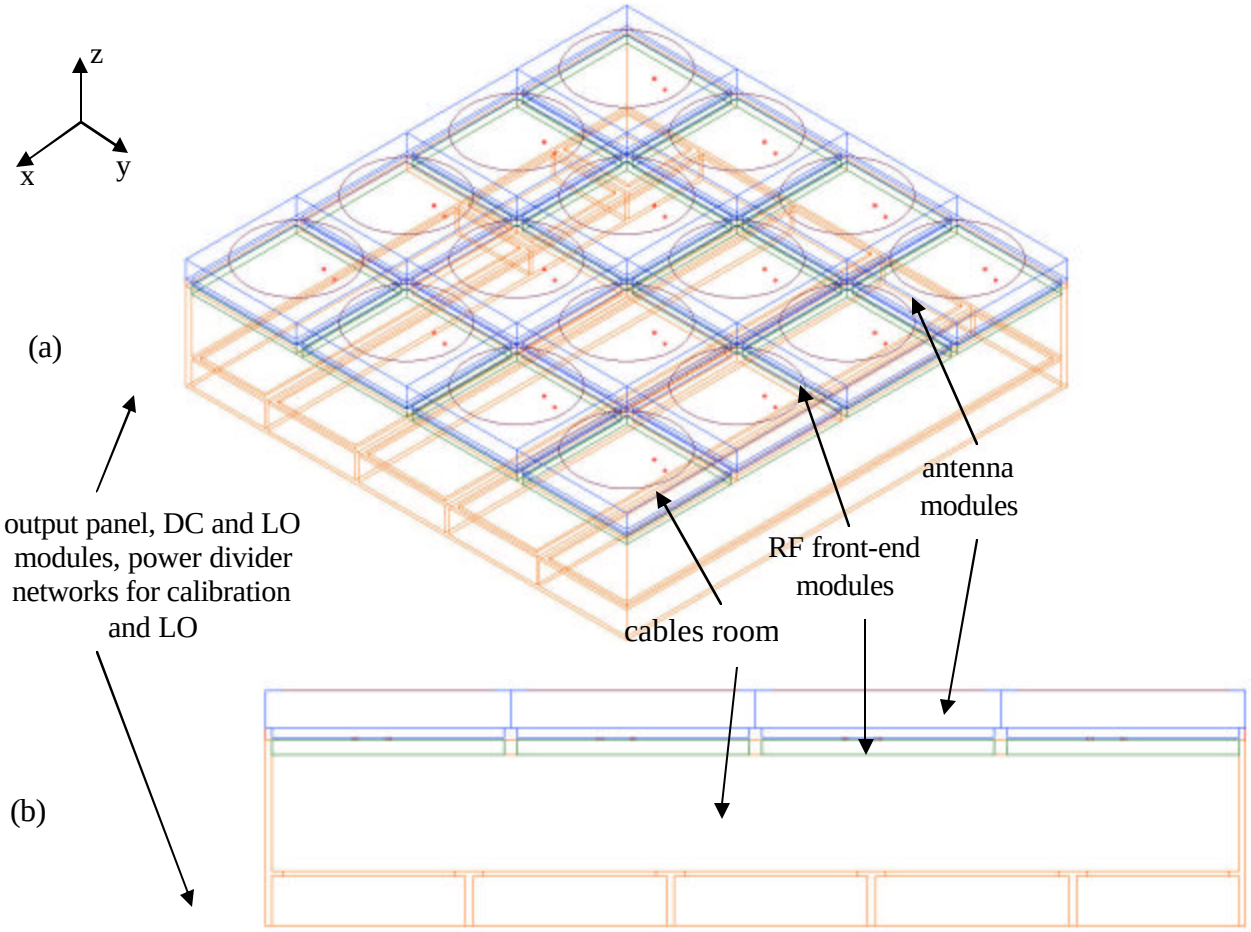

Fig. 2. Antenna array frame structure. (a) Perspective view. (b) Side view.

3. Beamforming Simulation Results

In order to verify the array performance, simulations have been carried out for different beamforming conditions and frequencies. The computations have been performed using a simplified model of the antenna to suit the available computational resources. It did not consider the feeding system under each array element (180° and 90° hybrids). Therefore, the vias feeding the four plates shown in Fig. 1(a) have been directly fed with the appropriate amplitudes and phases.

Beamforming simulations including mutual coupling have been performed. For this purpose, the radiation characteristics for each array element were determined using the Planar EM Simulator from Ansoft Designer®. A decoupling algorithm was applied according to the procedure described in [3]. The dielectric layers and ground plane were considered infinite in extension. Further details related to these simulations will be given at the symposium.

Since the array is designed to operate at the entire Galileo band, computations have been performed for frequencies located at the lower and upper parts of it. The first observable effect when working with a broad band is that the directivity, as well as the side lobe level (SLL) related to the main lobe, may vary significantly from the lower to the upper frequencies. For instance, when pointing the main beam to broadside and without applying any SLL suppression, a directivity of 15.65 dBi is observed at 1.19 GHz in contrast with 17.98 dBi at 1.57 GHz. One reason for that is the electrical inter-element spacing, which is 0.38 λ_0 for the first and 0.5 λ_0 for the second frequency respectively. Moreover, the simulated gain for an isolated element in the boresight decreases from the upper to the lower part of the frequency band.

Simulations pointing the main beam to an azimuth angle of 45° and different elevation angles with SLL suppression of 20 dB were performed. With this setup, the main beam could only be steered down to an elevation angle of 47.5° at 1.19 GHz due to the physical characteristics of the array. The calculated directivity in this case was 14.09 dBi. All lobe levels are 20 dB under the main beam, as shown in Fig. 3. Under these conditions, the directivity at an elevation of 30°, the minimum acceptable according to the specifications, is estimated to be 12.12 dBi. At 1.57 GHz, the main beam could be steered down to an elevation angle of 40° with a directivity of 15.99 dBi considering the same SLL suppression and azimuth angle as in the former case. However, two lobes appear with levels greater than –20 dB, as it can be seen in Fig. 4.

The ratio between the E_{right} and E_{left} components, observed in Fig. 3 and Fig. 4, shows a reasonably good axial ratio, below 5 dB, for elevation angles down to 30°.

4. Conclusions

Beamforming simulations for a broadband antenna array have been presented in this work. The results showed that the radiation characteristics, especially in terms of directivity and grating lobes excitation, may present significant variations within a broad frequency band demanding careful array design.

Grating lobe excitation occurred in both frequencies simulated. In the 1.19 GHz case, the side lobe levels are all below 20 dB the main lobe. However, for other simulated beamforming conditions where the electrical inter-element spacing is bigger, lobes with higher levels have been excited.

Finally, a reasonable performance in terms of axial ratio was achieved.

References

[1] E. S. Neves, A. Dreher, and P. De Vita, "Smart antenna array for Galileo and GPS applications," *2nd ESA Workshop on Satellite Navigation User Equipment Technologies*, Noordwijk, The Netherlands, 8 pages on CD-ROM, Dec. 2004.

[2] E. S. Neves, P. De Vita, and A. Dreher, "Modular Smart antenna array for GPS and Galileo Applications," *The European Navigation Conference ENC-GNSS*, Munich, Germany, 12 pages on CD-ROM, Jul. 2005.

[3] M. Clergeaud and M. Thiel, "Algorithms for beamforming and beamsteering of adaptive antennas for satellite communications and navigation," *Internal Report*, DLR-IB 554-04/01, DLR, Germany, 2003.

[4] F.-I. Tseng and D. K. Cheng, "Invariant scannable planar arrays with an invariant sidelobe level," *Proc. IEEE*, vol. 56, no. 11, pp. 1771-1778, Nov. 1998.

[5] I. S. Reed, J. D. Mallet and L. E Brennan, "Rapid convergence rate in adaptive arrays," *IEEE Trans. Aerosp. Electron. Syst.*, vol. 10, pp. 853-863, Nov. 1974.

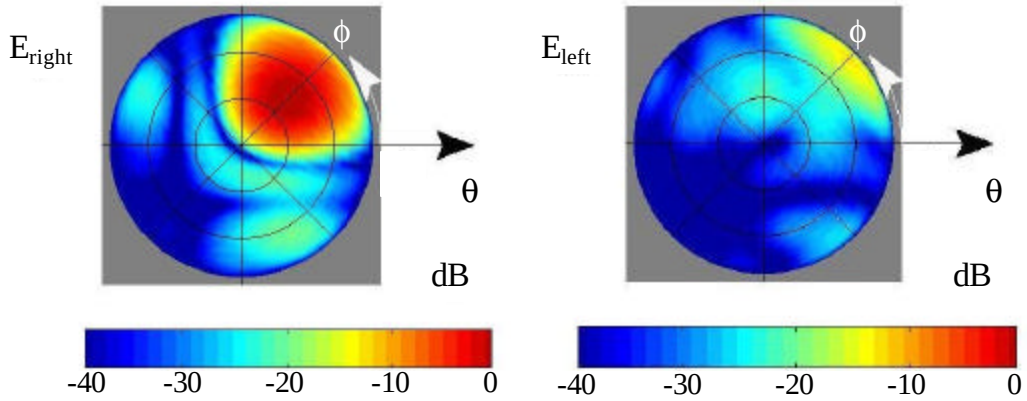

Fig. 3. Normalized Fields radiated by the antenna array at 1.19 GHz.

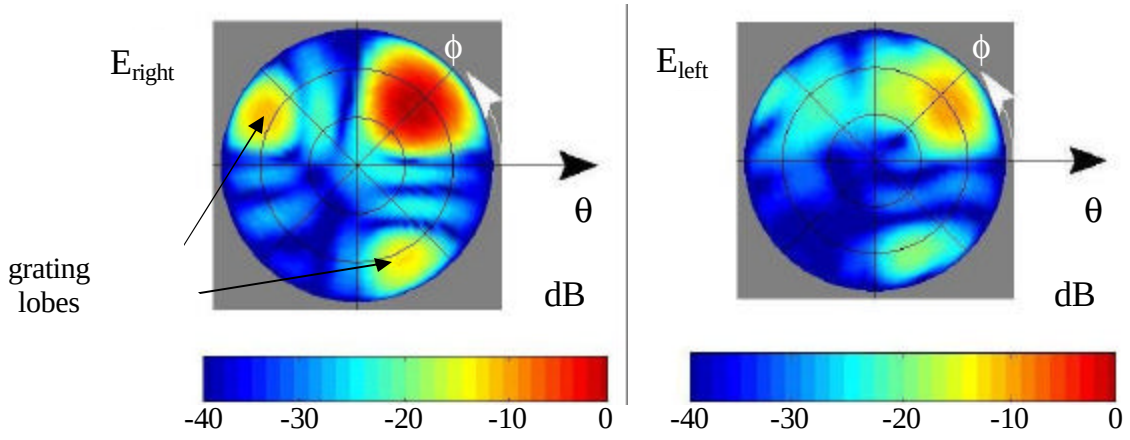

Fig. 4. Normalized Fields radiated by the antenna array at 1.57 GHz.